UNIVERSITY OF HAWAI'I

FINAL REPORT

U.S. Department of the Interior
Minerals Management Service
Contract No. 1435-01-98-CT-30964

EXPERIMENTAL STUDY OF MULTI-PHASE PLUMES WITH APPLICATION TO DEEP OCEAN OIL SPILLS

Submitted to:

U.S. DEPARTMENT OF THE INTERIOR
Minerals Management Service
381 Elden Street
Herndon, Virginia 20170-4817

Submitted by:

HAWAI'I NATURAL ENERGY INSTITUTE
University of Hawaii
2540 Dole Street, Holmes Hall 246
Honolulu, Hawaii 96822

Authors:

Stephen M. Masutani
University of Hawaii
and
E. Eric Adams
Massachusetts Institute of Technology

DISCLAIMER

Approval of this report by the Minerals Management Service does not signify that the contents necessarily reflect the views and policies of the Service, nor does mention of trade names or commercial products constitute endorsement or recommendation for use.

ABSTRACT

Offshore oil and gas exploration and recovery activities are taking place at increasingly greater depths in the ocean. During these operations, well blowout or oil leakage may occur. Transport and dispersion of the contaminants released during these events may be affected by factors that are not encountered near to the ocean surface, such as the transformation of natural gas bubbles into solid hydrates.

Accurate predictive models of deep ocean spills must be developed to address safety and environmental concerns. Since the understanding of the underlying physical phenomena is incomplete, modeling efforts need to be complemented by well-controlled experiments. The present investigation responds to this need. Tests examined the mechanisms of oil droplet and gas hydrate formation and the behavior of multiphase plumes rising through a density stratified water column. The study was performed jointly by Drs. Stephen Masutani of the University of Hawaii (UH) and Eric Adams of the Massachusetts Institute of Technology (MIT).

This Final Report summarizes all technical activities undertaken at UH and MIT as part of U.S. Department of the Interior (Minerals Management Service) Contract No. 1435-01-98-CT-30964.

TABLE OF CONTENTS

LIST OF FIGURES

LIST OF TABLES

EXECUTIVE SUMMARY

This Final Report summarizes technical activities conducted at the University of Hawaii (UH) and the Massachusetts Institute of Technology (MIT) as part of the investigation entitled "Experimental Study of Multi-Phase Plumes with Application to Deep Ocean Oil Spills."

Experiments were conducted at the UH and MIT to investigate the behavior of oil and gas released into the deep ocean during underwater oil well blowout and spill events. The principal results and primary conclusions of this study are:

1. Approximate boundaries of the instability regimes of crude oil discharging into water were identified. The boundaries differ from those established in earlier studies of liquid jets in a gas and are shifted to lower values of Reynolds numbers. Relationships for the boundaries are provided in Equations III.1.1 and II.1.2.

2. As oil jet breakup in water approaches atomization, two instability mechanisms appear to operate in parallel, producing a polydispersion of droplets comprising two distinct size groups. Small droplets are generated by a short wavelength surface instability while large droplets, of the order of the oil discharge orifice, may continue to form in transitional jets from a filament of core jet fluid.

3. Although the PDPA was unable accurately to measure droplet size distributions of opaque crude oil, size histograms obtained using a clear analog fluid support the above mechanism for the breakup of jets approaching atomization. To the authors' best knowledge, these size histograms represent a unique addition to the database on liquid-liquid breakup.

4. The data do not indicate any clear relationship between orifice diameter and the size of the fine droplets. Additional experiments need to be conducted to confirm this apparent scale independence.

5. Plume type depends on U_N such that Type 1* plumes occur for U_N less than about 1.4, Type 2 plumes occur for U_N between about 1.4 and 2.4, and Type 3 plumes occur for U_N greater than about 2.4.

6. Field plumes exhibiting Type 1* behavior would have oil droplets that initially are trapped in the intrusion layers. Trapping oil in the intrusion layers produces two results. First, the droplets are dispersed over a wide area, the size of the area depending on the degree to which the droplets stay with the intruding water. Second, the dispersed oil droplets lose (at least some) of their identity with the plume and can rise only at their slip velocity. A random-walk dispersion model would be a good candidate model for simulating the fate of oil droplets stripped from the plume by an intrusion layer.

7. The trap height, h_T, and the intrusion layer flux for the first intrusion, Q_i, both decrease with increasing U_N. This is due to the loss of buoyancy from the bubbles/droplets when the bubbles/droplets separate from the fluid. As U_N increases, the bubbles/droplets become more independent of the fluid and separation occurs earlier and more completely.

8. Separation occurs in multi-phase plumes in a crossflow at the critical height, h_{cr}, given by (III.2.4).

9. Multi-phase plumes in a crossflow differ from single-phase plumes when the crossflow separates the entrained fluid (and the fine oil droplets) from the rising bubble column. Above that height the gas bubbles can be modeled as the vector sum of their group rise velocity and the current speed, and the separated fluid can be modeled as a single-phase plume with the appropriate initial volume, buoyancy, and momentum flux.

10. Multi-phase plumes in a stratified crossflow have varied behavior, depending on the relative strength of the stratification to the crossflow. When the trap height predicted for stratification, h_T, is much less than the separation height for the crossflow, h_{cr}, the plume is stratification dominated, and the crossflow can be neglected in the near-field. In the opposite case, where h_{cr} is much less than h_T, separation will occur due to the crossflow and the plume is crossflow dominated: stratification can be neglected in the near-field of the plume. When the two separation heights are comparable, some fluid is stripped by the current and some fluid rises to the peel height, but the end result is that fluid intrudes in the lee of the plume at $h_T \approx h_{cr}$.

11. Hydrate formation on rising bubbles of natural gas is fostered by large bubbles and high gas loading. Hydrate formation appears to begin in the wake or on downstream surfaces of bubbles. If gas loading is high (i.e., the concentration of bubbles is high), then the hydrate film can promote bubble agglomeration and growth of the hydrate mass

12. The presence of oil at the gas-water interface can exercise an inhibiting effect of the initiation and growth of hydrate films. Additional experiments are warranted to clarify the influence of oil type, film thickness, and other factors.

Based on the results of the present investigation, it is recommended that:

1. Experiments be conducted at lower values of Ohnesorge number (i.e., using larger orifices and flow rates) to confirm the boundaries of the crude oil-water instability regimes that were identified in the present study.

2. Larger scale experiments also should be performed to determine if the size of fine droplets produced on the surface of the oil jet are independent or only weakly dependent on the dimension of the discharge orifice. This has important implications with regard to the far-field dispersion of the contaminant material.

3. Effort should be made to develop techniques to measure the full size distribution of droplets produced by transitional and fully atomized liquid jets in another liquid.

4. .The SINTEF field experimental data should be used to verify the correlation equations derived for this report from the laboratory experiments.

5. The model of Yapa & Zheng (1999) should be adapted to account for the separation observed in crossflow-dominated plumes illustrated above and should be tested for the momentum jet/plume region after separation.

6. Additional laboratory experiments in stratification and crossflow should investigate the enhanced leakage observed in stratification-dominated plumes.

7. Multiple separating dispersed phase plumes (plumes with several bubble/droplet classes having different slip velocities) should be studied in the laboratory and compared to the results presented above (with new theoretical relationships derived if necessary). These effects are important in field-scale plumes where gas, gas hydrate and oil may be present simultaneously in a wide range of bubble/particle/droplet sizes.

8. Experiments are warranted to confirm the effects of oil at the gas-water interface on hydrate formation. Studies should systematically examine the influence oil type and film thickness.

I INTRODUCTION

Offshore oil and gas exploration and recovery activities have been moving into increasingly deeper water. During these operations, undersea well blowout or oil leakage may occur. Transport and dispersion of the contaminants discharged during these events may be affected by factors that are not encountered near to the ocean surface, such as the transformation of natural gas bubbles into solid hydrates (Brewer *et al*., 1997; Szczepanski *et al*., 1998).

Well blowout or leakage will, in the general case, release two buoyant fluids into the sea water: oil and natural gas. The gas phase is highly buoyant; the oil phase is moderately buoyant. The combined buoyancy will drive a three phase plume (oil, gas, and sea water) which will rise toward the surface. En route, plume transport will be affected by interactions with the ambient ocean including: (1) entrainment of sea water into the plume; (2) physical-chemical reactions between sea water and both gas and oil; (3) sub-surface intrusion of portions of the plume; and (4) surface spreading of remaining portions of the plume. These phenomena and other complex mechanisms, such as jet instability and break-up, that influence plume generation and transport are not completely understood.

Accurate predictive models of deep ocean spills must be developed to address safety and environmental concerns (Yapa & Zheng, 1997). Modeling efforts need to be complemented by well-designed experiments that can elucidate the physical processes upon which the models are based, and that can provide data for model calibration and validation. A Deep Spills Task Force (DSTF) was formed to support this research. The Task Force is a partnership between industry and government.

Dr. Poojitha Yapa of Clarkson University was contracted by the Deep Spills Task Force to develop a robust model of deep ocean oil spills. Related laboratory experiments were performed jointly by Drs. Stephen M. Masutani of the University of Hawaii (UH) and E. Eric Adams of the Massachusetts Institute of Technology (MIT). The experimental component of the research program is the subject of this Report. The experiments were conducted to provide qualitative insight into basic physical phenomena and quantitative data for the development and calibration of mathematical submodels.

The primary objectives of the laboratory investigation were to simulate: (1) the break up of contaminants discharging into the deep ocean environment from well blowout and other deep oil spills; (2) the interactions between sea water, gas bubbles, and oil droplets within the plume; and (3) the macroscopic (global) behavior of multiphase plumes rising in a stratified water column. Tests also were performed to study the behavior of multi-component plumes in a crossflowing current. On a global scale, the behavior of oil and gas plumes is similar to single-phase plumes up to the point where the dispersed phase separates from the entrained fluid. For a plume developing in a stably stratified water column, separation occurs when the buoyancy of the dispersed phase can no longer support the dense entrained fluid. In a crossflow, the lateral motion of the current can also precipitate a separation of the phases. Integral models of oil/gas plumes need to account for separation since it breaks down the underlying similarity assumption.

This Final Report summarizes all technical activities undertaken at UH and MIT as part of the investigation entitled "Experimental Study of Multi-Phase Plumes with Application to Deep Ocean Oil Spills." The investigation was funded through Contract No. 1435-01-98-CT-30964, between the U.S. Department of the Interior, Minerals Management Service, and the University of Hawaii at Manoa.

I.1 Objectives and Scope

The overall goal of this study was to conduct laboratory experiments that would support the development of predictive models of deep ocean oil spills. The experiments were intended to provide qualitative insight into physical phenomena and, wherever possible, quantitative data on the breakup of contaminant jets from deep oil spills into a buoyant dispersed phase; hydrate formation in the water column; and global plume behavior in stratified media and in the presence of cross currents. The scope of this investigation was limited to laboratory experiments and the analysis of the results of those experiments; the scope of work did not extend to deep oil spills model development, which was pursued in a separate research effort funded by the DSTF.

Specific objectives of the present study included:

1. Conduct experiments of the breakup of jets of four deep crude oils and similar pure fluids to determine the effects of jet velocity, discharge orifice size, jet fluid properties, and ambient fluid properties (e.g., temperature; salinity) on the breakup mechanism and the size spectra of the resulting dispersed phase.

2. Analyze the results of the liquid-in-liquid breakup experiments to map the different instability regimes in scale-independent, non-dimensional space and to characterize the size distributions of oil droplets in underwater spill plumes.

3. Perform experiments using gas, oil, and combined gas/oil plumes in stratification to observe potential separation among the phases and to determine the extent to which fine oil droplets strip from the plume and become trapped in the intrusion layers.

4. Analyze the stratified experiments to obtain predictive criteria applicable at the field-scale for when the oil will separate from a rising gas plume and intrude with the peeling plume fluid.

5. Perform experiments of gas, oil, and combined gas/oil plumes in a crossflow to visualize how multi-phase plumes in a current differ from single-phase plumes.

6. Analyze the cross-flow experiments to understand the critical elevations at which certain events take place, such as the leakage of fine droplets from the downstream edge of the plume or the escape of larger droplets or gas bubbles from the upstream side.

7. Use the analysis of the plumes in a crossflow to develop an algorithm for incorporating multi-phase effects into the field-scale model of Yapa and Zhang (1999). Their model is a complete oil spill fate prediction tool that includes the effects of chemistry, mass transfer, hydrate formation, etc.

8. Perform exploratory experiments in stratification with crossflow to test the hypothesis that the effects of a current which were observed without stratification will also be observed in stratification as long as the critical elevations for crossflow separation occur before the plume becomes trapped due to stratification.

9. Perform exploratory experiments in a pressurized, simulated deep ocean environment to investigate the conversion of natural gas bubbles rising through the water column into hydrates and to assess whether an oil film at the gas-water interface inhibits this conversion.

I.2 Organization of the Report

Descriptions of the experimental facilities and procedures, and the methods of approach employed to collect and to analyze the data are provided in Section II. The experimental results are discussed in Section III and a summary and conclusions are presented in Section IV. Supplementary material can be found in the report appendices.

II METHOD OF APPROACH, FACILITIES, AND PROCEDURES

II.1 Studies at UH

UH researchers conducted two series of experiments utilizing different test facilities. Liquid-in-liquid jet breakup experiments were performed in an atmospheric pressure, clear Plexiglas tank measuring approximately 0.55 m x 0.55 m in cross section and 1.3 m tall. For weakly- or incompressible liquid-liquid (i.e., a liquid jet discharging into a liquid environment) systems, theory indicates that ambient pressure is not a relevant parameter and jet breakup into a dispersed phase in the deep ocean can be simulated in an atmospheric pressure facility. On the other hand, since ambient pressure profoundly affects hydrate formation, exploratory tests of rising bubbles of clean and oily natural gas components were conducted in a downward flowing water tunnel immersed in a 0.55 m i.d. cylindrical steel pressure vessel.

II.1.1 Jet Breakup

When oil escapes into the water column from undersea wells or pipelines, it will break up into droplets. The size of these droplets will influence whether they will reach the surface or remain dispersed in the water; how they dissolve; and the condition of any resulting surface oil slick (Rygg & Emilsen, 1998; Johansen, 1999). Modeling of deep oil spills stands to benefit significantly if the initial droplet size spectra can be estimated for different blow-out or leakage scenarios.

The breakup into a dispersed (droplet) phase of a contaminant liquid jet issuing into another liquid remains poorly understood. While studies of jet instability have been pursued for almost 170 years, “there are no generally accepted theories, regimes, or even terminology” (Reitz & Bracco, 1986). The majority of effort to date has been directed toward studies of liquid jets in air (hereinafter referred to as liquid-gas). While instability phenomena in liquid-gas and liquid-liquid systems are similar, they are not identical; breakup is affected by the properties of the

continuous (ambient) phase and the condition of the jet-ambient fluid interface–which can be significantly different in the two systems. Investigations of liquid-liquid instability are limited, and largely confined to the laminar flow regime. Little or no information exists on droplet sizes produced by transitional flow and turbulent breakup events that are likely to occur during deep oil spills. One of the goals of the present study was to attempt to address this deficiency.

II.1.1.1 Jet Breakup: Background and Approach

Background information on jet breakup can be found in Reitz & Bracco (1986), Kitamura & Takahashi (1986), Lefebvre (1989), and Teng (1994).

Instability of a cylindrical liquid jet issuing into another immiscible (or slightly miscible) fluid may be caused by interfacial tension (Rayleigh, 1945), gravitational effects (Chandrasekhar, 1981), or by hydrodynamic forces (Reitz & Bracco 1986). In many applications, including undersea oil spills, the gravitational force (body force) is negligible relative to surface tension and hydrodynamic forces; jet instability depends primarily on surface forces (i.e., interfacial tension, viscous forces, and hydrodynamic forces acting at the jet-ambient fluid interface). Due to these forces, the jet becomes unstable and breaks up into droplets.

Droplet formation is poorly understood due to insufficient information on the effects of hydrodynamic forces (for high jet velocities) and mass transfer, as well as the influence of jet and ambient fluid properties on jet instability. For liquid-liquid systems, information pertaining to droplet formation is largely based on experimental observations. As a result, in most practical applications, prediction of droplet size depends on empirical correlations obtained for only a few systems. Theoretical analyses have been attempted for low flow rate situations (Weber, 1931; Tomotika, 1935; Tomotika, 1936; Teng *et al.,* 1995), but, to date, no general droplet-size (theoretical or empirical) expression has been reported in the literature.

II.1.1.1.1 Breakup Mechanisms and Flow Regimes

The breakup of liquid jets into droplets is driven by a competition between cohesive and disruptive forces. Instabilities that can lead to deformation of the jet surface may be amplified or damped. The dominant mode of instability depends on a number of factors, including jet velocity and fluid properties, and manifests itself in the appearance of disintegrating jet.

Studies have identified a number of distinct flow regimes wherein breakup apparently proceeds by different mechanisms that change the characteristics of the generated droplet ensemble. An understanding of the boundaries of these regimes is important in order to be able to anticipate the type (i.e., size; mono- or polydispersion) of droplets produced by different oil spill and leakage scenarios.

Figure II.1.1 from Grant & Middleman (1966) shows the typical evolution of jet breakup length observed as jet discharge velocity is increased. Breakup length is the distance from the discharge orifice to the point where discrete droplets are formed. Upstream of this point, the jet remains continuous and intact.

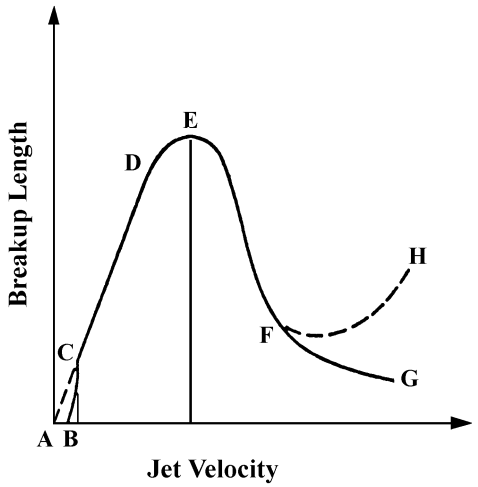

Figure II.1.1 Variation of jet breakup length with velocity (from Grant & Middleman, 1966). At very low velocities, large droplets are produced at the orifice (sometimes called drip flow). As velocity is increased, a laminar jet forms (point C) and breakup length increases linearly until it reaches a maximum. In this Rayleigh instability regime, axisymmetric disturbances grow in amplitude on the jet surface, eventually pinching off the jet column to generate a stream of essentially monodispersed droplets about 2 times the initial jet diameter. Surface tension forces are dominant over this range. The Rayleigh instability regime has been the subject of extensive theoretical analyses (Tomotika, 1935 & 1936; Weber, 1999; Teng *et al.,* 1995).

After attaining a maximum value, breakup length decreases. Droplet size remains nearly uniform and larger than the jet diameter (for liquid jets discharging into a gas). This flow regime is referred to as the first wind-induced breakup. Hydrodynamic forces arising from the relative velocities of the jet and ambient fluid accelerate breakup. Beyond point F on the curve, the relative influence of surface tension decreases and breakup is determined by hydrodynamic forces. The term "sinuous instability" is often used to describe the process in this second wind-induced breakup regime and droplet size decreases and becomes irregular (polydispersed). Breakup length can increase slightly or decrease steadily before falling to zero. At higher velocities, instability begins on the jet surface and produces a polydispersed spray of fine droplets immediately downstream of the orifice; however, the core of the jet may remain intact and this filament can persist for some distance before disintegrating. A single breakup length may not be adequate to describe the jet in this atomization regime and also during the latter stages of the second wind-induced breakup. Reitz & Bracco (1986) propose that both intact-surface and intact-core lengths be used to describe the jet.

The preceding regimes have been identified based on observations of liquid jets discharging into a gas. Figure II.1.2 from Kitamura & Takahashi (1986) presents measured breakup lengths and droplet sizes for a liquid-liquid system (i.e., water injected into carbon tetrachloride). The figure also contains sketches of the jet appearance at different velocities. The general shape of the breakup curve resembles Figure II.1.1; however, droplet size non-uniformities (indicated by the height of the bars around the droplet diameter data points) appear earlier and can be much more pronounced than in most liquid-gas systems. Based on the rather disorderly mode of breakup,

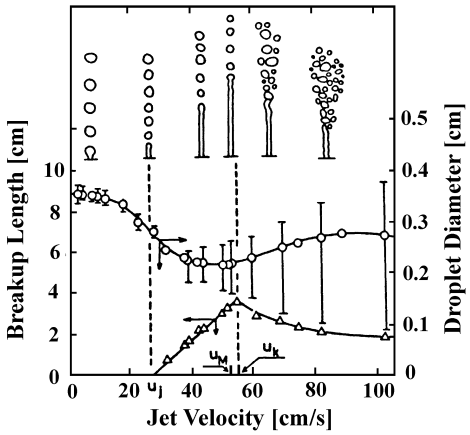

Figure II.1.2 Jet breakup length and droplet size as functions of velocity for a liquid (water) jet discharging into liquid carbon tetrachloride (from Kitamura & Takahashi, 1986). Orifice diameter was 0.118 cm. The figure also shows sketches of the appearance of the jet.

Kitamura & Takahashi (1986) proposed that the process be designated as turbulent once jet velocity exceeds the value corresponding to the maximum jet length.

In order to extend the application of case-specific data and to develop general relationships, attempts have been made to correlate experimental observations against the non-dimensional Reynolds (Re_D) and Ohnesorge (Z) numbers (Ohnesorge, 1936). Figure II.1.3a provides an example of the experimentally determined boundaries of the primary instability regimes determined from liquid-gas experiments. The figure also indicates that breakup can be influenced by additional factors, such as ambient fluid density (and other properties) and the initial state of the jet, which are not accounted for by Re_D and Z. A complete characterization of the breakup process probably requires that regime boundaries be presented as surfaces rather than lines, such as in the conceptual sketch prepared by Reitz (1978) shown in Figure II.1.3b.

While the mode of breakup is manifested–to an extent–in the size distribution of the resulting droplets, size data alone will not reveal many important features of the instability process. Earlier studies of jet breakup have successfully employed flow visualization as the primary measurement technique. This approach was applied in the present investigation where direct video imaging complemented size measurements performed with a laser phase Doppler particle analyzer.

II.1.1.1.2 Dimensionless Parameters

Following standard practice to develop scale-independent results, data were analyzed and, wherever possible, presented in non-dimensional space. It is generally agreed that the following dimensionless parameters characterize jet instability (Reitz & Bracco, 1986; Kitamura & Takahashi, 1986; Lefebvre, 1989; Teng, 1994):

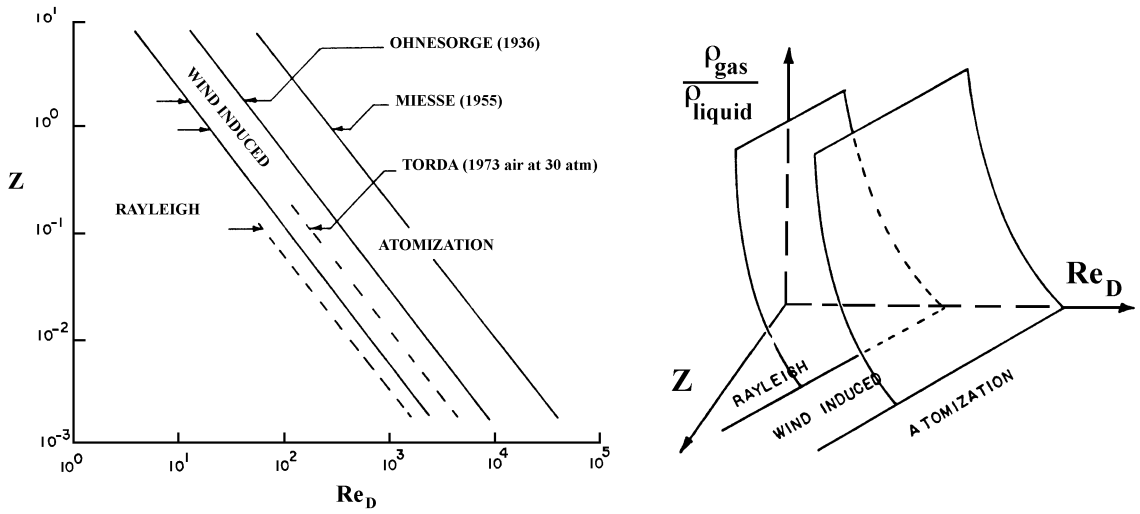

1. (b)

Figure II.1.3 (a) Instability regimes as a function of Ohnesorge (Z) and Reynolds (Re_D) numbers; the dotted lines show a shift in the boundaries due to ambient fluid density (from Reitz & Bracco, 1986); (b) conceptual sketch by Reitz (1978) showing regime boundaries as surfaces to account for the relative densities of the jet and ambient fluids.

Reynolds Number, Re_D

$$\mathrm{Re}_D \equiv \frac{U_j D}{\nu_j} \tag{II.1.1}$$

Weber Number, We

$$We \equiv \frac{\rho_j U_j^2 D}{\sigma} \tag{II.1.2}$$

*Ohnesorge Number, Z, and Modified Ohnesorge Number, Z**

$$Z \equiv \frac{\mu_j}{\sqrt{\rho_j \sigma D}} = \frac{\sqrt{We}}{\mathrm{Re}_D} \tag{II.1.3a}$$

$$Z^* \equiv \frac{3\mu_j + \mu}{\sqrt{\rho_j \sigma D}} \tag{II.1.3b}$$

Bond Number, Bo

$$Bo \equiv \frac{g\Delta\rho D^2}{\sigma} \tag{II.1.4}$$

The subscript $_j$ denotes properties of the jet fluid; ambient fluid properties are not subscripted. U_j is taken to be the bulk-mean inlet velocity of the jet (calculated as the volumetric flow rate of jet fluid divided by the cross sectional area of the injection orifice); D is the injection orifice diameter; *g* is the gravitational constant; ρ, μ, ν, and σ are, respectively, fluid density, dynamic

viscosity, kinematic viscosity, and interfacial tension; and $\Delta\rho$ is the difference in the densities of the jet and ambient fluids.

Re_D is the ratio of inertial to viscous forces; *We* is the ratio of disruptive momentum (hydrodynamic) forces to restoring surface tension; and Z, a stability index given as the ratio of viscous forces to surface tension. The modified Ohnesorge number (Teng *et al.,* 1995), Z*, attempts to account for the influence of ambient fluid viscosity on jet instability and breakup. Ambient density effects appear in the Bond number, *Bo* (sometimes called the Eötvös number; *vide* Kumar & Hartland, 1984); ambient density also is employed occasionally to calculate the Weber number. *Bo* is important for buoyancy-driven flows (e.g., gases leaking upward into a liquid; liquids falling through a gas) and is less relevant for high Weber number jets.

As mentioned previously, other factors not included in the above dimensionless groups are believed to influence jet breakup and, hence, the size distribution of the dispersed phase. The development of free shear flows, such as a contaminant oil jet, is known to depend strongly on the condition of the wall boundary layer at the point of separation and on upstream and downstream pressure fluctuations. To date, a viable approach to account for these factors in the analysis of breakup data has not been identified (furthermore, precise measurements of the jet initial and boundary conditions are not trivial)–which could explain some of the scatter encountered when data are correlated.

II.1.1.1.3 Characteristic Diameters

The diameter of an "average" droplet in an ensemble of polydispersed droplets can be represented by several statistically-determined quantities. Characteristic diameters conventionally employed in multi-phase flow studies that were applied in this investigation are:

Arithmetic Mean Diameter, D_{10}

$$D_{10} \equiv \frac{\sum_{i=1}^{n} d_i}{n} \tag{II.1.5}$$

Area Mean Diameter, D_{20}

$$D_{20} \equiv \sqrt{\frac{\sum_{i=1}^{n} d_i^2}{n}} \tag{II.1.6}$$

Volume Mean Diameter, D_{30}

$$D_{30} \equiv \sqrt[3]{\frac{\sum_{i=1}^{n} d_i^3}{n}} \tag{II.1.7}$$

Sauter Mean Diameter, D_{32}

$$D_{32} \equiv \frac{\sum_{i=1}^{n} d_i^3}{\sum_{i=1}^{n} d_i^2} \tag{II.1.8}$$

In the preceding definitions, d_i is the diameter of particle i and n is the total number of particles in the collection (ensemble). D_{10} is the ensemble mean diameter. D_{20} and D_{30} are the diameters that correspond to the calculated average droplet surface area and volume, respectively. D_{32}, the Sauter mean diameter, is the diameter of a droplet that has the same ratio of volume to surface area as the entire ensemble. D_{32} is particularly relevant to analyses of droplet mass transfer (e.g., dissolution; evaporation) and chemical reaction (e.g., spray combustion; hydrate formation), while D_{20} applies to studies of surface phenomena, such as hydrodynamic drag and heat transfer, and D_{30} to areas such as momentum transfer and buoyancy.

II.1.1.2 Experimental Set-up for Jet Breakup Tests

Jet breakup experiments were conducted in an atmospheric pressure water tank. While the UH pressure vessel had initially been considered for the tests, it was determined that this approach was impracticable and unnecessary. A trial run utilizing modest quantities of oil resulted in substantial fouling of the viewports, interior surfaces, and water lines, demonstrating that the vessel would need to be opened (i.e., the upper head removed) to suction out the oil layer and pump out the water, and to allow personnel access for cleaning after each oil injection test. Removal and replacement of the head requires 2-3 days, and degreasing the interior surfaces and servicing and re-torquing the viewports would increase total clean-up time per test (15-20 tests were planned) to more than 1 week. Furthermore, theoretical analyses and previous experiments suggest that jet breakup is insensitive to the absolute value of system pressure for weakly- or incompressible liquid-liquid systems; in liquid-gas systems, pressure exercises an effect through changes in the ambient gas density. An examination of the dimensionless parameters listed in Section II.1.1.1.2 and the governing equations (Teng, 1994; Kinoshita *et al.* 1994; Teng *et al.* 1995) reveals that the relevant ambient liquid properties are ρ, μ, and σ. These properties are very weakly dependent on pressure; they also do not vary widely over the range of temperatures (approximately $0°C \leq T \leq 25°C$) encountered in undersea oil spill events.

The primary diagnostics employed in the jet breakup experiments were digital video cameras and a phase Doppler particle analyzer (PDPA). Droplet size was measured using the PDPA and by direct imaging with the video cameras. The video cameras also provided information on the jet breakup length and transitions in the mode of breakup (e.g., Rayleigh; transitional; atomization).

The primary components of the experimental facility included:

1. an open, atmospheric pressure, clear Plexiglas tank measuring approximately 0.55 m x 0.55 m in cross section and 1.3 m tall.

2. Oil delivery system comprising a closed oil reservoir, variable speed gear pump, control valves, inline positive displacement flow meter, and temperature and pressure readouts.

3. Three discharge nozzles fitted with ASME sharp-edged circular orifices. Orifice diameters were 1, 2, and 5 mm. The nozzles were mounted on a manual, chain-driven traverse installed in the Plexiglas water tank.

4. Video system consisting of 3 tripod-mounted Sony Mini-DV video cameras (two DCR-TRV900 models and one DSR-PD100) and video lamps. Recordings were made with the cameras fitted with wide-angle conversion lenses that allowed better close-up views of the breakup and droplets.

5. Aerometrics (now TSI, Inc.) PDPA using a 1000 mm focal length transmitter lens and 0.25x beam expander, and a 500 mm (in air) focal length receiver lens. A 100 mW Omnichrome air-cooled argon laser or a 6W water-cooled Spectra Physics laser were used with the PDPA.

II.1.1.2.1 Tank and Oil Delivery System

A photograph of the atmospheric pressure Plexiglas tank is provided in Figure II.1.4 and a schematic drawing is shown in Figure II.1.5. The tank was constructed to test optical systems used in the UH pressure vessel and was therefore designed with similar dimensions. The square tank measures approximately 55 cm (21.5 in.) between the interior surfaces of the walls, and is about 1.3 m (51 in.) tall. It has a capacity of 400 liters (106 gallons) of water.

The tank is constructed from structural aluminum angle and plate, and clear cast acrylic Plexiglas. A thermistor probe is threaded through one of the lower circular windows and a second probe is suspended from the top to monitor water temperature. Oil injection nozzles are mounted on a horizontal traversing mechanism installed diagonally across the tank on two vertical shafts. The manual traverse is driven by an acetal chain and a gear-crank mechanism and is used to position the nozzle at an appropriate location relative to the PDPA optical sample volume. Oil discharges vertically upward. The height of the nozzle can be changed before a test by moving and locking the traverse assembly up or down the vertical shafts.

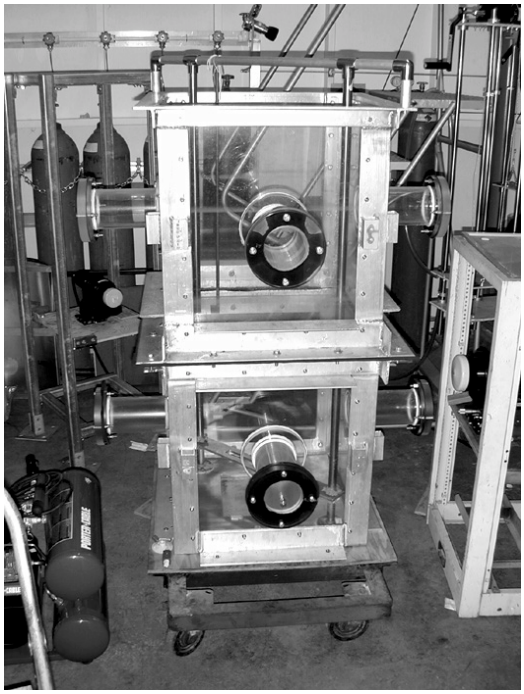

Figure II.1.4 Photograph of the Plexiglas tank used to conduct the oil breakup experiments.

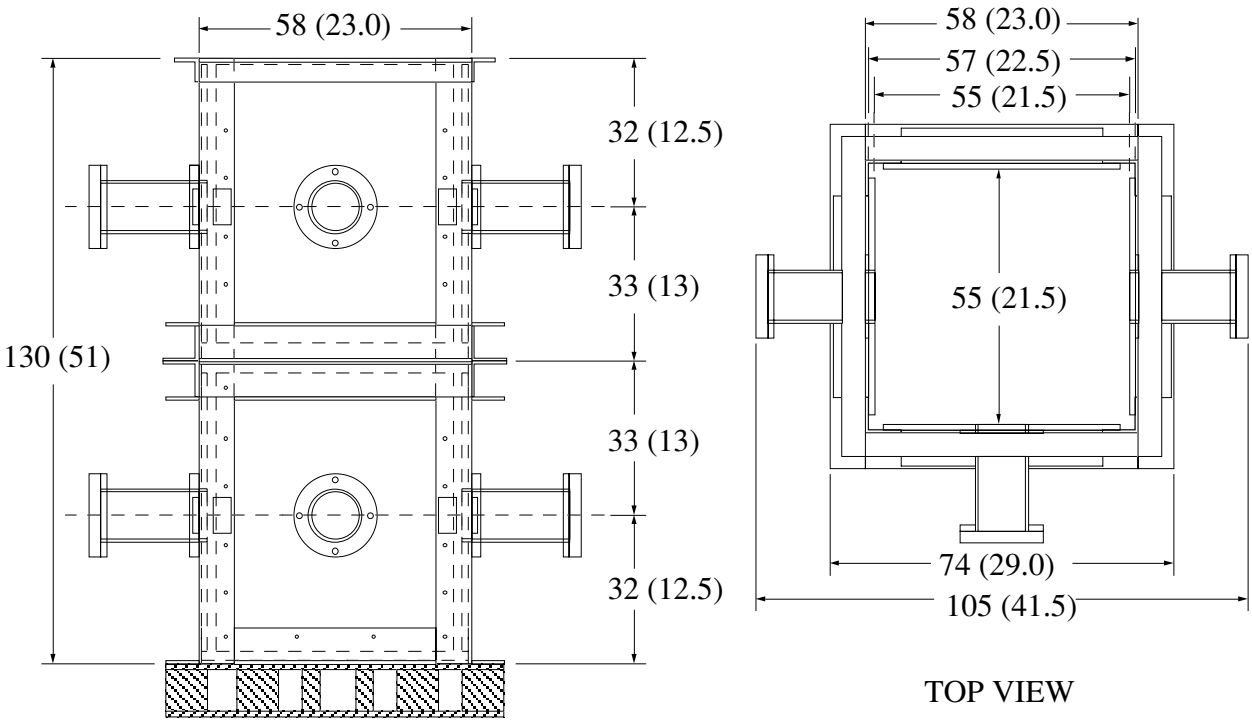

Figure II.1.5 Schematic drawing of the Plexiglas tank. Dimensions are given in centimeters and (inches).

Recirculation flows generated by the injection jet disperse small oil droplets throughout the water, resulting in a degradation in clarity that can make it impossible to conduct the optical measurements. To reduce this problem, a droplet trap is suspended between the vertical shafts about 15 cm below the centerline of the upper row of viewports. The trap comprises a square window screen and frame with dimensions slightly less (about 53 cm) than the distance between the interior surfaces of the tank walls. A layer of oil-only absorbent pads is attached to the screen and extends to the walls. A circular hole about 18 cm in diameter is cut in the center of the pads and screen to allow the rising oil plume to pass through it. The trap intercepts fine droplets that are advected downward after reaching the water surface and reduces the opacity they cause in the measurement zone.

Figure II.1.6 presents a schematic diagram of the oil injection system. A pulseless, magnetic drive, cavity-style gear pump (Micropump Series 2200) coupled to a Leeson variable speed 1 hp motor draws oil from a small (about 8 liter) reservoir. The reservoir is closed and the constant temperature water bath is removed to minimize devolatilization of the crude oils. Devolatilization produces undesirable changes in the oil properties (i.e., composition, viscosity, and density). Flow rate is set by adjusting the pump motor speed and two needle valves that divide the flow between the injector and a bypass line back to the reservoir. A positive displacement flowmeter (Omega Engineering FTB-1000 series) is installed inline with the injector to measure the flow rate of oil into the tank. Oil temperature and pressure are monitored with an inline thermistor and precision pressure gauge, respectively. All wetted parts are compatible with, and insoluble in, the oils.

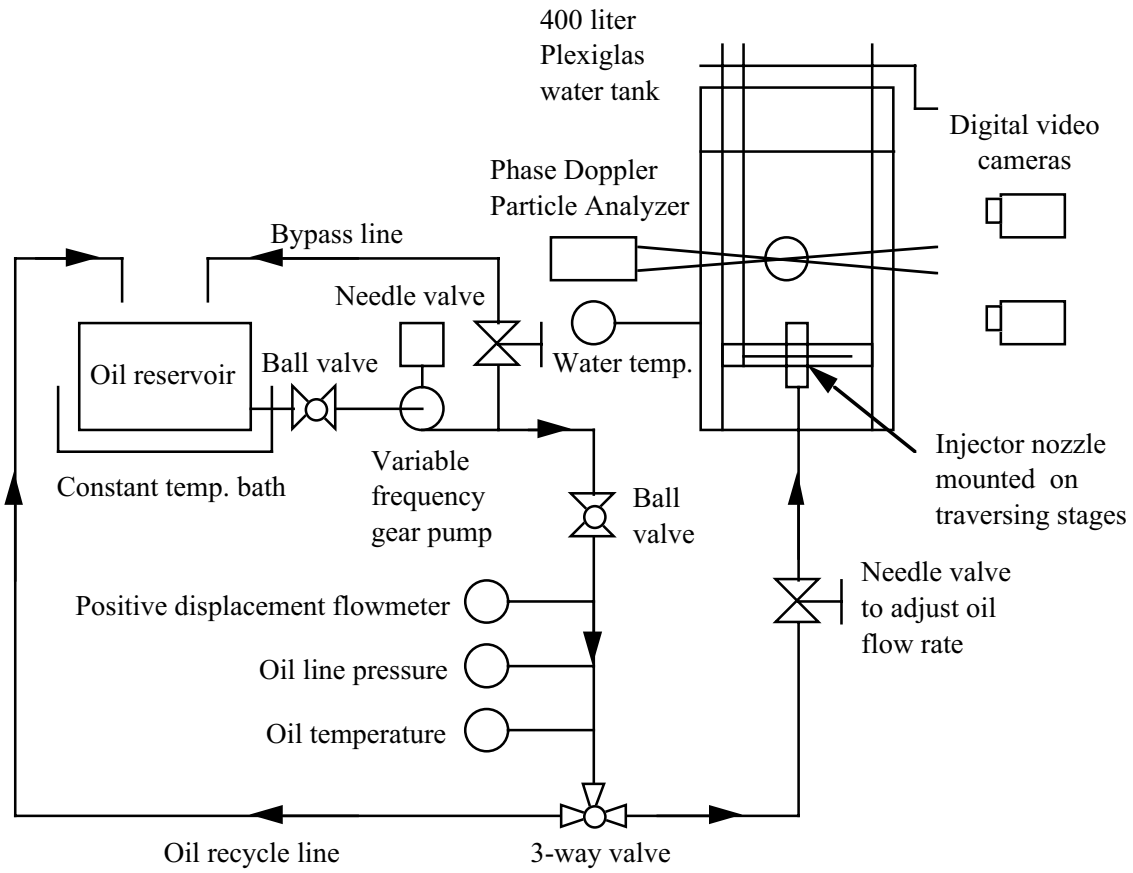

Figure II.1.6 Schematic diagram of the oil injection system.

Oil enters the tank through a pipe fitting in its base and flows through a short service loop of 9.5 mm (0.375 in.) i.d. flexible tubing before entering the injection nozzle mounted on the horizontal traverse. Three nozzles were used in the experiments with circular orifice diameters of 1, 2, and 5 mm. The nozzles were fabricated from thick wall 25.4 mm (1.0 in.) diameter stainless steel tubing and marine bronze. The nozzle profiles were machined to conform with specifications for ASME sharp edged orifices. Figure II.1.6 presents a photograph of the 2 mm and 5 mm nozzles.

Four deepwater crude oils–Genesis, Mars TLP, Neptune SPAR, and Platform Gail–were tested in the breakup experiments. The oils were analyzed by the Environmental Technology Centre of Environment Canada (Fingas, 1999). Results of those analyses are provided in Appendix A and can also be found in the Oil Properties Database at www.etcentre.org. As mentioned previously, the crude oils evaporate (i.e., devolatilize) readily, which can lead to significant changes in properties. Uncertainties in the values of critical properties such as ρ, μ, and σ used to calculate the dimensionless parameters Re_D, *We*, *Z*, and *Bo* complicate the interpretation of breakup data. It was decided, therefore, to supplement the crude oil results by conducting a series of tests using a stable (i.e., properties do not vary over time due to devolatilization) analog fluid that had comparable values of ρ, μ, and σ. After evaluating a large number of candidates, pure polydimethylsiloxane (silicone) fluid was selected. This silicone liquid has a very low vapor pressure at room conditions and is insoluble in water. Its properties are relatively stable over the

Figure II.1.7 Photograph of the 5 mm and 2 mm sharp edged orifice nozzles. The 1 mm diameter orifice nozzle has identical dimensions.

planned range of test conditions and are well documented (Rochow, 1987; Fendinger *et al*., 1997; Hoffmann & Ulbricht, 1999). Furthermore, unlike the very opaque crude oils, polydimethylsiloxane is transparent, which, as explained in the following section, makes it significantly easier to perform the optical PDPA measurements.

Comparisons of properties of the oils and silicone fluid are provided in Table II.1.1 and in Figure II.1.8. The silicone fluid properties fall very near or within the range of properties reported (or estimated) for the deepwater oils.

Table II.1.1 Comparison of properties of silicone fluid and four deepwater crude oils at 25°C (0% evaporation); surface tension, σ, of the oils were not measured; values shown were estimated from data on σ for similar crude oils given in the Environmental Technology Centre online database.

Oil Name	ρ [kg/m^3]	μ [centipoise]	ν [centistokes]	σ [dyne/cm]
Genesis	877	18	20.5	~25 (estimate)
Mars TLP	882	24	27.2	~25 (estimate)
Neptune SPAR	861	13	15.1	~25 (estimate)
Platform Gail	922	196	211	~25 (estimate)
SPF96-20 silicone fluid	977	19.5	20	21

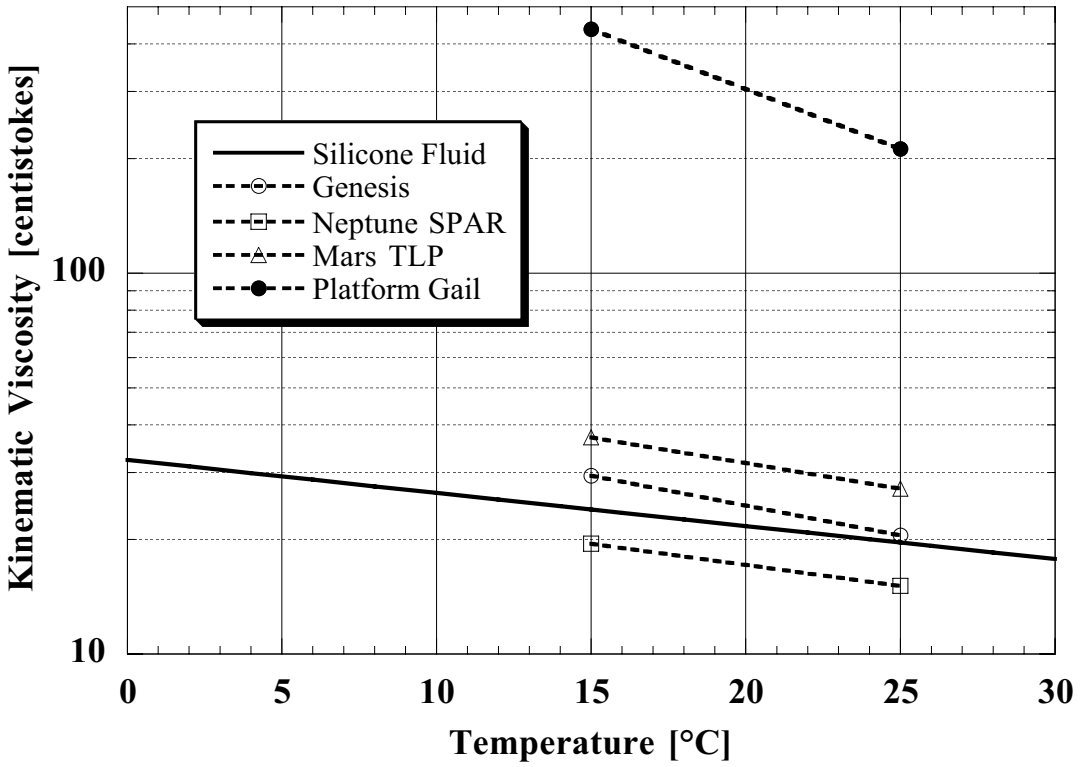

Figure II.1.8 Kinematic viscosities (in centistokes) of SPF96-20 silicone fluid and four deepwater crude oils. SPF96-20 viscosity obtained from the manufacturer; crude oil viscosities calculated from values of dynamic viscosity and density reported by Fingas (1999) at 15°C and 25°C for 0% evaporation.

II.1.1.2.2 Phase Doppler Particle Analyzer (PDPA)

Measurements of oil droplet size were attempted using both direct video imaging and a PDPA manufactured by Aerometrics, Inc. (now part of TSI, Inc.). Commercial laboratory particle sizers have a finite measurement range that is determined by factors such as the optics employed, photoelectronic detector sensitivity and S/N, theory of operation, and scattering characteristics of the media being tested. Instruments based on Fraunhofer diffraction (e.g., Malvern Instruments Mastersizer and Spraytec), interferometric phase shift (PDPA), and scattered light intensity (Insitec PSCV) have an upper size limit of no more than around 1-3 mm and a droplet size range of less than a 100-to-1 for a particular optical configuration (with typical values being around 50-to-1). For the liquid-liquid systems of interest to this study, the largest droplets that form in the laminar and transitional breakup regimes were anticipated to be several times the orifice diameter and would exceed the measurement limit of any of the commercially available instruments. Direct digital video imaging was therefore employed to extend the range of droplets that could be detected, since imaging is well suited for applications involving large (> 1 mm) particles. It was recognized that "splicing" results obtained from the digital video and PDPA measurements to generate an accurate size distribution that spanned the entire polyderspersion would be difficult or impossible. Rather, the video records would primarily serve as a check to determine whether the PDPA results were representative of the flow or if the

statistics were biased due to an insufficient measurement range or attenuation by the optically thick dispersed phase.

It should be noted that the accuracy of size data obtained by means of conventional video or photographic imaging is limited by depth of field issues and other factors. The magnification of an imaging system varies with the distance between the object (droplet) and the lens. Due to a finite depth of field (i.e., range of distances from the lens over which objects remain in focus), the exact magnification (and, hence, size) of a droplet image is uncertain. While selection of appropriate lenses, apertures, and illumination can minimize this uncertainty, the problem is exacerbated by droplet movement. Movement of a droplet at the focal point (where magnification is known) can lead to a blurred image that generally cannot be distinguished from blurring resulting from being outside the focal range (unknown magnification). Sheet illumination of the flow field reduces depth of field ambiguities but can be complicated in high number density situations where sheet extinction, and refraction and reflection are significant. A summary of the capabilities and problems of direct imaging and other optical and non-optical sizing techniques can be found in Chapter 9 of Lefebvre (1989).

The PDPA used in this study was originally procured for a different project to perform measurements of liquid CO_2 sprays in pressurized sea water. The range of droplet sizes encountered in that study and in the present investigation of oil breakup were expected to be identical. The primary difference was the optical characteristics of the opaque oil and the transparent CO_2. The PDPA was selected over the Malvern Fraunhofer diffraction instrument and the Insitec PSCV since it could detect larger droplets (approximately 4000 μm in refection mode vs. about 2000 μm for the Malvern and 200 μm for the Insitec PSCV). In addition, unlike the Malvern system which collects only size information data along the line-of-sight, the PDPA performs simultaneous, spatially-resolved measurements of the size and velocity of single particles. The Malvern results are therefore spatially-averaged while the PDPA generates time-averaged statistics. A brief description of the PDPA theory of operation and limitations follows.

Operation of the PDPA is based on geometrical optics and Lorenz-Mie scattering theory applied to spherical particles (Bachalo, 1980; Bachalo & Houser, 1984; Naqwi & Durst, 1991; Sankar & Bachalo, 1991). This is the primary limitation of the technique: it is valid strictly for spherical particles, droplets, and bubbles; deviations from a perfect sphere can lead to serious measurement errors.

PDPA is implemented by collecting light scattered by particles (used hereinafter in the general sense to denote a dispersed phase consisting of solids, liquids, or gas) passing through the intersection of two laser beams. Scattering occurs as a result of diffraction, refraction, and reflection. Light collection is performed at angles away from the forward direction (i.e., the direction of the laser beams) to avoid light scattered by Fraunhofer diffraction. Theory indicates that light scattered by refraction or reflection is shifted in phase if viewed from different locations, and that this phase shift can be related directly to the diameter of the scattering particle. Diffracted light contains no phase information and must be avoided. For $\alpha>15$ (where $\alpha= \pi d/\lambda$; d = particle diameter; λ = laser wavelength), diffraction is insignificant at angles >10° (a ray pointed in the direction of the laser beam propagation has an angle of 0°; a ray pointed at

the laser source has an angle of 180°). Thus, proper placement of the PDPA receiving optics can eliminate unwanted diffracted light.

It is easiest to understand PDPA operation by considering that the intersection of two coherent laser beams of equal intensity and parallel polarization produces an interference fringe pattern consisting of alternating bright (constructive interference) and dark (destructive interference) bands. A photodetector monitoring the light scattered by a particle traversing these fringes will experience a regular modulation of light intensity as the particle passes through the bright and dark regions. Figure II.1.9 shows a typical PDPA photodetector output signal. The electronic output of the detector is proportional to the intensity of the incident radiation. The signal is modulated at the Doppler frequency ($f_{Doppler}$), which is equal to the velocity of the particle normal to the fringes divided by the (equal) distance between fringes. The Gaussian envelope (called the pedestal) of the signal seen in the figure is a consequence of the Gaussian intensity distribution of the laser beams over their cross sections.

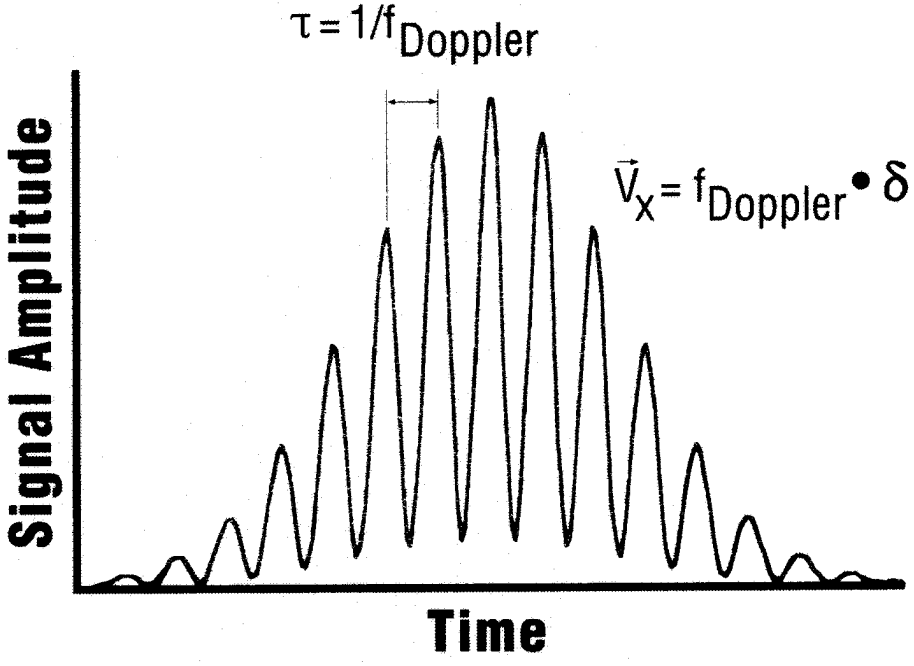

Figure II.1.9 Typical output signal from a photodetector monitoring light scattered by a particle traversing the interference fringes formed at the intersection of two laser beams of a PDPA (or laser Doppler velocimeter).

The fringe spacing, δ, can be calculated from the known laser wavelength, λ, and the angle at which the two beams cross. The component of velocity of the particle normal to the fringes can then be determined, since electronics can easily time the signal modulation and identify $f_{Doppler}$. This is the underlying principle of operation of laser Doppler velocimetry (LDV). PDPA extends the LDV concept through application of Lorenz-Mie theory. It can be shown that, for a spherical particle, the Doppler modulation of reflected or refracted light observed by separate detectors located at different angles from the beam intersection is shifted in phase. Figure II.1.10 demonstrates the phase shift of signals from three photodetectors spaced slightly apart from one

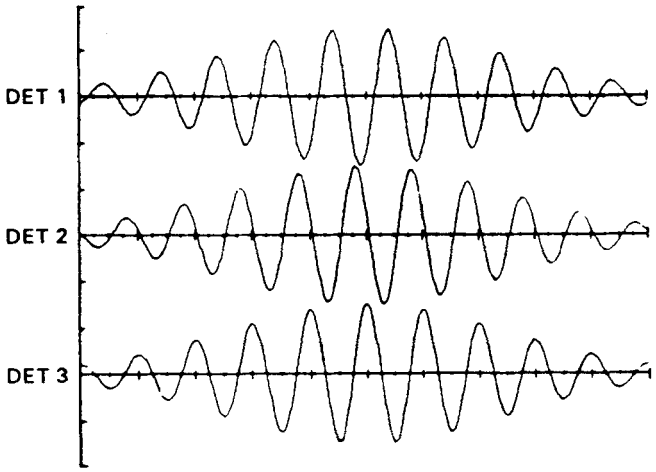

Figure II.1.10 Phase shift of output signals from three separate photodetectors monitoring light scattered by the same particle traversing the interference fringes at the intersection of two laser beams. The signals have been high-pass filtered to remove the Gaussian pedestal. Figure from Bachalo & Houser (1984).

another and monitoring scattered radiation from the same particle passing through laser interference fringes. The electronic signals have been high-pass filtered to remove the Gaussian pedestal. Theory provides that the phase shift is linearly related to the diameter of the scattering particle. Figure II.1.11 from Bachalo (1994), presents calculated phase shifts between the signals observed by detectors 1 and 2 (φ_{12}) and 1 and 3 (φ_{13}). Two pairs of detectors eliminate ambiguities when the size range extends over several (360°) cycles (i.e., over several of the shorter sawtooth functions). The particle diameter is found when the corresponding theoretical phase shifts match both measured values φ_{12} and φ_{13}.

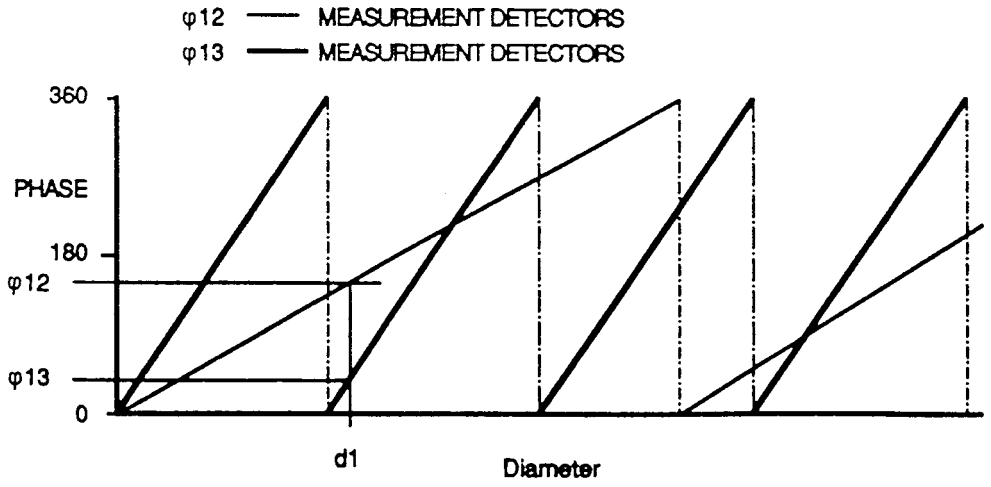

Figure II.1.11 Calculated phase shifts in signals observed by two pairs of three photodetectors (1, 2, and 3) as functions of scattering particle diameter (from Bachalo, 1994).

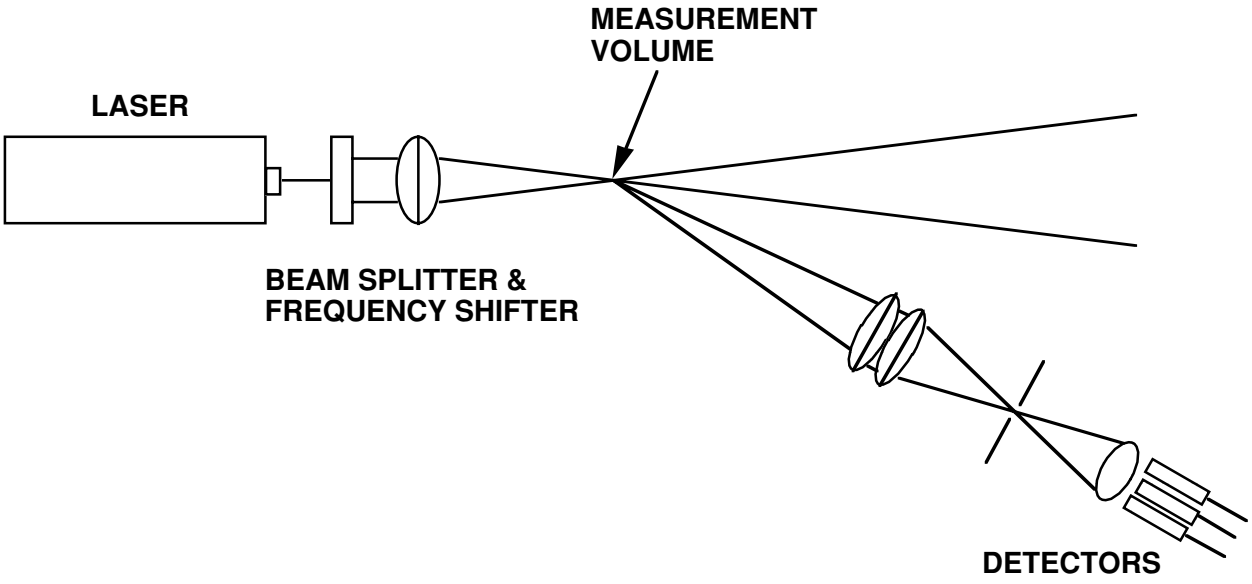

Figure II.1.12 Layout of optical components of a PDPA.

A schematic diagram of the primary optical components of a PDPA system is shown in Figure II.1.12. The output of a laser is divided using a beamsplitter or Bragg cell into two identical coherent beams. The beams are focused by the transmitter lens and cross at the measurement volume. Radiation scattered (reflected or refracted) off-axis by particles crossing the interference fringes is collected by the receiver optics and imaged onto three photodetectors (photomultipliers) whose spacing relative to one another is known and fixed. The sample volume is limited by placing a spatial filter (pinhole) in front of the detector lens. This restricts the field of view of the detectors to the volume defined by the image of the pinhole projected onto the intersection of the two laser beams.

The output of the photomultipliers are coupled to electronics that operate on these signals to determine particle velocity and diameter. The system is controlled by a personal computer. The electronics hardware and software provide elaborate data validation and error correction tools.

As mentioned previously, the PDPA is susceptible to measurement errors. If the scattering particles are non-spherical, then the underlying theory of operation and relationships between phase shift and diameter are invalidated. If the particles are deformed spheres (i.e., oblate or prolate spheroids), then the PDPA may over- or underestimate their diameters. Figure II.1.13 illustrates this problem.

Even if all particles are spherical, errors may arise due to factors such as the non-uniformity of laser beam light intensity over the optical sample volume and beam attenuation in optically thick flows.

In the presence of system noise, a threshold photodetector output (which corresponds to an incident light intensity) must be established, below which signals are rejected. This may bias the measurements in favor of large particles. Since the radiant intensity of the laser beams and,

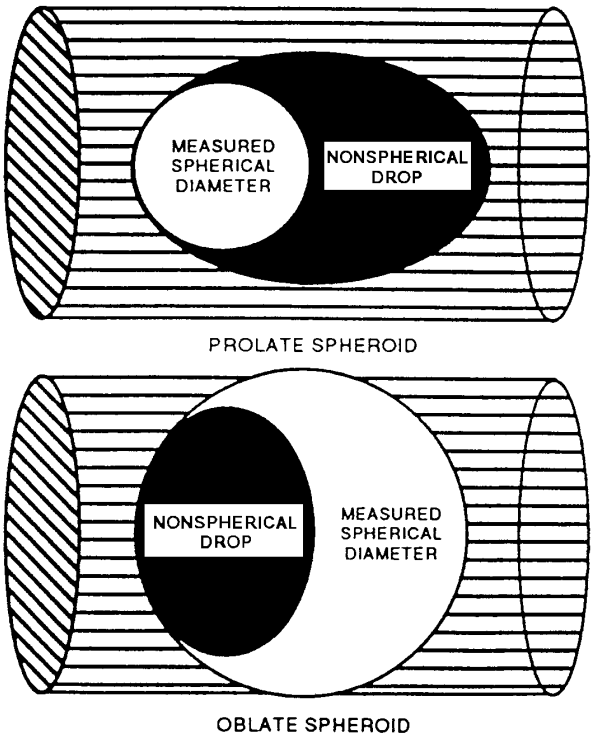

Figure II.1.13 PDPA measurement errors due to deformation of droplets. Cylinders represent the laser beam intersection and indicate the relative orientation of the major axes of the spheroids and the interference fringes. Figure from Bachalo (1994).

hence, the measurement volume, is not uniform but follows a Gaussian distribution, decaying rapidly with distance from the beam centerline, the peak intensity of light scattered by a particle will depend on whether its trajectory carries it through the center of the beam or near the edges. Since the amount of light scattered also depends strongly on the size of the particle–increasing as the square of diameter–a small particle moving through the edges of the measurement volume may produce a very low signal from the photodetectors that falls below the threshold and is rejected, while a large particle following the identical trajectory is accepted. This potential bias can be exacerbated when the concentration of particles is high and/or the particles are opaque. If slow transmitting optics are employed (i.e., the beams cross at a small angle and the length of the intersection zone is long) then particles intercepting the beam before the optical sample volume will attenuate the bright fringe intensity. This will, in turn, reduce the intensity of scattered radiation to a point where the signals from most small particles fall below the threshold and only large particles are detected. This bias problem appears to have affected the PDPA data obtained in the crude oil experiments.

Finally, it should be pointed out that PDPA measurements in the present investigation were conducted with the instrument configured to detect refracted light from the clear silicone fluid droplets and reflected light from the opaque crude oil droplets. The indices of refraction of the silicone fluid and the four deepwater crude oils were measured directly (see Appendix A) and did not differ substantially (about 1.40 for the silicone and 1.5 for the oils); however, these measurements examined a very thin film of oil. For droplets with finite dimensions, refracted light that passes through the droplets can be greatly attenuated or extingusihed altogether. In a

series of shakedown experiments, the PDPA was optimized to monitor refracted light from silicone fluid droplets in water. When crude oil was switched with the silicone fluid, the sampling rate dropped precipitously (by orders of magnitude). The detector output examined with an oscilloscope revealed that the scattered light intensities were very low. No amount of adjustment was successful in increasing the data rate to an acceptable level.

When the system was reconfigured to monitor reflected light by changing the angle of the receiver relative to the axis of the laser beams, rotating the polarization filter, and changing parameters in the software, the crude oil data rate improved substantially. On the other hand, size measurements of the clear silicone fluid became more difficult.

Light scattered off-axis by particles that are large relative to the wavelength of the light (the argon laser line used in the UH PDPA has a wavelength of 514.5 nm = 0.5145 μm) comprises a superposition of rays emerging from the particle after reflection, refraction, and single or multiple internal reflections. An optical detector may encounter one or a combination of these rays, depending on its location. Since the relationship between phase shift and particle diameter depends on the scattering mechanism (e.g., refraction or reflection), it is important to select the location of the detector such that only one scattering mechanism is dominant (Naqwi & Durst, 1991). If the detector is placed in a wrong location where levels of reflected and refracted radiation are comparable, then the size data calculated by the PDPA will be incorrect. The spatial distribution of the amplitudes of reflected and refracted light depends on the relative values of the indices of refraction of the ambient fluid and the droplet material, and varies with polarization.

Based on the shakedown experiments and after extensive consultation with the PDPA manufacturer (TSI, Inc.), the collection angles (i.e., placement of the PDPA receiver) were selected for the refractive silicone fluid measurements and the reflective crude oil measurements. Note that in the present investigation, the two laser beams lie one above the other in the vertical plane. The collection angle is defined relative to this plane (e.g., at 0°, the receiver is looking directly at the incoming laser beams; at 90°, the receiver monitors radiation scattered perpendicular to both beams). Although some mixing of refracted and reflected light was expected with these two configurations, it was assumed in the measurement algorithms that scattering signals consisted, respectively, of pure refraction and pure reflection for the silicone fluid and crude oils.

Table II.1.1 summarizes the PDPA configurations employed in this study.

II.1.1.3 Experimental Procedures and Data Reduction for Jet Breakup Tests

The typical procedure followed during the oil breakup experiments consisted of the following steps:

1. The selected nozzle is mounted on the horizontal traversing mechanism in the Plexiglas tank. A new oil droplet trap is installed about 48 cm above the nozzle. The tank is then wheeled into position between the PDPA transmitter and receiver and the oil supply line is connected.

Table II.1.2 PDPA set-ups used to measure size distributions of crude oils and silicone fluid.

	SPF96-20 silicone fluid	Genesis	Mars TLP	Neptune SPAR	Platform Gail
Index of refraction	1.405	1.497	1.498	1.486	1.518
Mode	Refraction	Reflection	Reflection	Reflection	Reflection
Collection angle	30°	60°	60°	60°	60°
Polarization	Horizontal	Vertical	Vertical	Vertical	Vertical
Laser beam expansion	0.25x	0.25x	0.25x	0.25x	0.25x
Transmitter lens focal length [mm]	1000 (in air)	1000 (in air)	1000 (in air)	1000 (in air)	1000 (in air)
Receiver lens focal length [mm]	500 (in air)	500 (in air)	500 (in air)	500 (in air)	500 (in air)
Spatial filter (pinhole) diameter [μm]	150	150	150	150	150
Theoretical droplet size range [μm]	5.7 - 1886	12.27 - 4059	12.27 - 4059	12.27 - 4059	12.27 – 4059 12.52 - 4077 (in sea water)
Measurable droplet size range[i] [μm]	37.7 - 1886	81.2 - 4059	81.2 - 4059	81.2 - 4059	81.2 - 4059 81.5 - 4077 (in sea water)

NOTES

i) The dynamic range of the receiver limits the minimum measureable droplet to about 1/50 of the maximum detectable droplet diameter.

2. The tank is filled with tap water or natural sea water. Ice is added to the tap water to chill it to a nominal temperature of either 7°C (45°F) or 18°C (65°F). Synthetic sea water is prepared by adding BioSea aquarium mix (chemical analysis available at www.aqcraft.com) to the tap water. Natural sea water obtained from a pipeline extending to a depth of 15.2 m (50 ft.) offshore of Kewalo Basin, Honolulu, Hawaii is chilled by storing it overnight in a walk-in refrigerator. The proportions of water and ice are calculated so that the tank ultimately contains about 335 liters (90 gallons) of water and the water level is approximately 73 cm above the nozzle. The water is agitated until temperatures indicated by the upper and lower thermistors agree to within 0.5°C.

3. The PDPA optics are aligned and the nozzle is moved using the traverse so that the discharge orifice is offset slightly from the optical measurement volume. Along the centerline of the orifice, droplet number densities are very high and multiple scattering and beam extinction are problems. Acceptable sampling rates are obtained by locating the measurement volume near the edges of the plume where the concentration of droplets is lower.

4. Two digital video cameras fitted with wide-angle conversion lenses are positioned next to the tank to view the jet at right angles to one another. One camera is zoomed in to image a small region immediately below the PDPA optical measurement volume and the other is set to record the overall jet structure. The camera clocks are synchronized with a handheld digital stopwatch/clock. The height of the laser beams above the nozzle is recorded and the close-up camera is calibrated by placing a scale within its field of view; autofocus is disabled.

5. Oil is pumped from the sealed storage barrels and the oil injection system reservoir is filled and covered. This step is carried out immediately before injection begins to minimize devolatilization of the crude oils.

6. Oil injection begins and the PDPA is tested to confirm that the data rate and signal quality are satisfactory. If not, then the optics are realigned and/or the nozzle is repositioned.

7. With injection off, the water is agitated near the optical measurement volume and the PDPA is used to sample the water-only phase to determine the level of background particulates within the measurable size range.

8. Size data are obtained with the PDPA for a number of injection velocities. Oil flow rate, temperature, and pressure; and water temperatures are recorded over the PDPA data collection period. Video is recorded continuously with the two cameras. Video data also are collected for very low and high flow rate conditions where the PDPA is unable to perform measurements.

9. After completion of a test, the layer of oil that has collected on the water surface is suctioned off into a oily waste storage vessel. Oil absorbing pads and sump skimmers are then used to remove most of the residual oil in the water. The tank is drained, the droplet trap is discarded, and the nozzle is removed. The tank is then disconnected from the oil supply system and wheeled away to a cleaning area where all surfaces are scrubbed clean and polished. Oil remaining in the reservoir is removed.

The positive displacement flow meter was calibrated for each of the four crude oils and silicone fluid. The uncertainty in the flow meter readings over the range of flow rates examined in this study appear to agree with the manufacturer's specification of approximately ± 5%.

To minimize cross contamination, all flexible tubing was replaced and the oil injection system was flushed thoroughly whenever a different oil was tested. Flushing consisted of draining the system of the old oil and pumping between 5 and 10 gallons of the new oil through all lines and components.

A number of attempts were made to conduct PDPA measurements of oil breakup in synthetic sea water. Synthetic sea water is convenient since–unlike natural sea water–its composition can be controlled and ice can be used to quickly adjust temperature without requiring a heat exchanger or refrigeration unit (salinity is subsequently adjusted by adding more aquarium mix). All PDPA trials were unsuccessful due to high water opacity (turbidity) that attenuated the laser beams and

obscured the scattered light. A fine precipitate formed throughout the synthetic sea water as it was chilled. The precipitate remained in suspension and did not dissolve over several hours. Alternative procedures to formulate and chill the synthetic sea water (e.g., pre-chill tap water and add aquarium mix; pre-mix tap water and aquarium mix, then chill) yielded little improvement. Synthetic sea water was therefore abandoned in favor of natural surface sea water.

PDPA size data were analyzed with the instrument's DataView software package and saved as tables comprising all droplet diameters measured during a run. During a run, between approximately 1000 to 3000 droplet diameters were validated and saved, with a count of 2000 being typical. Several algorithms developed by the PDPA manufacturer can be used to compensate for errors and instrument bias (see Section II.1.1.2.2). The DataView software package automatically calculates size statistics (e.g., characteristic diameters). The data files also were evaluated with the MatLab analysis program.

Still video images were captured from the recordings. Jet breakup length and the size of large droplets were estimated from the images both by direct measurements with a scale off a monitor screen or with digital image processing software. Image adjustment, filtering, and enhancement were performed using Adobe Photoshop and the public-domain NIH Image programs.

II.1.2 Gas Hydrate Formation in the Water Column

Large quantities of natural gas may escape into the water column with the oil during undersea well blow-out or leakage events (Rygg & Emilsen, 1998). The dynamics of the contaminant plume–and, hence, the ultimate dispersion of the contaminants in space–may be profoundly influenced by the buoyancy of this gas phase. In the deep ocean environment, ambient pressures and temperatures fall within a range where many hydrocarbon components of natural gas can exist as solid hydrates (Sloan, 1989). *In situ* observations (Brewer *et al*., 1997) and laboratory experiments (Maini & Bishnoi, 1981) suggest that natural gas bubbles may transform into solid hydrates as they rise through the water. This transformation produces an increase in density that results in a loss of global plume buoyancy.

The oil and natural gas phases can co-mingle prior to, and as they discharge into the water, yielding a contaminant plume that includes droplets of oil saturated with natural gas components and/or gas bubbles encased in a thin film of oil. Bishnoi and his co-workers have observed hydrate formation on the surface of oil droplets saturated with natural gas when hydrate nuclei are present in the water phase (Bishnoi, 1999). On the other hand, recent direct observations of naturally-occurring oil and gas seeps in the ocean suggest that hydrate formation is suppressed or precluded on oily bubbles of natural gas (Leifer, 1999). In consideration of the implications of such hydrate suppression on the modeling of buoyant oil and gas plumes, exploratory experiments were conducted in the UH pressure facility to detect whether the presence of an interfacial oil film affects the transformation of hydrocarbon gas bubbles into solid hydrates in a simulated deep ocean environment.

II.1.2.1 Gas Hydrate Formation: Background and Approach

Natural gas hydrates were discovered over a century ago and have been the subject of numerous studies. During the first half of this century, hydrate blockage of gas pipelines posed a serious problem and extensive research was undertaken to develop solutions. Once solutions were identified and implemented, interest waned. Recently, field studies have revealed that seabed and permafrost deposits of natural gas hydrates represent an enormous untapped energy resource (Kvenvolden, 1988; Kvenholden *et al*., 1993; Gornitz & Fung, 1994). Estimates of the total volume of hydrocarbons locked in hydrate deposits worldwide range widely from about 10^5 trillion standard cubic feet (TCF) to 2.7 x 10^8 TCF (i.e., 2.8 x 10^{15} to 7.6 x 10^{17} m^3). Hydrates also pose an immediate and formidable nuisance to offshore oil and gas operations in deep water (Max & Cruickshank, 1999; Cruickshank & Masutani, 1999). The resource potential and safety problems associated with natural gas hydrates, as well as certain military and environmental issues, have led to the initiation of major national R&D programs in Japan, India, Germany, and the U.S. (Cruickshank & Masutani, 1999; Masutani *et al.*, 2000).

The crystalline structure and mechanics, thermodynamics, and kinetics of natural gas mixtures and the pure components of natural gas (e.g., hydrocarbons; CO_2; N_2, etc.) have been investigated both experimentally and theoretically. Results of these studies can be found in a number of sources, including symposia proceedings and in the books by Sloan (1989) and Berecz & Balla-Achs (1983).

Natural gas comprises a mixture of hydrocarbons, N_2, CO_2, and possibly CO and several inert species. Proportions of the components can vary significantly as seen in the range of concentrations recommended by the Gas Processors Association for natural gas reference standards, Table II.1.3.

Table II.1.3 Natural gas reference standards.

	GPA Gas Reference	High Helium	High Ethane	Low BTU
Component	Component Concentration [mol%]			
Helium	0.5	0.2-2.0	---	---
Hydrogen	---	---	---	14.0
Argon	---	---	---	1.0
Nitrogen	5.0	1.6	9.0	66.5
Carbon Monoxide	---	---	---	12.0
Carbon Dioxide	1.0	0.3	0.5	5.0
Methane	70.5	Balance	71.0	0.5
Ethane	9.0	3.0	10.5	---
Propane	6.0	1.8	7.0	---
Acetylene	---	---	---	1.0
Isobutane	3.0	1.0	1.0	---
n-Butane	3.0	1.0	1.0	---
Isopentane	1.0	0.3	---	---
N-Pentane	1.0	0.3	---	---

Thermodynamic properties of natural gas and its components have been thoroughly investigated over temperatures and pressures encountered in underwater oils spills (Sloan, 1989). Formation and decomposition kinetics information also have been obtained, but these results are less general and definitive, since formation–in particular–entails a complex combination of inter-related physical transport and chemical processes. Hydrate formation is essentially a crystallization phenomena comprising the following steps: diffusion of guest molecules into the water matrix; nucleation; and crystal growth and agglomeration. Nucleation is an intristically random process that, along with diffusion and crystal growth, can be strongly affected by the specific conditions under which the hydrate forms. For the case of hydrate formation on natural gas bubbles rising through the water column, the situation is complicated by the fact that the gas-rich diffusion layer around a bubble may be constantly swept away by the relative motion of the bubble and water phases. The proximity of neighboring bubbles (e.g., wake effects) will also determine the dissolved gas concentration at any location in the bubble plume (which impacts nucleation and crystal growth). Furthermore, the nucleation film or centers may be disrupted by fluid motion and deformation of the gas-liquid interface.

Most hydrate formation (kinetics) experiments have been conducted in static cells or well-stirred reactors. With the exception of the study by Maini & Bishnoi (1981), little information is available on the transformation of natural gas into solid hydrates in the complex, dynamic environment experienced by bubbles rising through the ocean water column. The present investigation followed the approach taken by Maini & Bishnoi and observed the behavior of buoyant hydrocarbon gas bubbles trapped in a pressurized water tunnel by a downward flow of water. Direct imaging was employed to collect video data of the phenomena. To assess the apparently conflicting reports on oil suppressing hydrate formation, an apparatus was developed to inject both clean bubbles and bubbles covered with a film of crude oil into the water tunnel for the purpose of comparison.

II.1.2.1 Experimental Set-up for Gas Hydrates Tests

Hydrate formation experiments were conducted in a water tunnel submerged in the UH pressure vessel. The water tunnel employs a downward flow of water to trap buoyant natural gas bubbles in a clear viewing section visible through the pressure vessel windows. This allows long term (of the order of minutes to hours) observation of hydrate formation phenomena. In the viewing section, the downward drag force of the flowing water offsets the upward buoyancy of the bubble, preventing further ascent. The droplet remains (relatively) stationary in the observer's frame of reference but continues to experience the flow of water past it that it would during an unrestricted ascent.

An apparatus was developed to inject clean and oily bubbles of 3 different mixtures of hydrocarbon components of natural gas into the water tunnel. A pair of digital video cameras were used to record the behavior of the bubbles. The primary components of the experimental facility included:

1. a pressurized, downward-flowing water tunnel with a clear conical polycarbonate viewing section.

2. An instrumented steel pressure chamber in which the water tunnel was submerged.

3. Clean and oily bubble generator comprising bottled gases and regulators, a pair of manual pressure generators, valves and pressure gauges, and a 0.775 mm (0.0305 in.) i.d. orifice injector.

4. Video system consisting of 2 tripod-mounted Sony Mini-DV video cameras (models DCR-TRV900 and DSR-PD100) and video lamps. Recordings were made with the cameras fitted with wide-angle conversion lenses that allowed better close-up views of the bubbles.

II.1.2.1.1 Pressurized Water Tunnel and Bubble Generator

Photographs of the water tunnel prior to and during installation in the pressure vessel are presented in Figures II.1.14 and II.1.15, respectively. Figure II.1.16 shows the pressure vessel and components of the external water circulation loop. A schematic diagram of the system is provided in Figure II.1.17.

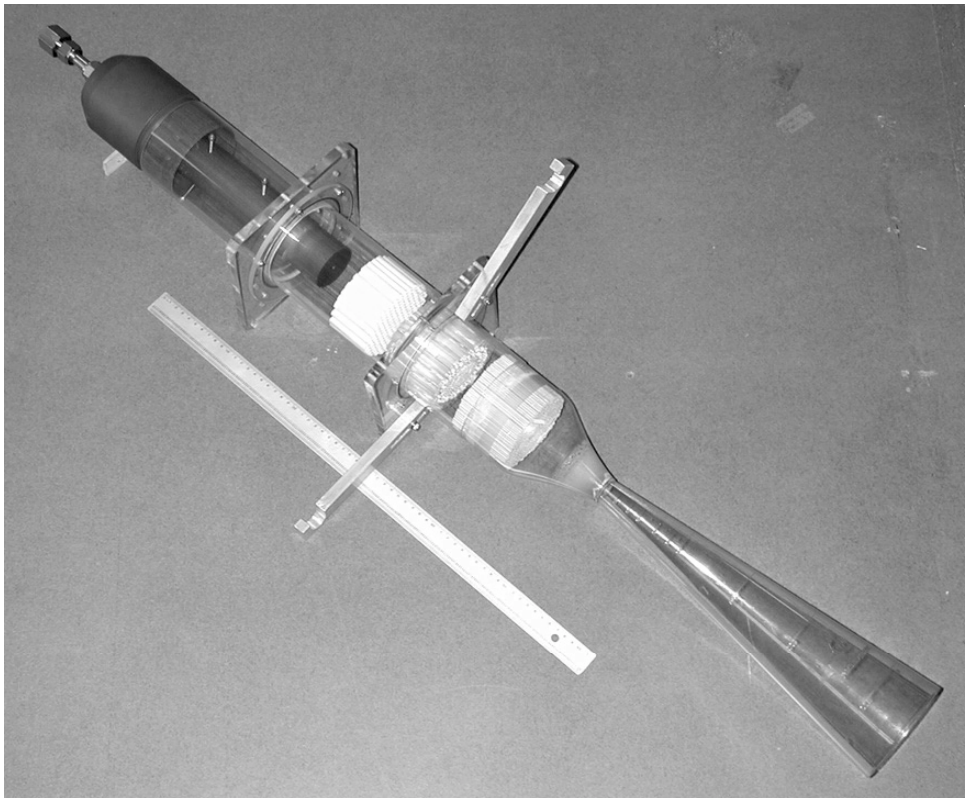

Figure II.1.14 Photograph of the water tunnel. The clear PVC plenum (upstream of the contraction and conical viewing section) has an outside diameter of 10.1 cm (4 in.).

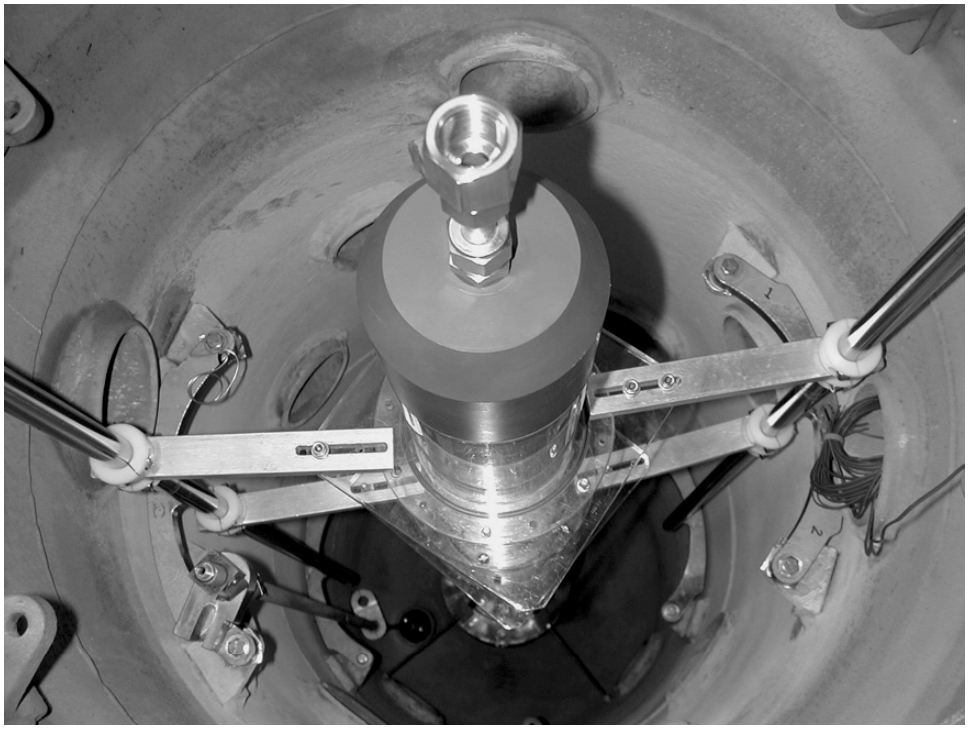

Figure II.1.15 Photograph of the water tunnel mounted inside the pressure vessel.

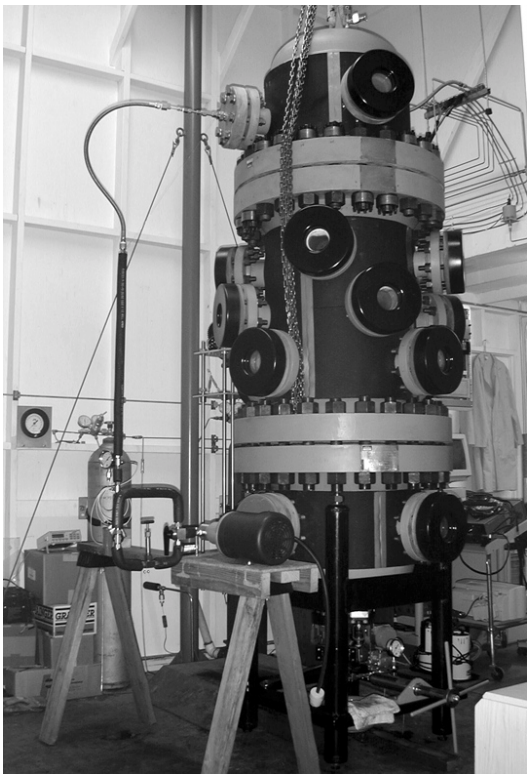

Figure II.1.16 Photograph of the pressure vessel showing the gear pump (on the sawhorse) and other components of the water tunnel water circulation loop.

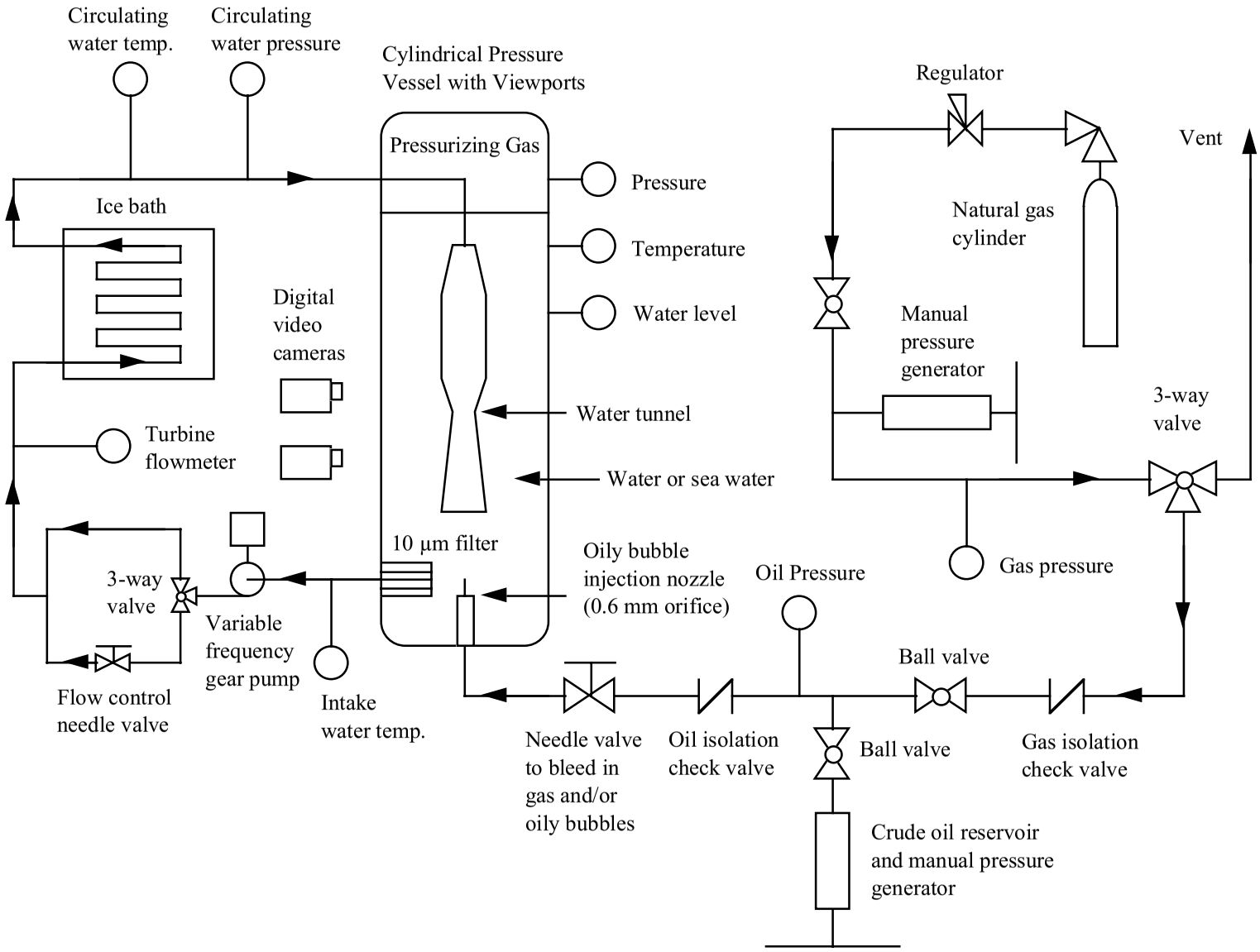

Figure II.1.17 Schematic diagram of the water tunnel and bubble generator.

The water tunnel and water circulation loop were originally designed and constructed to investigate liquid CO_2 droplet dissolution and hydrate formation in a simulated deep ocean environment and needed to be modified to accommodate the significantly greater buoyancy of natural gas bubbles (the density of liquid CO_2 is about 20 times that of CH_4 at 61 MPa and 5°C). This required increasing the flow rate capacity of the system and operating the water tunnel at higher velocities and water turbulence levels.

The water tunnel is mounted on the centerline of the UH pressure vessel and aligned so that the top of the conical viewing section can be seen through the second row of pressure vessel windows. Due to water flow rate limitations, bubbles large enough to be imaged well with the video system tend to stabilize in the top 5-7 cm of the viewing section where velocities are highest.

The steel pressure vessel consists of three sections fabricated out of 24 inch schedule 80 pipe components. The 2.46 m tall vertical cylindrical vessel has an inside diameter of 54.8 cm (21.56 in.). Optical access to the interior of the vessel is provided by five rows of high pressure, annealed and polished acrylic windows. During experiments, the vessel is partially filled with fresh or sea water chilled to a temperature representative of the depth being simulated and pressurized by charging the space above the water with N_2 or argon gas. Pressures up to 6.3 MPa and temperatures as low as 0°C can be attained in the facility. Instruments continuously monitor water level and internal temperature and pressure. Additional details can be found in Masutani *et al*. (1993).

During operation, the pressure vessel usually contains between 490 to 570 liters (130 to 150 gallons) of water. Pressurized water from the vessel is drawn through a 10 μm filter connected to a penetration in a solid flange substituted for one of the bottom windows by a Micropump Series 2200 pulseless, magnetic drive gear pump coupled to a Leeson variable speed 1 hp motor (similar to the unit used in the oil breakup tests). Flow rate is set by adjusting the pump motor speed and a metering valve and monitored with a calibrated turbine flowmeter. To compensate for heat added by the pump and from the ambient air, the stainless steel water lines are routed through a manually-agitated ice (or dry ice) bath. A pair of thermistors are employed to measure the temperature of water exiting the pressure vessel and downstream of the ice bath. Water pressure in the line is monitored with a pressure gauge.

The water enters the pressure vessel through a penetration in another solid steel flange mounted on the upper row of windows and flows through flexible tubing into the water tunnel. The water tunnel comprises four sections: (1) a compact diffuser with perforated plates and screens installed to prevent flow separation; (2) a constant area plenum section constructed from 10.2 cm (4 in.) o.d. x 0.32 cm (1/8 in.) wall clear PVC tubing containing a bluff body mounted on centerline followed by flow operators (honeycombs and grids); (3) a plastic axisymmetric contraction with a 14:1 area ratio; and (4) a conical, clear polycarbonate viewing section constructed from an Imhoff settling cone with a 12.4° included angle and an exit diameter of 10.8 cm (4.25 in.). The bluff body produces a slight velocity deficit in the center of the flow surrounded by a ring of higher velocity that serves as a barrier to inhibit bubbles from migrating into the wall boundary layer where they can ascend into the nozzle or attach to the wall. The conical geometry of the viewing section provides a streamwise gradient in velocity that

minimizes the need to adjust pump flow rate to compensate for the changing buoyancy of the dissolving bubbles.

The exit of the viewing section is positioned directly above the bubble injector. To ensure that bubbles enter the viewing section and are not swept to the side by the exiting flow of water, the injector and the lower portion of the viewing section are enclosed by a sheath device shown in Figure II.1.18. The sheath sits on the bottom of the pressure vessel. The injector enters through a 10 cm diameter opening in its base. The bottom of the viewing section slips through a circular opening in the screen clamped to the top of the clear Lexan tube. Water from the water tunnel discharges through the screened annulus between the viewing section wall and the tube and through perforated PVC sheets at the base of the assembly. The sheath also traps oil droplets released by the oily bubble generator that might otherwise escape and deposit on the walls and windows o0f the pressure chamber

.

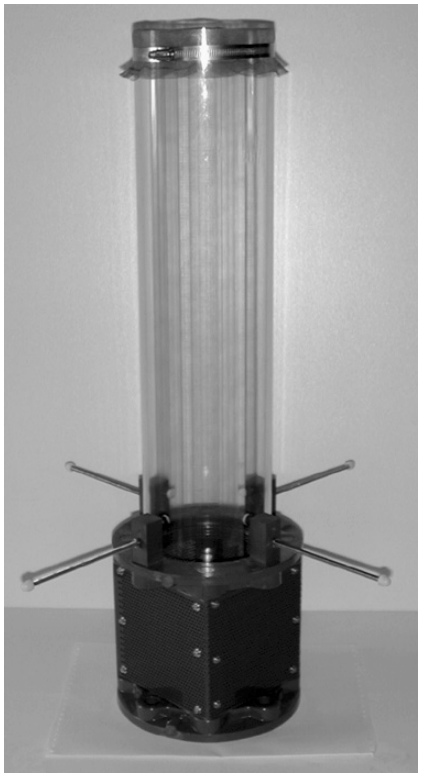

Figure II.1.18 Photograph of the sheath device that fits around the exit to the water tunnel and the bubble injector nozzle.

The bubble injection system developed for this project and shown in Figure II.1.17 can generate both clean and oily hydrocarbon bubbles. Three gas mixtures were tested: (1) 100% CH_4 (methane); (2) 90% CH_4 + 10% C_2H_6 (ethane); and (3) 70% CH_4 + 20% C_2H_6 + 10% C_3H_8 (propane). To generate clean bubbles, the needle valve upstream of the nozzle and the ball valve at the exit of the oil pressure generator are closed and the lines are pressurized with gas from a cylinder. The 3-way valve is then used to isolate the system from the cylinder and pressure is increased with the manual pressure generator (High Pressure Equipment model 87-6-5). Gas bubbles are bled through the injector mounted at the base of the pressure vessel using the needle valve. Figure II.1.19 presents photographs of the injector prior to installation. The injector is

fabricated from thick wall 25.4 mm (1.0 in.) diameter stainless steel tubing and marine bronze. Gas and oil discharge through a short length of 0.775 mm (0.0305 in.) i.d. (i.e., 1.59 mm (1/16 in.) o.d. x 0.41 mm (0.016 in.) wall) stainless steel tubing.

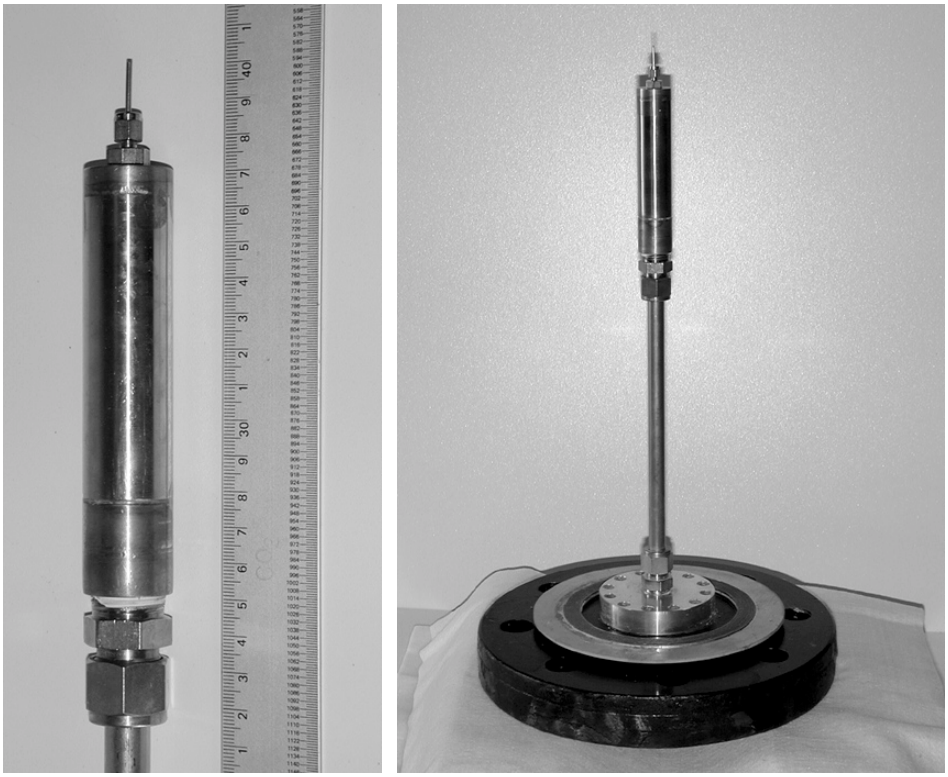

Figure II.1.19 Photographs of the bubble injector nozzle. The scale in the close-up photograph on the left is in mm. The photograph on the right shows the injector mounted on a flange that is bolted to an opening in the bottom of the pressure vessel.

To produce oily bubbles, the section between the gas isolation check valve and the needle valve is filled with oil and pressurized using a hand actuated hydraulic pump calibrator. The pressure of the gas upstream of the oil is increased with the manual pressure generator until the isolation check valve cracks and gas flows into the oil. The needle valve then is opened and gas and oil flow into the injector nozzle. After a quantity of oil discharges through the injector into the water, the gas is further pressurized until the check valve between the gas and oil legs opens again. Gas flows downs the lines and pushes through the small 0.57 mm i.d. tube mounted at the exit of the injector. Oil that had coated the inner surfaces of the tube is drawn along by the gas and forms a film that encloses the resulting bubble.

As mentioned previously, the water tunnel originally was designed to stabilize liquid droplets of CO_2 and needed to be modified to accommodate the more buoyant gas bubbles. While the liquid CO_2 droplets (and oil droplets) can be held relatively stationary, the gas bubbles tend to jump about, with rapid vertical excursions of 5-10 cm not being uncommon. These erratic movements may be due to a number of factors including deformation of the bubbles that alter drag characteristics coupling to small unsteadiness in the water flow rate. The problem is exacerbated by the fact that the bubbles need to be at least several millimeters or more in diameter in order to

be imaged well with the available video camera lenses. Bubbles of this size tend to deform readily. Furthermore, since the water flow rates that can be sustained by the pump are limited, such bubbles tend to stabilize just downstream of the exit to the contraction where velocities and the streamwise and radial velocity gradient are highest.

Although bubble movement was a nuisance, it did not seriously affect the ability to obtain quality video data.

II.1.2.3 Experimental Procedures and Data Reduction for Gas Hydrates Tests

The typical procedure followed during the gas hydrates experiments consisted of the following steps:

1. About 570 liters (150 gallons) of tap water or synthetic sea water are chilled with ice to a nominal temperature of about 0° C in a large stainless steel tank. Synthetic sea water is prepared by adding BioSea aquarium mix (chemical analysis available at www.aqcraft.com) to the tap water until the salinity (measured with an Orion portable conductivity meter) reaches 35 part per thousand. As mentioned in Section II.1.1.3, turbidity of the synthetic sea water was a problem; of three attempts made on different days, acceptable video data was obtained successfully only once.

2. The water is pumped into the pressure vessel until the water tunnel inside is completely submerged (water level slightly above the upper pressure vessel flange). (This process is usually repeated twice: cold tap water is pumped in first to cool down the pressure vessel; the water is then drained back into the stainless steel tank and chilled again; aquarium mix is added at this point if synthetic sea water is to be used; the final filling process then takes place). During the filling process, the gear pump is run at low speed to help expel air from inside the water tunnel and lines.

3. With the gear pump running, pressure in the vessel is increased slowly by flowing inert gas (usually N_2) into the space above the water until a predetermined set point is reached. Any residual gas in the water tunnel is compressed and goes into solution or is advected away. An electronic process control system vents some of the inert gas when pressure rises above the set point and the gas supply regulator is adjusted to flow if pressure falls below the set point. These two systems operate against each other to maintain pressure within a small band (between ± 1 to 2%) around the set point.

4. Two digital video cameras fitted with wide-angle conversion lenses are positioned in front of adjacent windows of the row of viewports immediately above the bottom pressure vessel flange. The two cameras view the bubbles at right angles. The camera clocks are synchronized with a handheld digital stopwatch/clock (the videos are all time stamped).

5. Clean or oily bubbles are injected into the water tunnel viewing section following procedures described in the previous section. Water flow rate is adjusted to stabilize the bubbles in the field of view of the video cameras. The external ice bath chiller is continuously agitated to increase heat transfer from the water flowing through the cooling coils.

6. Video is recorded continuously with the two cameras. Meter and gauge readings of water temperatures, pressures, water level, flow rates, etc. are recorded at 60 second intervals, noting the corresponding time indicated by the reference stopwatch/clock to allow direct comparison with the time stamped video tapes.

7. At the end of the test, the vessel is de-pressurized and the water is drained and discarded.

All three gas mixtures were typically tested during the course of a run. After switching gas cylinders, the system (that had already been vented) was purged with the new gas to eliminate any remaining trace of the previous gas mixture.

Two crude oils were employed in these experiments: Platform Gail and Neptune SPAR. When the oil was switched, the injection system needed to be disassembled and flushed and cleaned with solvent and detergent to avoid cross contamination.

Although, under static conditions, heat transfer from the surroundings slowly increases the temperature of the water in the insulated pressure vessel, cooling provided in these tests by flowing water through the ice bath proved to be very effective in maintaining stable temperatures. It should be noted that water flowing through the water tunnel is not continuously recirculated, but discharges from the exit of the conical viewing section back into the pressure vessel where it mixes with the surrounding water.

Still video images were captured from the recordings. Image adjustment, filtering, and enhancement were performed using Adobe Photoshop and the public-domain NIH Image programs.

II.2 Studies at MIT

MIT researchers conducted stratified experiments in a tall, stagnant tank (1.2 m wide by 1.2 m long by 2.4 m deep) and conducted crossflow experiments (some including stratification) in a long flume (0.8 m wide by 20 m long by 0.8 m tall). Results from the experiments were analyzed in non-dimensional space so that they could be applied at the field-scale.

II.2.1 Experiments in Stratification

Experiments were conducted in stratification to observe whether fine oil droplets would strip from the rising plume and become trapped in the intrusion layers. The results of this work were presented at the meeting of the Deep Spills Task Force in Honolulu, HI in February of 1999.

II.2.1.1 Experimental Set-up for Stratification Tests

The experimental facility used in the stagnant-stratified experiments is composed of the following components:

1. 1.2 m by 1.2 m by 2.4 m tall glass-walled tank.

2. Tanks and piping for the two-tank stratification method for producing step- and linearly-stratified ambient conditions. The standard stratification is generated using table salt that results in a density difference from bottom to top of 25 Kg/m^3.

3. Buoyancy sources which include four different air diffusers and two oil diffusers.

4. Lighting systems, including a virtual point source light for shadowgraphs and a 6 W argon-ion laser for laser-induced fluorescence (LIF) imaging.

5. Imaging system, including a digital, progressive scanning CCD camera, computerized frame grabber, and image acquisition and analysis software.

6. Dye injection method using a metering pump and a collar diffuser.

7. Density profiling system using a Head Conductivity and Temperature (CT) probe and an Ocean Sensors OS300 CT probe mounted to a linear actuator for accurate positioning.

8. Dye profiling system using an in-situ Chelsea fluorometer mounted to an Ocean Sensors OS200 Conductivity, Temperature, and Depth (CTD) probe.

9. Systems integration software using the LabView graphical programming language and Windows NT.

In comparison with previously reported experiments, this apparatus allows us to extend the parameter range of our experiments to better match field conditions for a well blowout, and in addition, provides novel measurements of flow rates in the intrusion layers for model calibration.

The facility used in stratified experiments with crossflow is described in Section II.2.2.1.

II.2.1.2 Analytical Techniques for Stratification Tests

Analytical techniques included direct visual observation, image processing of video images, analysis of the salinity and dye profiles before and after experiments, and a correlation analysis in non-dimensional space.

Figure II.2.1 illustrates three types of plume behavior, introduced by Asaeda & Imberger (1993), along with a new plume type identified by our experiments. Type 1 plumes have no subsurface intrusions, and all the entrained water is carried to the reservoir surface (these plumes are generally not applicable to deep ocean scenarios). Type 2 plumes have one or more subsurface intrusions, each forming a distinct intrusion layer as entrained water periodically leaves the plume (called plume peeling). Type 3 plumes have a continuous set of intrusions as entrained water continuously peels and gets re-entrained by the rising bubble column. Our new plume type, Type 1*, has a distinct initial intrusion that significantly alters the inner bubble core,

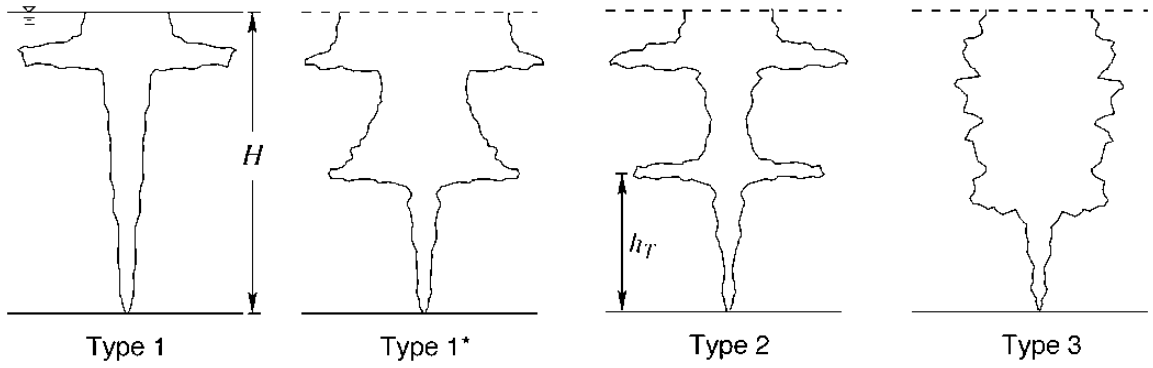

Figure II.2.1 Schematics of the various plume types. H is the total depth for a Type 1 plume and h_T is the intrusion depth (or trap height) of the first intrusion.

carrying droplets down toward the intrusion layer and forming a diffuse, Type 3-like plume in the subsequent intrusions. Type 1* plumes represent the case where oil would be trapped in the intrusion layer and not immediately follow the associated gas to the surface.

From direct visual observation, the plume type was documented for a wide range of air and oil bubbles/droplets, flow rates, and stratification strengths. Image processing of the video images and analysis of the salinity and dye profiles provided quantitative measures of the height of the first intrusion layer and the volume flux of peeled fluid into the intrusion.

Non-dimensional numbers were used to scale the laboratory results to the field. Considering an oil plume in a stratified, stagnant ambient, the important independent variables are the buoyancy flux, $B = g\, Q_0\, \Delta\rho/\rho$ (where Q_0 is the oil flow rate, and $\Delta\rho$ is the density difference between a reference ambient density, ρ, and the oil), the slip velocity (or terminal velocity) of the bubbles, u_s, and the stratification strength, measured by the buoyancy frequency, $N = [(-g/\rho)(\partial\rho/\partial z)]^{1/2}$. An important dependent variable is the trap height of the first intrusion, h_T. Forming the appropriate non-dimensional groups, the Buckingham Π Theorem gives:

$$\frac{h_T}{(B/N^3)^{1/4}} = f\left(\frac{u_s}{(BN)^{1/4}}\right). \qquad \text{(II.2.1)}$$

The left-hand side of (II.2.1) is the ratio of the trap height to the characteristic plume length scale, $l_C = (B/N^3)^{1/4}$. The variable on the right hand side of (II.2.1) is the ratio of the slip velocity to the characteristic plume fluid rise velocity taken at the trap height. We have named this non-dimensional slip velocity $U_N = u_s/(BN)^{1/4}$.

Another important dependent variable is the intrusion layer flux, Q_i. By a similar use of the Buckingham Π Theorem, we expect the relationship:

$$\frac{Q_i}{(B^3/N^5)^{1/4}} = f\left(U_N\right). \qquad \text{(II.2.2)}$$

The left-hand side of (II.2.2) is the ratio of the intrusion layer flux to a characteristic plume flow rate at the trap height; the right-hand side is U_N.

The final dependent variable of interest is the characteristic plume type. Since the plume type is a non-dimensional attribute, we expect it to depend simply on U_N:

$$\text{Plume type} = f\left(U_N\right). \tag{II.2.3}$$

Section III.2 presents the results of correlating the trap height, the intrusion layer flux, and the characteristic plume type with U_N.

II.2.2 Experiments in a Crossflow

Experiments in a crossflow were conducted to visualize how multi-phase plumes differ from single-phase plumes and to provide the insight necessary to improve integral model predictions for multi-phase plumes in crossflow. The preliminary results of the crossflow experiments were reported in two interim reports in September and October of 1999 entitled: "Final Report: Exploratory Experiments with Droplet Plumes in a Crossflow" and "Report Summary: CORMIX 3.2 Analysis of Droplet Plumes in a Crossflow." These reports are provided in Appendices B and C.

II.2.2.1 Experimental Set-up for Crossflow Tests

Several systems designed for the stratified experiments were used in the crossflow experiments. These included the buoyancy sources, the lighting and imaging systems, and the dye injection method. Additional components of the crossflow experiments included:

1. 0.8 m wide by 20 m long by 0.8 m deep glass-walled flume.

2. 10 hp recirculation pump. The flow rate is controlled by an upstream gate valve and measured using a calibrated orifice meter. An upstream flow-straightener was used to create a uniform, horizontal current. Flowing full, the pump generates velocities of 2 to 16 cm/s.

3. Towing mechanism to simulate a current by towing the diffusers along the flume bottom. The towed carriage achieves velocities from 2 to 22 cm/s.

4. For stratified crossflow experiments, bulkheads were installed upstream and downstream of a test section, and the water was stratified between the bulkheads using the two-tank method. The towing mechanism was used to create the current in the stratified case.

Similar experiments (without stratification) were conducted by Hugi (1993) at the Swiss Federal Institute of Technology in Zurich (ETH). Our experiments extend those conducted by Hugi (1993) by reducing the crossflow velocity and observing the critical height at which the plume diverges from integral behavior (i.e. the height where entrained fluid separates from the rising bubble column). More details of the apparatus can be found in Appendix B.

II.2.2.2 Analytical Techniques for Crossflow Tests

Similarly to the stratified experiments, the analytical techniques included direct visual observation, image processing of video images, and correlation analysis in non-dimensional space.

Analysis of the observations and video images allowed a comprehensive qualitative description of multi-phase plume behavior in a crossflow. Of particular interest was the critical height at which entrained fluid separated from the rising bubble column. Above this height, a traditional integral plume model should not be applied.

This critical transition height can be predicted by correlating with appropriate non-dimensional numbers. For a multi-phase plume in a crossflow (without stratification), the important parameters are the ambient crossflow velocity, u_a, the transition height, h_{cr}, the buoyancy flux, B, and the slip velocity, u_s. Invoking the Buckingham Π Theorem again gives:

$$\frac{u_a}{(B/h_{cr})^{1/3}} = f\left(\frac{u_s}{(B/h_{cr})^{1/3}}\right). \qquad \text{(II.2.4)}$$

The left-hand size of (II.2.4) is the ratio of the current velocity to the characteristic plume fluid rise velocity at the critical transition point, $u_C = (B/h_{cr})^{1/3}$. Similarly, the parameter on the right hand side is the ratio of the slip velocity to u_C. Measured transition heights were correlated to u_s, u_a, and B using the relationship in (II.2.4).

II.2.2.3 Modeling Approach

The interim report entitled "Report Summary: CORMIX 3.2 Analysis of Droplet Plumes in Crossflow" presented a survey of modeling techniques for these multi-phase plumes using the single-phase model CORMIX (the Cornell Mixing Zone Model). The report found that traditional integral techniques worked well in the multi-phase case up to the critical transition height, h_{cr}, but did not follow either the bubbles or the entrained fluid above h_{cr}.

By direct observation of the experiments, it appears that the entrained fluid is accelerated upward by the bubbles over a height h_{cr} and then advected downstream of the bubbles by the ambient crossflow. The separated fluid continues to rise in the far field (after separation) due to the excess momentum present when separation occurs. A new modeling algorithm is, therefore, proposed:

1. Simulate the combined oil and air plume from the origin to the height h_{cr} using a traditional integral model approach.

2. Simulate the separated oil and entrained fluid plume alone in the far field (neglect the air bubbles). The initial volume, momentum, and buoyancy fluxes for this separated plume are predicted by the traditional model at the height h_{cr}.

3. Simulate the bubbles by the vector addition of their group rise velocity and the ambient current (add random walk effects if dispersion of the gas bubbles is of interest).

4. If the plume consists of bubbles/droplets having a range of slip velocities, a critical height for each size class could, in principle, be calculated. The model would then simulate multiple separations with the fractionated bubble/droplet classes each migrating upward according to their own slip velocity.

The plume parts of the above calculations could be preformed with the model of Yapa & Zhang (1999), though this should be tested against data. Preliminary results to substantiate this approach for a single separating dispersed phase are presented in Section III.2.3.

III RESULTS AND DISCUSSION

Results of the experiments and analyses conducted at UH and MIT are presented and discussed in this section.

III.1 UH Results

Experiments were conducted at UH to investigate oil jet breakup into a dispersed droplet phase and hydrate formation on clean and oily bubbles of the major hydrocarbon components of natural gas. The objectives of these experiments and descriptions of the facilities and procedures that were employed have been described previously in this report.

III.1.1 Jet Break-up

Table III.1.1 summarizes the fifteen cases that were examined in the jet breakup experiments. Four deepwater crude oils and a stable analog fluid (i.e., polydimethylsiloxane silicone fluid) were tested. The ambient liquid was either tap water or natural sea water chilled to a nominal temperature of 18°C (65°F). Three of the test cases also examined the break up of jets discharging into (nominal) 7°C (45°F) tap water. The ratio of ambient liquid and jet fluid densities fell within the range: $1.022 \leq \rho_{ambient}/\rho_{jet} \leq 1.191$. Three injection nozzles were employed with ASME sharp edged orifice diameters of 1 mm, 2 mm, and 5 mm.

Table III.1.1 Test cases examined in the jet breakup experiments.

Jet fluid	Ambient fluid	Orifice diameter [mm]	Water temperature [°C]	Oil temperature [°C]
Neptune SPAR	Tap water	1	8.5	27.6
Neptune SPAR	Tap water	1	18.5	26.8
Neptune SPAR	Tap water	2	17.6	28.6
Neptune SPAR	Sea water	2	18.4	27.2
Genesis	Tap water	2	18.1	27.7
Genesis	Tap water	5	18.9	27.2
Mars TLP	Tap water	2	18.3	26.9
Mars TLP	Tap water	5	16.8	28.2
Platform Gail	Tap water	1	17.7	27.3
Platform Gail	Tap water	5	18.0	27.9
Silicone fluid	Tap water	1	5.4	26.0
Silicone fluid	Tap water	1	19.2	28.0
Silicone fluid	Tap water	2	7.4	25.5
Silicone fluid	Tap water	2	20.3	26.0
Silicone fluid	Tap water	5	19.2	27.5

For each test case, PDPA and video data were collected over a range of jet velocities. A single case typically required a full day to complete, with most of the time spent on preparation and clean up.

III.1.1.1 Instability Regimes

Figure III.1.1 illustrates the progression in the mode of breakup that was observed as oil discharge velocity was increased, while holding all other conditions constant. These video images correspond to the case of Genesis oil injected into tap water at 18.1°C through a 2 mm diameter orifice. Similar results were obtained in all test cases examined in this study.

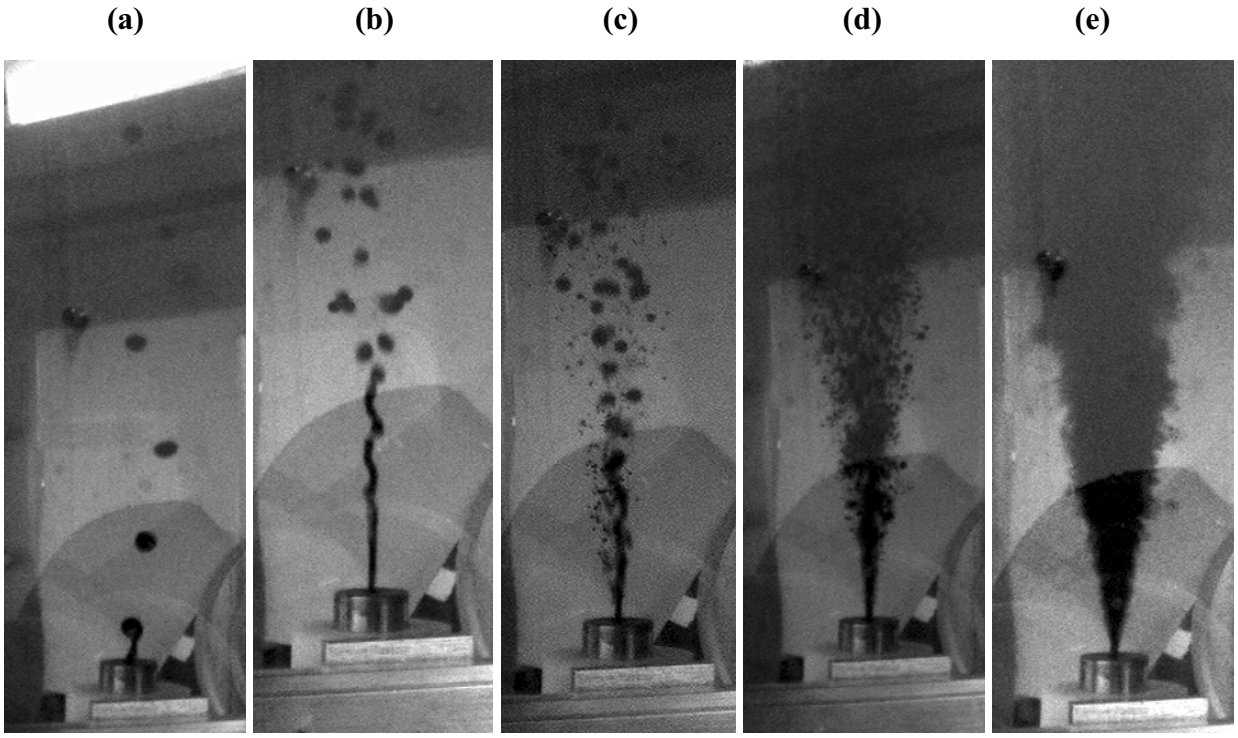

Figure III.1.1 Different modes of jet breakup observed during the oil injection experiments. Jet velocity increases from left to right. Images correspond to the case of Genesis crude oil injected into tap water at 18.1°C through a 2 mm diameter orifice. As a point of reference, the nozzle o.d. is about 2.5 cm.

At low velocities, Rayleigh instability dominates, producing a near monodispersion of droplets much larger than the orifice (note that the outer diameter of the nozzle shown in the pictures is about 2.5 cm). Jet breakup initially occurs near to the nozzle. As velocity is increased, the breakup location moves away from the nozzle and at some point the instability changes to the sinuous mode which will be referred to hereinafter as Type I. This sinuous instability generates a narrow polydispersion of relatively large droplets. At higher velocities, two instability mechanisms appear to operate in parallel: the surface of the jet becomes unstable to short wavelength disturbances and disintegrates close to the nozzle into fine droplets, while the core of the jet persists as a continuous fluid filament that breaks up further downstream into large droplets. These two distinct instability mechanisms result in a polydispersion of droplets,

initially comprising two different size groups. We will refer to condition (c) in Figure III.1.1 as a Type II instability. Raising the velocity moves the breakup location of the jet core filament closer to the nozzle and also increases the fraction of fine droplets. This near-atomization condition is shown as (d) in the figure. Finally, atomization is attained; however, the dense cloud of fine droplets on the perimeter of the jet obscures its interior. It could not be determined visually whether breakup of the core filament persists and continues to produce relatively large droplets when the jet appears as depicted in frame (e).

Figure III.1.1 demonstrates that the mode of breakup determines the droplet size distribution. Following conventional practice (see, for example Figures II.1.1 and II.1.2 and the related discussion in Section II.1.1.1), the evolution of jet breakup length, L, was examined to establish the limits of the different instability regimes for crude oil discharging into water. Estimates of L were obtained through analyses of video data and are presented in Table III.1.2. The table also lists values of Re_D and *We*, as well as breakup length non-dimensionalized using the corresponding orifice diameter, D.

Even in the Rayleigh instability regime, small variations in oil flow rate and other factors can result in breakup occurring over a range of distances from the orifice at a given test condition. This introduces uncertainty into the measured values of L. An example of the problem is shown in Figure III.1.2 where L varies by about 80% in three video frames taken during the same test.

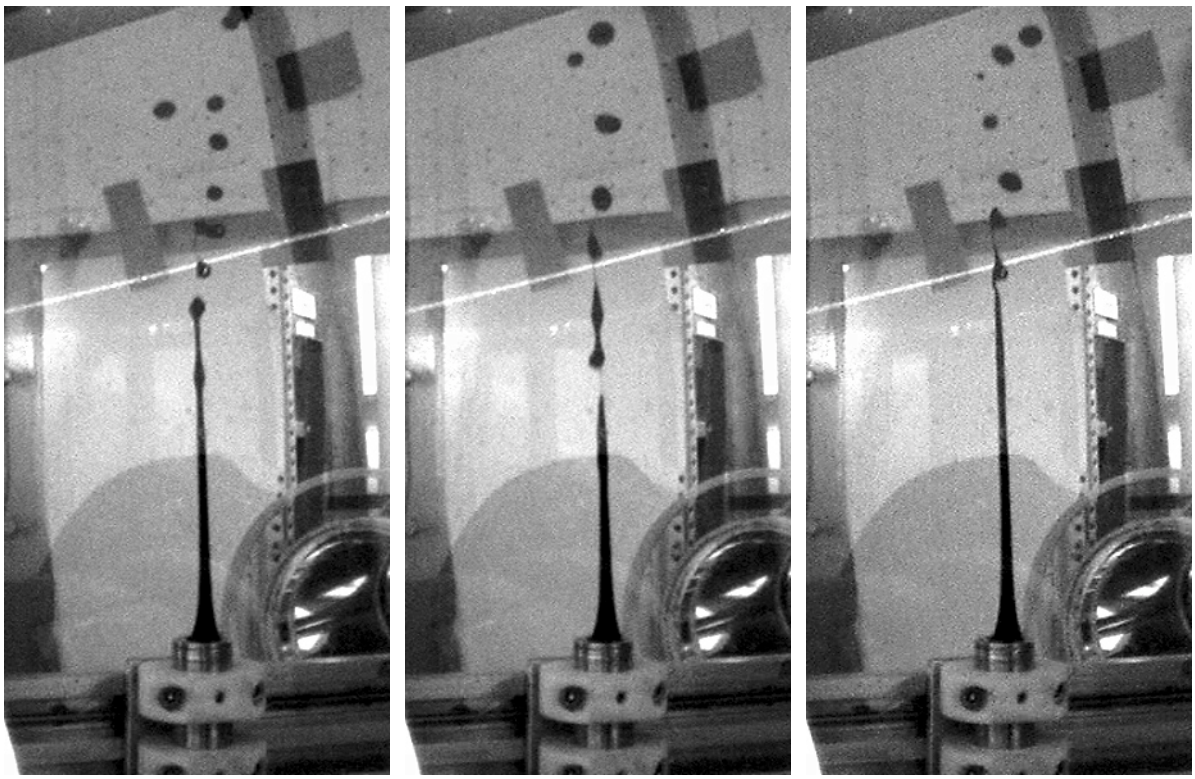

Figure III.1.2 Variation in jet breakup length at a fixed test condition. The video frames show Platform Gail oil being injected into water through a 5 mm diameter orifice. The bright diagonal line near the top of the pictures is the PDPA laser beam.

Table III.1.2 Jet breakup lengths for four deepwater crude oils.

Case	Water Temp. [°C]	Oil Temp. [°C]	Jet Velocity [m/s]	Re_D	*We*	L [cm]	L/D
G2T	18.0	27.6	0.308	3.382E+01	6.397E+00	2.2	10.8
G2T	18.0	27.6	0.403	4.425E+01	1.095E+01	2.0	10.1
G2T	18.0	27.6	0.753	8.281E+01	3.835E+01	4.6	23.0
G2T	18.4	27.8	0.281	3.122E+01	5.341E+00	1.6	7.9
G2T	18.4	27.8	0.340	3.770E+01	7.788E+00	2.0	10.2
G2T	18.4	27.8	0.340	3.770E+01	7.788E+00	3.3	16.3
G2T	18.4	27.8	0.435	4.830E+01	1.279E+01	3.5	17.4
G2T	18.4	27.8	0.716	7.952E+01	3.465E+01	4.5	22.4
G2T	18.4	27.8	0.966	1.072E+02	6.298E+01	5.1	25.4
G5T	19.2	26.9	0.085	2.255E+01	1.218E+00	1.5	3.1
G5T	19.2	26.9	0.161	4.284E+01	4.396E+00	2.6	5.1
G5T	19.2	26.9	0.252	6.697E+01	1.074E+01	3.0	5.9
G5T	19.2	26.9	0.357	9.470E+01	2.148E+01	4.1	8.1
G5T	19.2	26.9	0.441	1.172E+02	3.293E+01	7.6	15.2
G5T	19.2	26.9	0.637	1.691E+02	6.850E+01	8.1	16.2
M2T	18.4	27.0	0.286	2.272E+01	5.579E+00	2.5	12.4
M2T	18.4	27.0	0.645	5.112E+01	2.825E+01	6.1	30.6
M2T	18.4	27.0	0.838	6.648E+01	4.777E+01	7.1	35.7
M2T	18.4	27.0	1.066	8.458E+01	7.730E+01	3.5	17.7
M2T	18.4	27.0	0.361	2.861E+01	8.847E+00	3.3	16.3
M2T	18.4	27.0	0.408	3.240E+01	1.134E+01	4.5	22.4
M2T	18.4	27.0	0.523	4.145E+01	1.856E+01	4.9	24.6
M2T	18.4	27.0	0.626	4.965E+01	2.664E+01	4.4	22.1
M2T	18.4	27.0	0.387	3.072E+01	1.020E+01	4.0	19.8
M2T	18.4	27.0	0.332	2.630E+01	7.474E+00	3.5	17.3
M5T	17.2	28.1	0.064	1.320E+01	6.882E-01	3.3	6.6
M5T	17.2	28.1	0.093	1.936E+01	1.480E+00	3.4	6.8
M5T	17.2	28.1	0.145	3.010E+01	3.578E+00	10.0	19.9
M5T	17.2	28.1	0.169	3.503E+01	4.845E+00	12.1	24.2
M5T	17.2	28.1	0.235	4.876E+01	9.388E+00	5.9	11.9
N2T	17.7	28.9	0.361	5.411E+01	8.623E+00	2.5	12.4
N2T	17.7	28.9	0.642	9.629E+01	2.730E+01	5.7	28.7
N2T	17.7	28.9	0.777	1.166E+02	4.002E+01	5.5	27.4
N2T	17.7	28.9	1.061	1.592E+02	7.459E+01	5.8	29.0
N2T	17.7	28.9	1.013	1.520E+02	6.803E+01	6.5	32.5
N2T	17.7	28.9	0.870	1.305E+02	5.016E+01	6.4	32.2
N2T	17.7	28.9	0.663	9.947E+01	2.914E+01	5.5	27.4
N2T	17.7	28.9	0.584	8.754E+01	2.256E+01	5.5	27.4
N2T	17.7	28.9	0.318	4.775E+01	6.713E+00	4.2	21.1
N2S	18.5	27.5	0.292	4.178E+01	5.649E+00	3.5	17.3
N2S	18.5	27.5	0.451	6.457E+01	1.349E+01	3.7	18.5
N2S	18.5	27.5	0.865	1.238E+02	4.961E+01	5.0	25.1
N2S	18.5	27.5	0.859	1.231E+02	4.901E+01	5.0	24.9
N2S	18.5	27.5	0.753	1.079E+02	3.765E+01	4.5	22.4

Table III.1.2 (continued)

Case	Water Temp. [°C]	Oil Temp. [°C]	Jet Velocity [m/s]	Re_D	*We*	L [cm]	L/D
P5T	17.9	27.8	0.115	3.872E+00	2.368E+00	16.1	32.2
P5T	17.9	27.8	0.075	2.500E+00	9.869E-01	14.8	29.7
P5T	17.9	27.8	0.126	4.242E+00	2.842E+00	17.6	35.1
P5T	17.9	27.8	0.194	6.491E+00	6.655E+00	13.6	27.1
P5T	17.9	27.8	0.286	9.594E+00	1.454E+01	10.6	21.2
P5T	17.9	27.8	0.398	1.335E+01	2.816E+01	13.1	26.1
P5T	17.9	27.8	0.619	2.075E+01	6.803E+01	12.9	25.9
P5T	17.9	27.8	0.340	1.139E+01	2.048E+01	12.3	24.6
P5T	17.9	27.8	0.679	2.278E+01	8.193E+01	8.3	16.6
P5T	17.9	27.8	0.441	1.480E+01	3.462E+01	15.6	31.2

Explanation of Case code:

G2T: Genesis; 2 mm orifice diameter; tap water
G5T: Genesis; 5 mm orifice diameter; tap water
M2T: Mars TLP; 2 mm orifice diameter; tap water
M5T: Mars TLP; 5 mm orifice diameter; tap water
N2T: Neptune SPAR; 2 mm orifice diameter; tap water
N2S: Neptune SPAR; 2 mm orifice diameter; sea water
P5T: Platform Gail; 5 mm orifice diameter; tap water

It should be noted that significant uncertainties also exist in the calculated values of the Weber and Reynolds numbers given in Table II.1.2 (and, hence, in Ohnesorge number, *Z*). By definition, $Re_D = f(U, D, \rho, \mu)$; $We = f(U, D, \rho, \sigma)$; and $Z = f(D, \rho, \mu, \sigma)$. Calibration reduces the uncertainty in U to approximately the accuracy of the positive displacement flow meter (± 5%). Examination of the orifices with a microscope suggests that D agrees with the nominal values to within about ± 3%. By far, the primary source of uncertainty in Re_D, *We*, and *Z* lies in the crude oil properties ρ, μ, and σ.

Unlike density and viscosity, interfacial tension, σ, was not measured as part of the analyses of the four crude oil samples performed by Environment Canada. Instead, σ was estimated from surface tension data for similar oils. A mean value of 25.9 dyne/cm was used to calculate *We* and *Z* in this study. Based on the range of values reported in the database (21.6 to 30.2 dyne/cm), the uncertainty in σ is believed to be approximately ± 17%. This potential error is dwarfed by the uncertainties in dynamic viscosity, μ, related to possible changes in oil composition due to devolatilization. Relationships provided by Environment Canada (see Appendix A) predict that between 12% (Platform Gail) and 19% (Neptune SPAR) of the oil mass could evaporate in 1 hour at the air temperatures at which the experiments were conducted. (Anticipating this problem, procedures described in Section II.1.1.3 were followed to minimize evaporation.) In the worst case, this level of evaporation would yield a modest increase in density of around 4%. Dynamic viscosity, however, could change by a factor of 14 for Platform Gail and 4 to7 for the other three oils.

ρ and μ are estimated by extrapolation from property data reported at 15°C and 25°C. Differences between temperatures measured with the thermistor in the oil supply line before it enters the water tank and actual temperatures of the oil exiting the orifice also contribute to the experimental uncertainty. A detailed heat transfer analysis was conducted to identify the maximum oil temperature change that could occur between the measurement point and the orifice due to heat transfer to the cooler water in the tank. This analysis predicted a difference of less than 3°C for the worst case of extremely low oil flow rate. The corresponding uncertainties in ρ and μ are insignificant relative to the uncertainties associated with devolatilization.

Following standard procedures (Allisy, 1980), the uncertainty in *We*, which is not a function of viscosity, is estimated to be ± 21%. Most of this uncertainty is associated with the lack of information on surface tension. Since Re_D is inversely proportional to μ, the aforementioned devolatilization effects could result in actual values of this dimensionless parameter being 1/4 (25%) to 1/14 (7%) the tabulated values that were calculated assuming negligible evaporation. This huge potential error is a major justification for the use of stable analogs such as silicone fluid. Oil samples from the closed injection system reservoir were collected and stored in glass vials at the beginning and end of each test to document evaporation; however, there were no facilities available at UH to measure crude oil viscosity.

Keeping in mind the magnitude of the experimental uncertainties, dimensionless breakup length, L/D, is plotted as a function of Reynolds number in Figure II.1.3. L/D does not appear to correlate well against Re_D. Better correlation is obtained when L/D is plotted as a function of

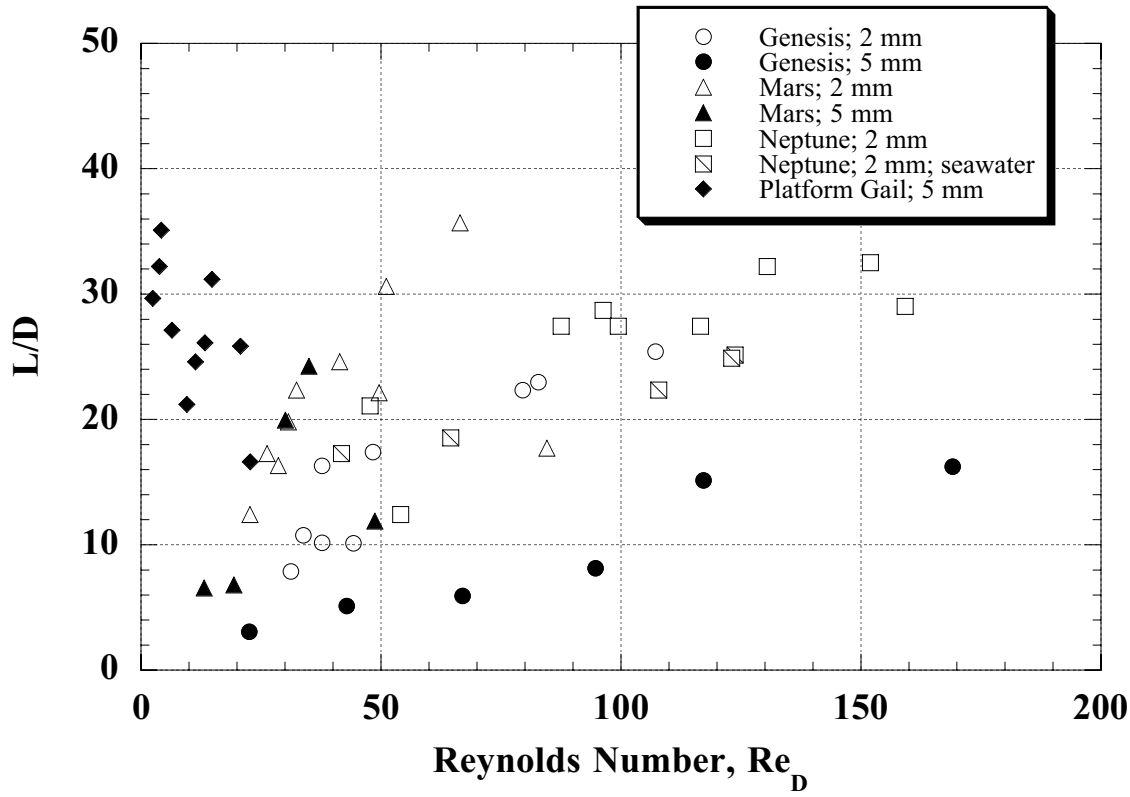

Figure III.1.3 Non-dimensionalized jet breakup length as a function of Reynolds number.

Weber number in Figure III.1.4. This figure also includes representative error bars estimated as described above. L/D appears to peak at Weber numbers between 40 and 60. Data obtained for the 5 mm diameter orifice exhibit a second peak at low values of We below 10.

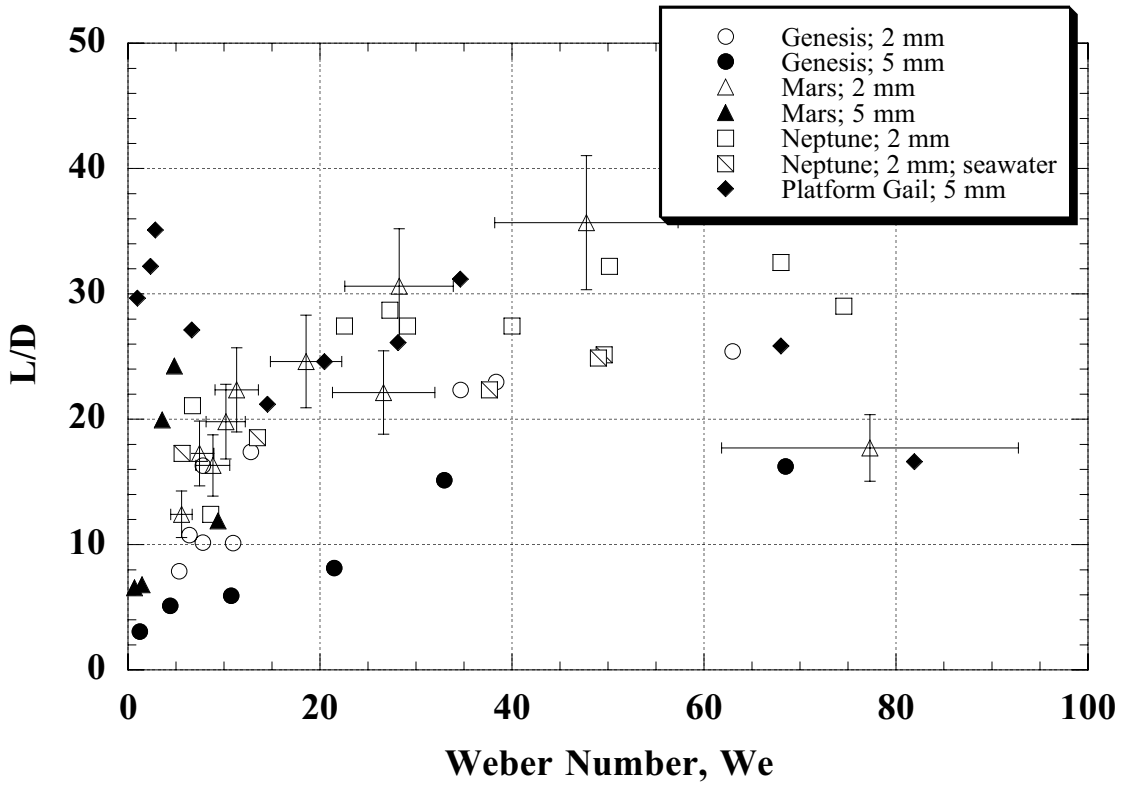

Figure III.1.4 Non-dimensionalized jet breakup length as a function of Weber number.

While some of the scatter in the results are related to uncertainties in the measurements of L/D and estimates of *We* and Re_D, it is understood that jet instability and breakup depends on a number of factors, including–but not limited to–Re_D, *We*, *Z*, and $\rho_{ambient}/\rho_{jet}$. Figures III.1.3 and III.1.4 therefore only present two-dimensional projections of a multi-dimensional surface.

Pursuing the objective of establishing the boundaries of the different instability regimes (which, it should be recalled, determine the characteristics of the droplet size distribution), the video records for all test cases were analyzed to categorize each flow condition as one of the five classes of instabilities depicted in Figure III.1.1: (1) Rayleigh; (2) Type I sinuous; (3) Type II; (4) near-atomization; and (5) apparent atomization. 170 flow conditions were evaluated and the results are presented in Figure III.1.5 as a conventional plot in dimensionless Re_D-*Z* space.

Double lines demarcating three distinct instability regimes identified as **a**, **b**, and **c** in the figure have been drafted through the data. Rayleigh instability produces a monodispersion of large oil droplets in regime **a**. In flow regime **b**, Types I and II instabilities result in a polydispersion comprising a mixture of an increasing fraction of fine droplets mixed with large drops generated by the breakup of the central jet core filament. Atomization occurs in regime **c**.

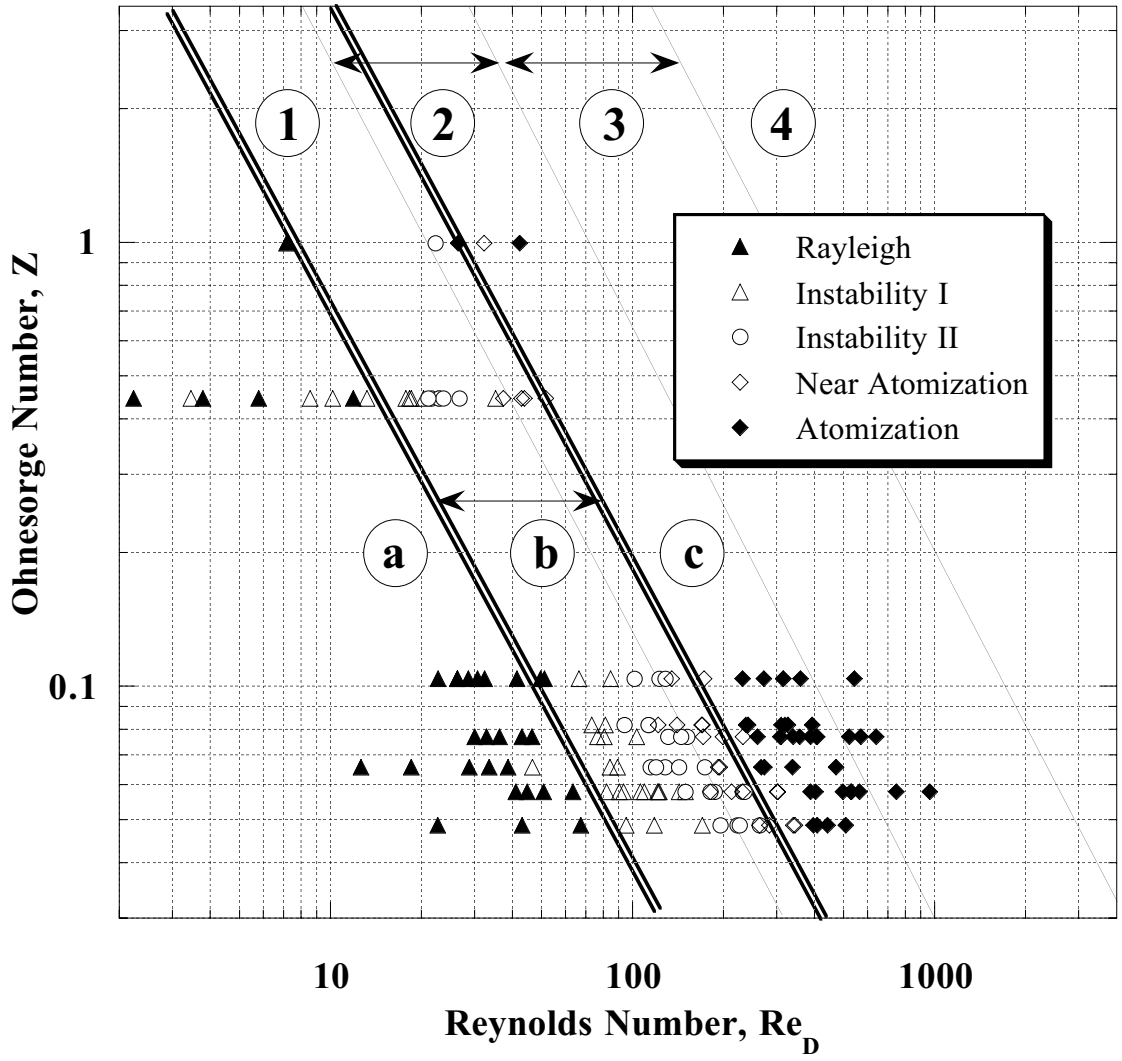

Figure III.1.5 Jet breakup instability regimes. Data points were obtained in the present study of oil injection into water. The double lines are the inferred boundaries of three breakup regimes denoted as **a** (Rayleigh), **b** (Types I and II identified in Figure III.1.1), and **c** (atomization). Solid lines are the boundaries established in previous investigations of liquid jets discharging into a gas where **1** is the Rayleigh regime, **4** is the atomization regime, and **2** and **3** correspond, respectively, to the first- and second wind-induced breakup.

Instability regime boundaries established in earlier investigations of liquid jet breakup in gas (Ohnesorge, 1936; Reitz & Bracco, 1986; Lefebvre, 1989) are included in Figure 111.1.5 for comparison. Ohnesorge (1936) proposed three regimes identified as **1**, **2**, and **3+4** in the figure wherein breakup occurs through Rayleigh instability, sinuous wave breakup, and atomization, respectively. Miesse (1955) and other researchers expanded the transitional breakup regime **2** to include a second wind-induced breakup condition (zone **3**).

Earlier studies have provided evidence that breakup of liquid jets may proceed differently in gas and in another viscous liquid. As discussed in Section III.1.1.1 of this report, Reitz (1978) observed that the instability regime boundaries may shift depending on the relative values of the densities of the jet and continuous (i.e., ambient) phases, $\rho_{ambient}/\rho_{jet}$. As shown in Figure II.1.3, there is an expectation that, at a given value of Z, transition moves to lower Reynolds numbers as $\rho_{ambient}/\rho_{jet}$ increases. Results of the present study appear to confirm this expectation. Uncertainties in Re_D and Z notwithstanding, the instability regime boundaries exhibit a significant shift to lower Re_D from the liquid-in-gas results. The relationships that define the boundaries drafted through the present data in Figure III.1.5 are:

*Boundary between regions **a** and **b**:*

$$Z = 12/Re_D^{1.24} \tag{III.1.1}$$

*Boundary between regions **b** and **c**:*

$$Z = 63/Re_D^{1.26} \tag{III.1.2}$$

The exponents of Re_D (1.24 and 1.26) are larger than the value that appears in the equation for the boundary line for atomization determined by Miesse (1955):

$$Z = 100/Re_D^{0.92} \tag{III.1.3}$$

This parameter (i.e., the slope of the boundaries in Re_D-Z space) is difficult to determine accurately since, as is apparent in Figure III.1.1, the transition point between adjacent instability regimes (particularly between near-atomization and atomization) often cannot be identified precisely.

III.1.1.2 Droplet Size Distributions

PDPA data were collected at 71 different test conditions using the four deepwater crude oils and the silicone fluid. As mentioned previously, after extensive testing and consultations with the instrument's manufacturer, different PDPA configurations were employed to conduct measurements of the crude oils and the silicone fluid. The PDPA monitored refracted light from the clear silicone droplets and reflected light from the opaque oil droplets.

Table III.1.3 summarizes the test cases that were examined and the experimental results. Jet inlet velocities were calculated by dividing the measured volumetric flow rates by the cross sectional area of the orifice that was used. Re_D, *We*, and Z were estimated following the procedures outlined previously. The PDPA collects velocity and size information for individual particles, one at a time. Statistics are determined from the collected data ensembles. The total number of samples that were collected for each case are reported in the table.

Definitions of the characteristic droplet diameters were given in Section II.1.1.1.3. The PDPA software utilizes equations II.1.5 through II.1.8 to calculate D_{10}, D_{20}, D_{30}, and D_{32}. Table III.1.3

Table III.1.3 Summary of PDPA droplet size measurements.

Case	Water Temp. [°C]	Oil Temp. [°C]	Jet Velocity [m/s]	Re_D	*We*	*Z*	No. of Samples	D_{10} [µm]	D_{10} (PVC) [µm]	D_{20} [µm]	D_{20} (PVC) [µm]	D_{30} [µm]	D_{30} (PVC) [µm]	D_{32} [µm]	D_{32} (PVC) [µm]
G2T	18.0	27.6	2.16	2.38E+02	3.17E+02	7.47E-02	2965	3569	3259	3612	3318	3639	3360	3695	3445
G2T	18.1	27.6	2.90	3.19E+02	5.67E+02	7.46E-02	2783	3570	3115	3614	3194	3643	3246	3702	3353
G2T	18.1	27.7	3.35	3.70E+02	7.58E+02	7.43E-02	2275	3543	3228	3585	3284	3610	3318	3661	3388
G2T	18.3	27.7	3.77	4.17E+02	9.63E+02	7.43E-02	1000	3396	3060	3454	3132	3486	3174	3552	3261
G5T	18.7	27.4	0.98	2.67E+02	1.64E+02	4.79E-02	3228	3091	2514	3167	2611	3226	2698	3347	2881
G5T	18.8	27.0	1.27	3.40E+02	2.74E+02	4.87E-02	3238	3316	2759	3383	2865	3432	2950	3531	3127
G5T	19.0	27.1	1.66	4.45E+02	4.63E+02	4.84E-02	2613	3310	2871	3402	3007	3458	3096	3573	3272
G5T	19.1	27.0	1.90	5.07E+02	6.11E+02	4.87E-02	1169	3392	2962	3431	3017	3462	3062	3524	3154
M2T	18.3	26.8	1.68	1.32E+02	1.92E+02	1.05E-01	3276	3630	3399	3654	3434	3669	3456	3701	3501
M2T	18.3	26.8	2.18	1.71E+02	3.22E+02	1.05E-01	2716	3613	3284	3649	3348	3671	3387	3716	3467
M2T	18.3	26.8	2.92	2.30E+02	5.79E+02	1.05E-01	2501	3561	3236	3610	3305	3638	3347	3695	3433
M2T	18.3	26.9	3.42	2.70E+02	7.97E+02	1.04E-01	2269	3522	3153	3587	3246	3623	3300	3697	3413
M2T	18.4	26.9	3.97	3.14E+02	1.07E+03	1.04E-01	2155	3506	3141	3561	3233	3591	3283	3651	3385
M2T	18.4	27.1	1.62	1.29E+02	1.78E+02	1.04E-01	3066	3465	3149	3496	3194	3518	3227	3563	3294
M2T	18.6	27.2	4.54	3.63E+02	1.40E+03	1.03E-01	73	3407	3114	3468	3222	3498	3274	3560	3380
M5T	16.7	28.0	0.98	2.02E+02	1.63E+02	6.32E-02	2731	3237	2708	3319	2814	3376	2895	3494	3062
M5T	16.7	28.1	1.34	2.79E+02	3.07E+02	6.28E-02	2335	3343	2851	3429	2965	3483	3044	3596	3208
M5T	17.0	28.1	1.71	3.54E+02	4.96E+02	6.28E-02	2435	3468	3114	3533	3204	3570	3256	3643	3364
M5T	17.1	28.1	2.38	4.92E+02	9.59E+02	6.30E-02	106	3222	2787	3292	2850	3341	2897	3440	2995
M5T	14.5	28.4	2.45	5.16E+02	1.02E+03	6.20E-02	393	3342	2950	3398	3038	3433	3094	3504	3210
N1T	18.4	26.7	2.39	1.67E+02	1.89E+02	8.25E-02	3338	3575	3312	3621	3365	3655	3408	3725	3495
N1T	18.4	26.7	4.42	3.09E+02	6.49E+02	8.25E-02	2764	3649	3331	3686	3395	3706	3430	3747	3500
N1T	18.5	26.7	5.62	3.93E+02	1.05E+03	8.25E-02	2466	3716	3503	3761	3572	3780	3603	3818	3666
N1T	18.6	26.8	1.63	1.14E+02	8.79E+01	8.22E-02	3135	3530	3182	3586	3267	3622	3328	3695	3452
N1T	18.6	26.9	3.37	2.37E+02	3.77E+02	8.21E-02	2796	3523	3252	3556	3299	3577	3328	3618	3387
N1T	8.4	27.5	1.61	1.16E+02	8.65E+01	8.04E-02	3044	3372	2999	3453	3098	3511	3175	3631	3334
N1T	8.4	27.6	2.42	1.73E+02	1.94E+02	8.02E-02	3095	3602	3152	3640	3222	3667	3273	3721	3379
N1T	8.5	27.6	3.46	2.49E+02	3.98E+02	8.01E-02	2795	3602	3277	3638	3334	3659	3369	3703	3441
N1T	8.8	27.9	4.51	3.27E+02	6.74E+02	7.93E-02	2202	3526	3256	3556	3303	3575	3330	3612	3384

Table III.1.3 (continued)

Case	Water Temp. [°C]	Oil Temp. [°C]	Jet Velocity [m/s]	Re_D	*We*	*Z*	No. of Samples	D_{10} [µm]	D_{10} (PVC) [µm]	D_{20} [µm]	D_{20} (PVC) [µm]	D_{30} [µm]	D_{30} (PVC) [µm]	D_{32} [µm]	D_{32} (PVC) [µm]
N2T	17.5	28.4	1.65	2.43E+02	1.80E+02	5.53E-02	3437	3230	2766	3280	2828	3321	2885	3407	3001
N2T	17.5	28.6	2.14	3.19E+02	3.04E+02	5.47E-02	3144	3450	3192	3507	3262	3548	3315	3631	3423
N2T	17.5	28.7	2.85	4.25E+02	5.37E+02	5.46E-02	2565	3555	3160	3602	3251	3629	3303	3683	3408
N2T	17.5	28.9	3.52	5.27E+02	8.21E+02	5.43E-02	2748	3602	3312	3638	3363	3659	3394	3701	3457
N2T	17.7	29.0	4.01	6.03E+02	1.06E+03	5.40E-02	2795	3585	3385	3608	3411	3623	3428	3650	3463
N2T	17.7	28.9	5.31	7.95E+02	1.86E+03	5.43E-02	974	3653	3477	3676	3518	3688	3536	3711	3574
N2S	18.2	27.0	1.65	2.32E+02	1.81E+02	5.79E-02	3321	3370	3093	3412	3143	3444	3183	3509	3263
N2S	18.3	27.1	2.11	2.98E+02	2.94E+02	5.76E-02	3013	3486	3187	3535	3253	3570	3304	3641	3407
N2S	18.4	27.3	2.76	3.92E+02	5.05E+02	5.73E-02	2772	3427	3033	3465	3087	3493	3129	3551	3214
N2S	18.4	27.4	3.78	5.40E+02	9.47E+02	5.70E-02	1507	3495	3197	3527	3261	3546	3296	3584	3366
P1T	17.7	27.2	4.86	2.98E+01	8.40E+02	9.73E-01	2095	3622	3257	3659	3326	3684	3374	3735	3470
P1T	17.7	27.3	3.73	2.31E+01	4.94E+02	9.63E-01	3078	3593	3281	3637	3353	3666	3400	3724	3497
P1T	17.7	27.5	5.41	3.45E+01	1.04E+03	9.34E-01	2014	3607	3262	3664	3344	3697	3397	3765	3504
P5T	17.9	27.8	1.17	3.92E+01	2.42E+02	3.97E-01	3096	3361	2723	3423	2856	3471	2967	3569	3203
P5T	18.0	28.0	1.72	5.97E+01	5.28E+02	3.85E-01	2843	3537	3139	3574	3199	3600	3242	3652	3330
P5T	18.1	27.9	1.47	5.01E+01	3.83E+02	3.91E-01	2903	3434	3045	3493	3123	3631	3177	3609	3287
S1T	5.3	25.9	1.06	5.50E+01	5.24E+01	1.32E-01	2320	993	569	1124	740	1214	885	1416	1267
S1T	5.4	26.0	2.11	1.10E+02	2.07E+02	1.31E-01	2336	807	450	1009	617	1172	797	1581	1331
S1T	5.4	26.0	4.03	2.10E+02	7.56E+02	1.31E-01	1301	1035	598	1288	906	1442	1127	1807	1742
S1T	5.5	26.1	5.77	3.01E+02	1.55E+03	1.31E-01	400	851	399	1186	720	1380	975	1869	1793
S1T	5.6	26.3	5.71	2.98E+02	1.52E+03	1.31E-01	843	1410	707	1594	912	1702	1111	1940	1650
S1T	19.0	28.0	1.38	7.46E+01	8.85E+01	1.26E-01	2296	967	459	1215	672	1376	888	1766	1554
S1T	19.0	28.0	2.51	1.36E+02	2.93E+02	1.26E-01	1883	1115	501	1363	731	1509	956	1850	1636
S1T	19.0	28.0	3.54	1.91E+02	5.82E+02	1.26E-01	1922	981	503	1214	724	1371	935	1749	1559
S1T	19.0	27.9	4.95	2.67E+02	1.14E+03	1.26E-01	1225	1126	482	1411	802	1560	1051	1906	1806
S2T	7.1	24.8	1.21	1.23E+02	1.36E+02	9.51E-02	793	1550	1472	1616	1538	1659	1582	1748	1673
S2T	7.2	25.4	2.35	2.41E+02	5.14E+02	9.40E-02	4370	996	559	1195	765	1335	955	1668	1489
S2T	7.2	25.4	2.37	2.43E+02	5.23E+02	9.40E-02	3984	1000	559	1200	717	1349	891	1704	1376
S2T	7.3	25.3	3.23	3.31E+02	9.71E+02	9.41E-02	3421	1048	550	1265	769	1408	970	1744	1546
S2T	7.4	25.9	0.66	6.82E+01	4.03E+01	9.30E-02	1007	394	239	551	337	724	474	1249	941
S2T	7.5	25.9	1.58	1.64E+02	2.33E+02	9.30E-02	4922	960	522	1141	718	1269	898	1570	1403
S2T	7.6	26.0	2.76	2.87E+02	7.08E+02	9.28E-02	3096	1037	552	1246	760	1384	852	1710	1493
S2T	7.8	26.1	1.10	1.14E+02	1.12E+02	9.27E-02	2047	347	250	523	294	746	408	1521	788

Table III.1.3 (continued)

Case	Water Temp. [°C]	Oil Temp. [°C]	Jet Velocity [m/s]	Re_D	*We*	*Z*	No. of Samples	D_{10} [µm]	D_{10} (PVC) [µm]	D_{20} [µm]	D_{20} (PVC) [µm]	D_{30} [µm]	D_{30} (PVC) [µm]	D_{32} [µm]	D_{32} (PVC) [µm]
S2T	20.3	25.9	1.31	1.36E+02	1.61E+02	9.29E-02	1462	1172	845	1300	964	1387	1052	1578	1253
S2T	20.3	26.0	2.39	2.48E+02	5.30E+02	9.28E-02	1517	1074	593	1266	770	1395	944	1695	1417
S2T	20.3	26.0	2.55	2.65E+02	6.03E+02	9.28E-02	1333	908	484	1123	650	1279	831	1656	1357
S2T	20.3	26.2	3.28	3.42E+02	1.00E+03	9.25E-02	522	821	369	1154	622	1360	874	1889	1725
S5T	19.1	27.7	1.28	3.44E+02	3.81E+02	5.68E-02	1528	1029	512	1238	751	1368	952	1671	1528
S5T	19.1	27.8	1.04	2.79E+02	2.49E+02	5.66E-02	2040	1244	652	1400	894	1495	1082	1706	1584
S5T	19.1	27.5	0.87	2.34E+02	1.78E+02	5.70E-02	2223	1220	702	1374	881	1479	1043	1715	1463
S5T	19.2	27.6	1.89	5.08E+02	8.33E+02	5.69E-02	1214	962	535	1225	845	1381	1066	1754	1695
S5T	19.3	27.5	2.56	6.87E+02	1.53E+03	5.69E-02	1049	804	428	1123	751	1313	993	1794	1738

Explanation of Case code:

G2T: Genesis; 2 mm orifice diameter; tap water
G5T: Genesis; 5 mm orifice diameter; tap water
M2T: Mars TLP; 2 mm orifice diameter; tap water
M5T: Mars TLP; 5 mm orifice diameter; tap water
N1T: Neptune SPAR; 1 mm orifice diameter; tap water
N2T: Neptune SPAR; 2 mm orifice diameter; tap water
N2S: Neptune SPAR; 2 mm orifice diameter; sea water
P1T: Platform Gail; 1 mm orifice diameter; tap water
P5T: Platform Gail; 5 mm orifice diameter; tap water
S1T: Silicone fluid SF96-20; 1 mm orifice diameter; tap water
S2T: Silicone fluid SF96-20; 2 mm orifice diameter; tap water
S5T: Silicone fluid SF96-20; 5 mm orifice diameter; tap water

also provides values of the characteristic diameters corrected using a standard algorithm provided by the manufacturer to compensate for measurement errors arising from non-uniformities in light intensity over the optical sample volume due to the Gaussian profile of the laser beams. This problem was discussed in SectionII.1.1.2.2. The corrected diameters are identified by the abbreviation "PVC" (Probe Volume Correction). The algorithm employs weighting factors, c_i, that depend on the measured diameter, in the following relationships:

Probe Volume Corrected (PVC) Arithmetic Mean Diameter, D_{10}

$$D_{10}(PVC) \equiv \frac{\sum_{i=1}^{n} c_i d_i}{\sum_{i=1}^{n} c_i} \tag{III.1.4}$$

Probe Volume Corrected (PVC) Area Mean Diameter, D_{20}

$$D_{20}(PVC) \equiv \sqrt{\frac{\sum_{i=1}^{n} c_i d_i^2}{\sum_{i=1}^{n} c_i}} \tag{III.1.5}$$

Probe Volume Corrected (PVC) Volume Mean Diameter, D_{30}

$$D_{30}(PVC) \equiv \sqrt[3]{\frac{\sum_{i=1}^{n} c_i d_i^3}{\sum_{i=1}^{n} c_i}} \tag{III.1.6}$$

Probe Volume Corrected (PVC) Sauter Mean Diameter, D_{32}

$$D_{32}(PVC) \equiv \frac{\sum_{i=1}^{n} c_i d_i^3}{\sum_{i=1}^{n} c_i d_i^2} \tag{III.1.7}$$

In general, Probe Volume Corrected diameters are smaller than the uncorrected values since they tend to weight the statistics in favor of smaller particles that are not detected well by the PDPA.

Although examination of the measured values of D_{10}, D_{20}, D_{30}, and D_{32}.would suggest that large droplets continue to be produced and dominate the size statistics even at relatively high flow rates where the jet appears to be atomized, a comparison to the size histograms and the close-up video records reveal significant discrepancies. The PDPA seems to be unable to adequately detect oil droplets under about 2 mm in diameter.

Figures III.1.6 and III.1.7 present, respectively the size histogram measured by the PDPA and corresponding video images of the flow. These data are for the case of Neptune SPAR oil injected into 17.5°C tap water at a velocity of 2.1 m/s through a 2 mm diameter orifice. A far-field view of the jet is included in Figure III.1.7. The histogram implies that there are very few droplets smaller than approximately 3 mm. The representative close-up video image provided in Figure II.1.7, along with an image of a millimeter scale recorded before oil was injected (note

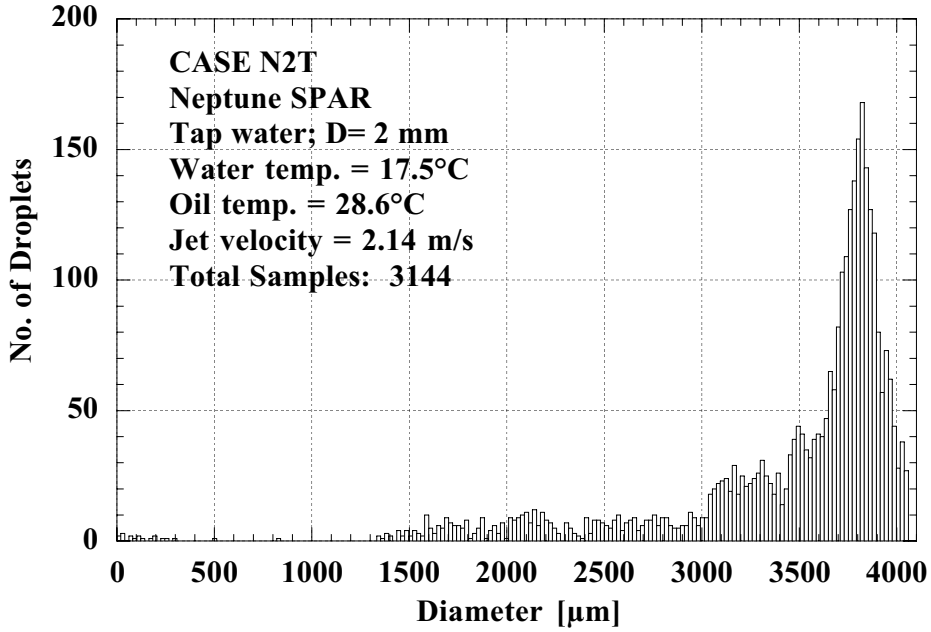

Figure III.1.6 Oil droplet size histogram measured with the PDPA. Flow conditions are given in the figure.

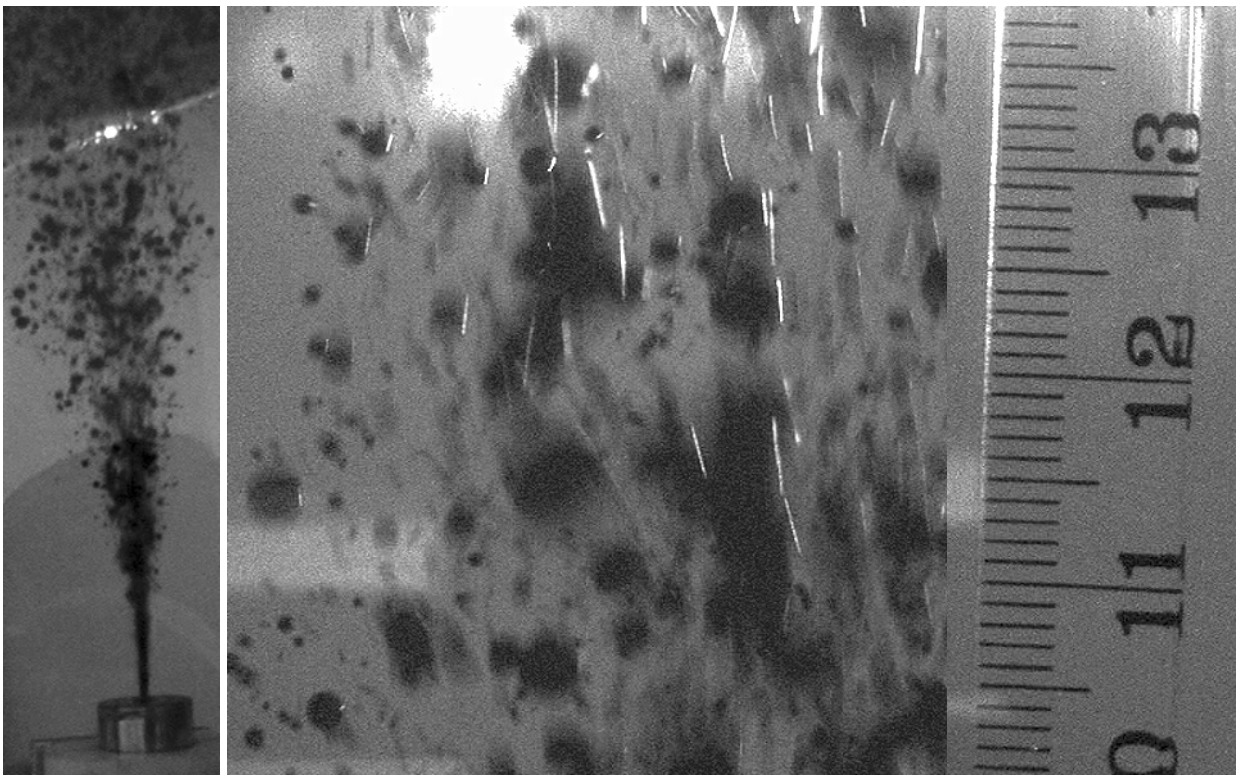

Figure III.1.7 Video images of the jet corresponding to the PDPA size histogram shown in Figure III.1.6. Magnification of the video camera was fixed after the scale was recorded prior to the start of oil injection.

that the magnification of the video camera was fixed) contradict this result. The video indicates that while large droplets persist at this flow rate, there are an equal or larger number of small droplets that apparently are not detected by the PDPA. Further evidence of this problem is provided in Figures III.8 and III.9 which were taken at higher jet velocities (apparent atomization) and correspond to the case of Neptune SPAR oil injected into 18.4°C natural sea water at a velocity of 3.8 m/s through the same 2 mm diameter orifice. Although the density of the oil plume makes it difficult to distinguish individual droplets, images of the perimeter of the plume (where the PDPA measurements were performed) give an indication of the representative droplet sizes. The contradiction between the video data and the PDPA measurements is even more pronounced.

Figure III.1.10 presents six droplet size histograms obtained in sequence with the PDPA during an experiment in which Neptune SPAR oil was injected into tap water at a nominal temperature of 17.5°C through the 2 mm orifice. Jet velocities ranged from 1.6 m/s to 5.3 m/s. Contrary to intuition and evidence provided in the video records, there is no indication of any increase in the number of smaller droplets as the jet proceeds from Type II instability to full atomization. Based on a comprehensive review of all the PDPA oil data, it is concluded that the instrument is extremely biased toward large droplets and is not capable of providing accurate size statistics for polydispersed opaque fluids such as crude oil. The source of the problem probably is related to beam attenuation upstream of the optical sample volume, and multiple scattering of the reflected signals, by the optically thick oil droplet cloud. This has been discussed in Section II.1.1.2.2. The results of verification tests that were conducted recently at UH and are reported in Appendix D confirm that the PDPA is capable of performing reflective measurements of small droplets when number densities are low. Although attempts have been made to post-process the data sets to compensate for the instrument bias, there is no clear evidence that these adjusted statistics accurately represent the actual droplet ensemble; hence, these results are not reported.

In contrast to the PDPA oil results, data obtained in the clear silicone fluid injection experiments appear to correlate well with the video records and provide quantitative insight into the breakup processes occurring at the transition to full atomization. The primary shortcoming of these PDPA measurements is that the upper size limit of the instrument when it is operated in this configuration is about 2100 μm (2.1 mm). Droplets larger than this limit cannot be detected.

Figures III.1.11 and III.1.12 present PDPA size histograms for silicone fluid injected into tap water at nominal temperatures of 20.3°C and 7.5°C, respectively, through the 2mm diameter orifice at different velocities. The histograms reveal a multi-modal size distribution and a steady increase in the fraction of fine droplets under 500 μm with increasing velocity. The multi-modal distribution (i.e., more than one size peak) may reflect the two breakup mechanisms that were observed to operate in parallel from the onset of what we denote as the Type II instability. Small droplets are generated from the jet surface and larger drops form as a result of the breakup of the jet core filament.

Since the results of this study were intended to be applied to actual oil spill events, it was of interest to elucidate scaling laws. Of particular interest was the dependence of droplet size on the scale of the orifice through which the oil escapes into the water. Given the limitations of the experimental system, the range of orifice diameters that could be tested was limited. The

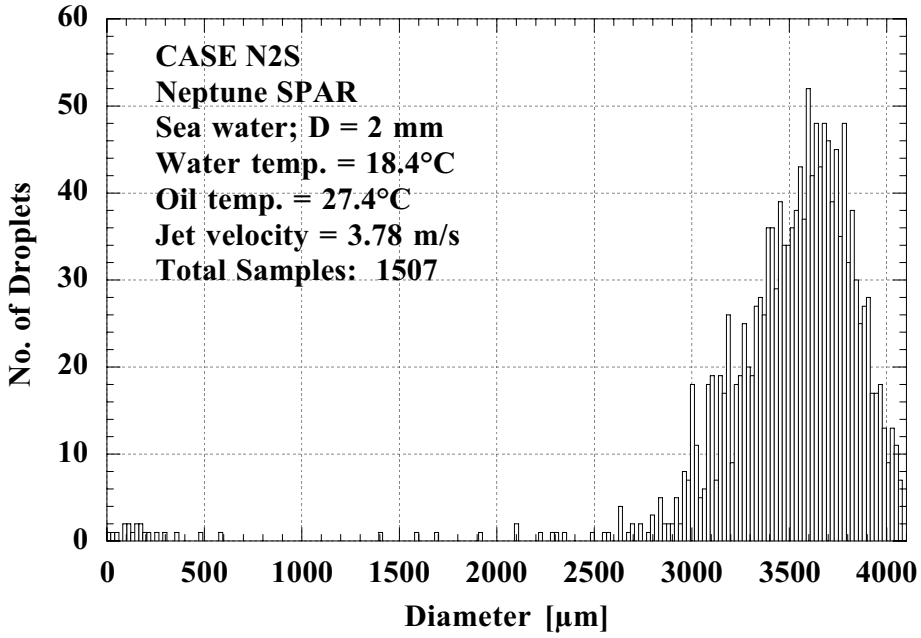

Figure III.1.8 Oil droplet size histogram measured with the PDPA. Flow conditions are given in the figure.

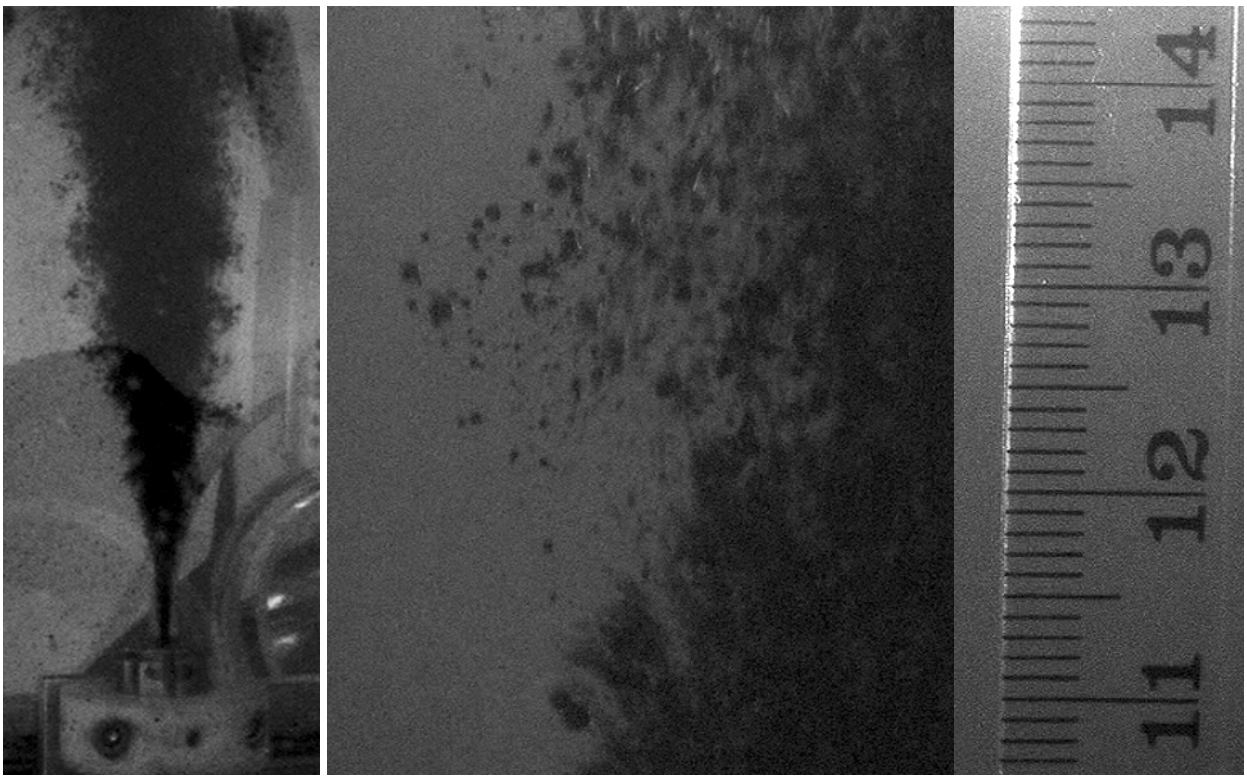

Figure III.1.9 Video images of the jet corresponding to the PDPA size histogram shown in Figure III.1.8. Magnification of the video camera was fixed after the scale was recorded prior to the start of oil injection.

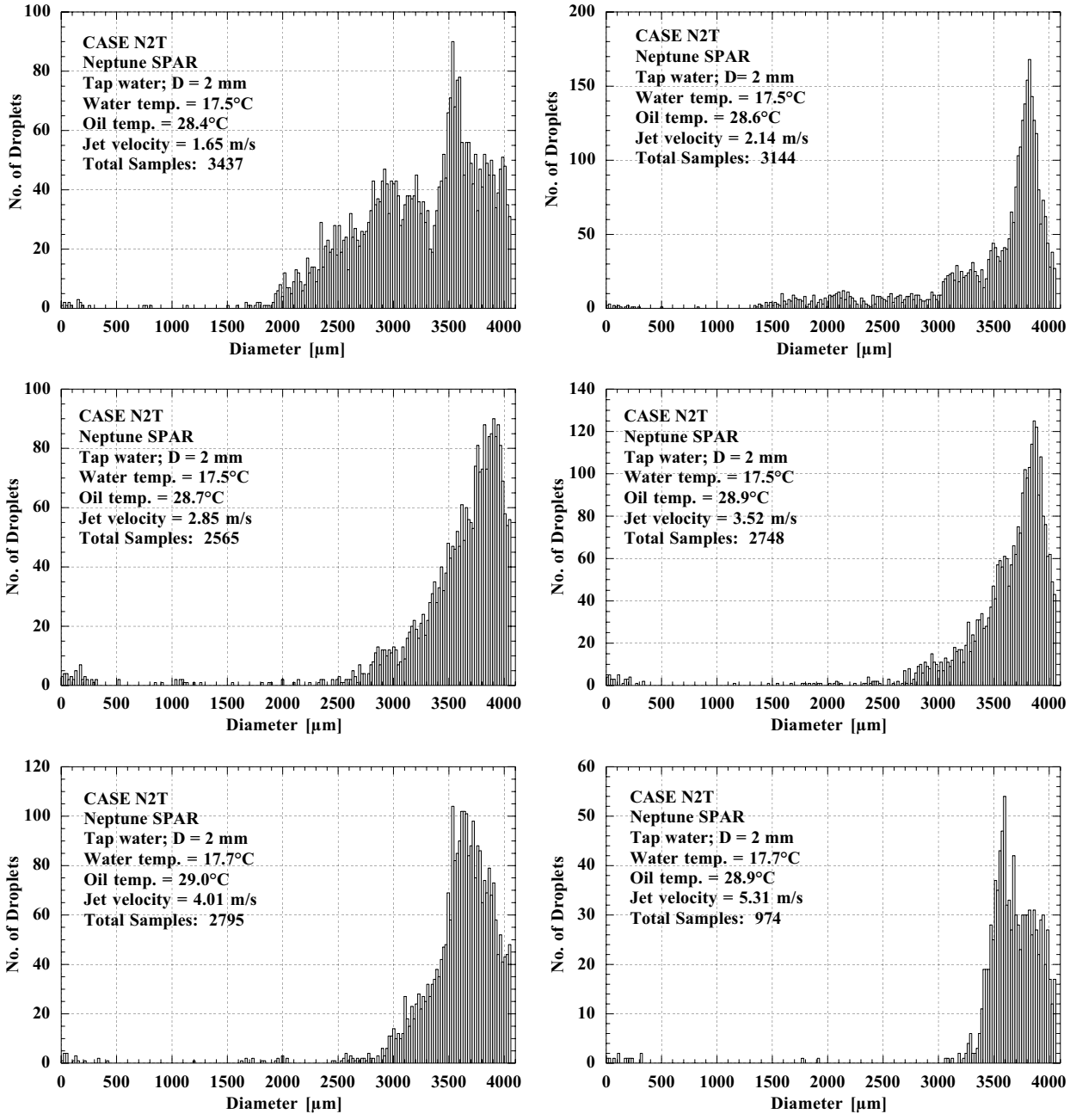

Figure III.1.10 Droplet size histograms measured at different jet velocities with the PDPA for Neptune SPAR crude oil discharging through a 2 mm diameter orifice into nominal 17.5°C tap water. Flow conditions are given in the figures.

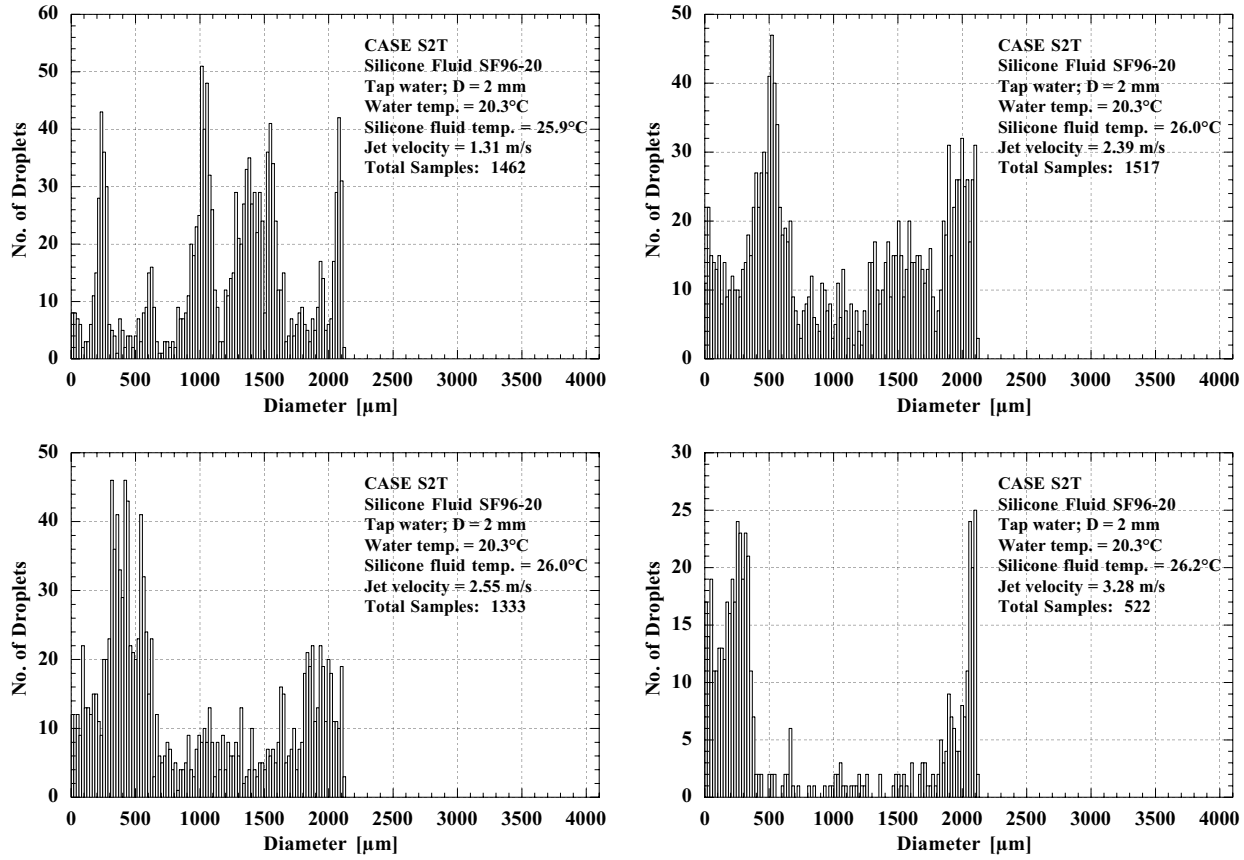

Figure III.1.11 Droplet size histograms measured at different jet velocities with the PDPA for pure silicone fluid SF96-20 discharging through a 2 mm diameter orifice into nominal 20.3°C tap water. Flow conditions are given in the figures.

minimum orifice diameter was 1 mm and the largest measured 5 mm. Theoretical relationships for droplet diameters have been verified in the Rayleigh instability regime (Teng *et al.*, 1995). Until this study, very limited size information was available in the literature for transitional and atomized liquid-liquid systems.

Figures III.1.13 and II.1.14 present PDPA size histograms obtained at different velocities for silicone fluid injected into tap water through a 1 mm and 5 mm diameter orifice, respectively. Although the information on large droplets is incomplete (due to dynamic range limitations of the instrument) comparison of these histograms and the data given in Figures III.1.12 and II.1.13 for the 2 mm diameter orifice does not reveal any conclusive differences in the distribution of droplet sizes. For all three orifices, a peak appears between 300 µm and 600 µm. As jet velocity is increased, the number of droplets smaller than 300 µm rises and intermediate peaks seem to disappear resulting in a bimodal distribution comprising very large and very fine droplets. The histograms reveal no clear relationship between orifice diameter and the size of the fine droplets.

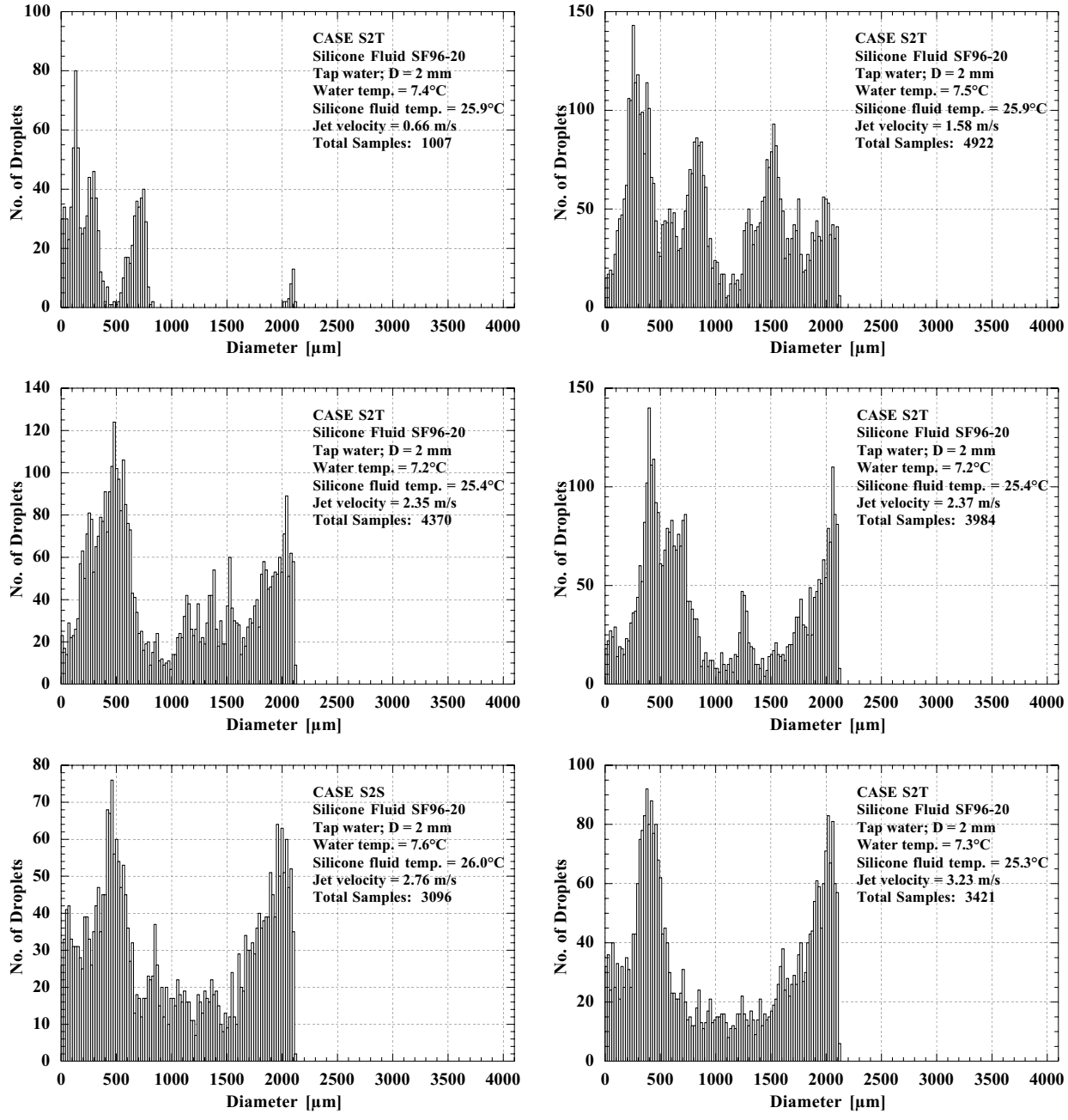

Figure III.1.12 Droplet size histograms measured at different jet velocities with the PDPA for pure silicone fluid SF96-20 discharging through a 2 mm diameter orifice into nominal 7.5°C tap water. Flow conditions are given in the figures.

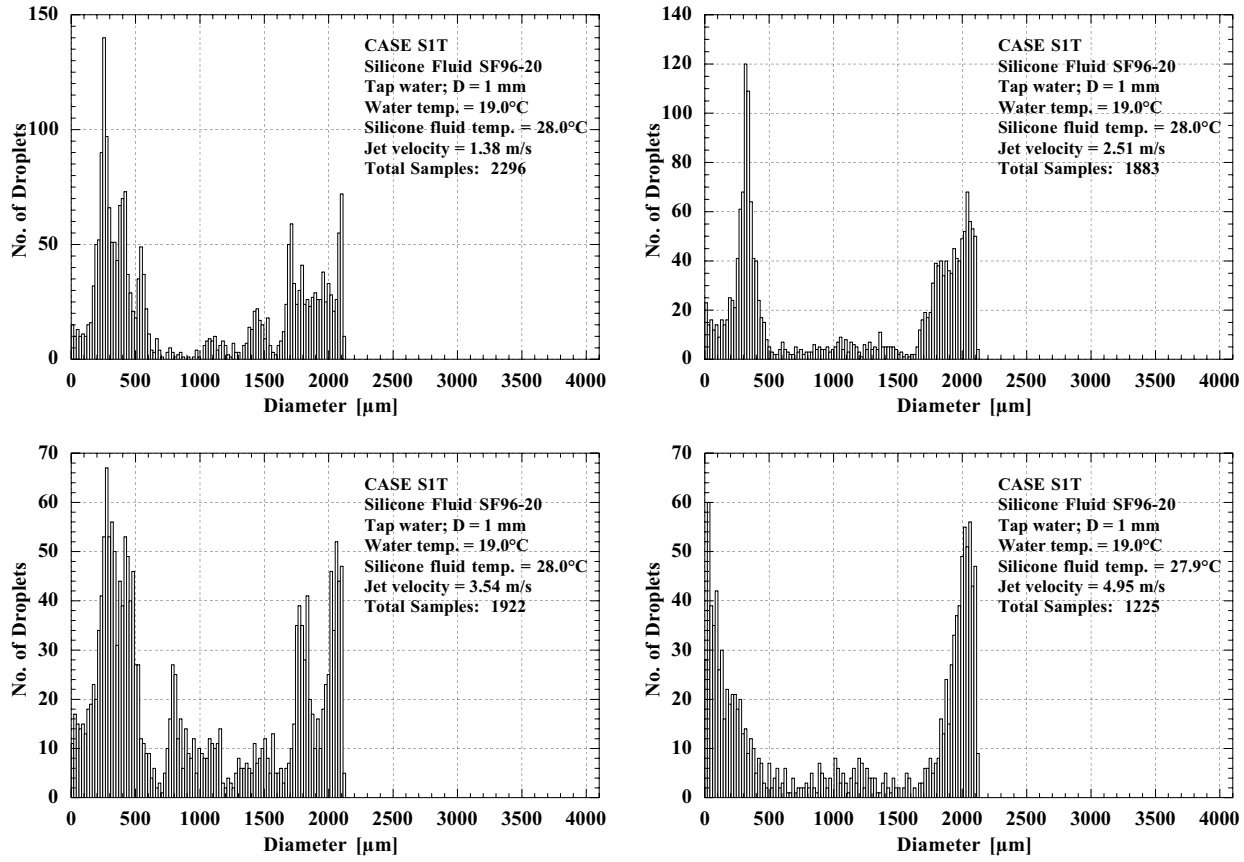

Figure III.1.13 Droplet size histograms measured at different jet velocities with the PDPA for pure silicone fluid SF96-20 discharging through a 1mm diameter orifice into nominal 19°C tap water. Flow conditions are given in the figures.

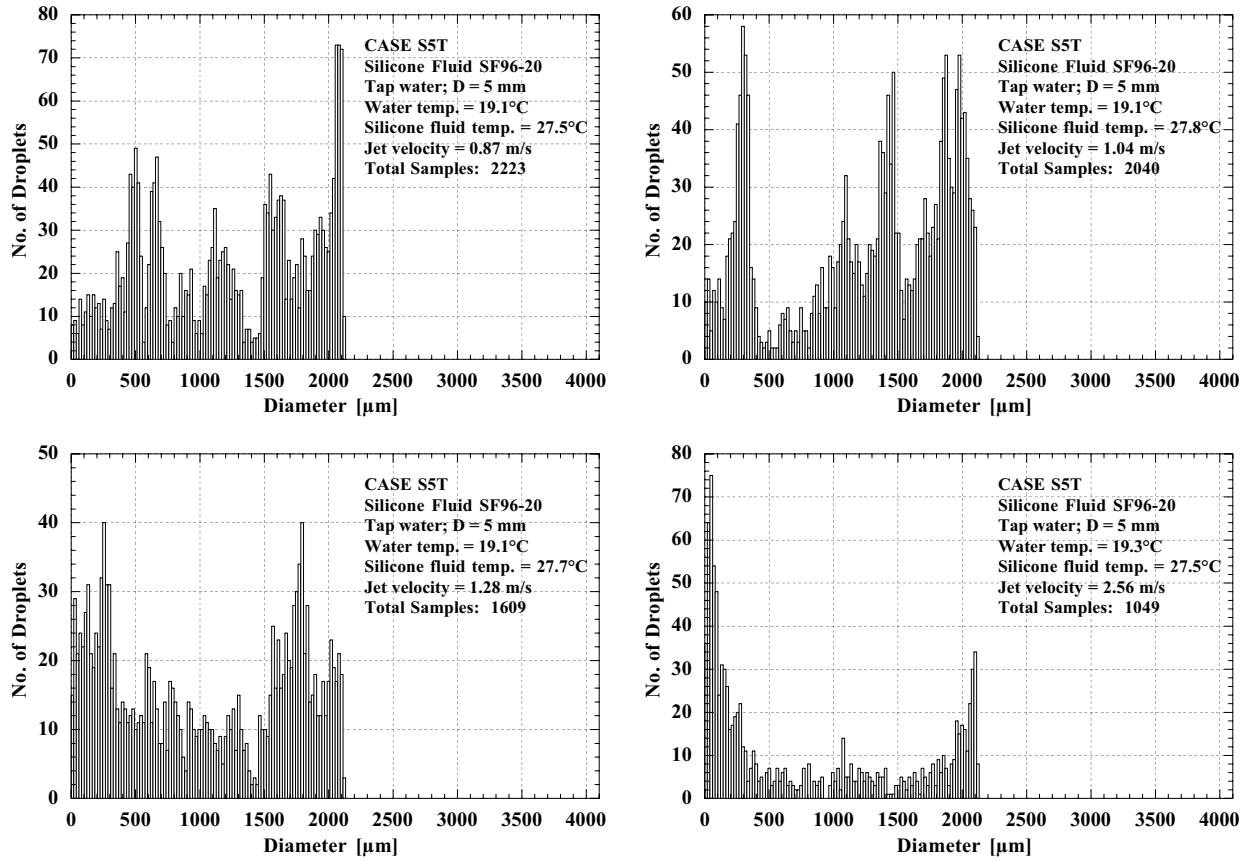

Figure III.1.14 Droplet size histograms measured at different jet velocities with the PDPA for pure silicone fluid SF96-20 discharging through a 5 mm diameter orifice into nominal 19°C tap water. Flow conditions are given in the figures.

Although the apparent independence of small droplet size and discharge orifice diameter needs to be confirmed through experiments conducted at a larger scale, one explanation may be that since small droplets appear to be produced at the surface of the jet, the generation mechanism becomes relatively scale independent once a threshold radius of curvature is exceeded. Since atomization serves to redistribute the jet fluid into small droplets, this implies that at a given value of jet velocity, the droplet production rate must increase approximately as the square of the discharge orifice diameter, D^2, to compensate for the additional mass flow. If, instead, small droplet size actually scales as D^n, then the droplet production rate will vary as $D^{2/(3n)}$.

To conclude the discussion of the results of the oil breakup experiments, it should be noted that there was no evidence of emulsion formation for any of the oils due to shear flow mixing of the ambient water and the jet fluid. Bluff bodies placed in the jet had no effect; however, the maximum velocities examined in this study were relatively low (< 6 m/s).

III.1.2 Gas Hydrate Formation

Excluding tests that were terminated as a result of equipment failure or the inability to obtain video data due to turbidity of the synthetic sea water, a total of about 20 cases were examined in the exploratory experiments conducted at UH to investigate hydrate formation. Table III.1.4 summarizes the test cases.

Table III.1.4 Test cases examined in gas hydrate formation experiments.

Case	Gas	Oil	Water	Range of pressure readings [psig]	Range of pressure readings [MPa]	Water temp. exiting pressure vessel [°C]	Water temp. entering pressure vessel [°C]
H1	NG1	none	tap water	850	5.96	not available	8.42-9.38
H2	NG1	none	tap water	850	5.96	not available	9.40-9.68
H3	NG1	none	tap water	850	5.96	not available	9.68-10.01
H4	NG1	none	tap water	863-871	6.05-6.11	not available	0-2.74
H5	NG1	none	sea water	874-875	6.127-6.134	4.69-4.78	1.54-1.97
H6	NG2	none	tap water	871-872	6.107-6.114	not available	2.55-2.88
H7	NG2	none	sea water	875-876	6.134-6.141	4.48-4.90	1.03-1.82
H8	NG2	none	tap water	872-877	6.11-6.15	3.34-3.69	1.08-1.36
H9	NG2	none	tap water	873-874	6.120-6.127	3.32-3.42	0.96-1.19
H10	NG3	none	tap water	853-865	5.98-6.07	not available	2.33-2.95
H11	NG3	none	sea water	876	6.14	4.18-4.21	0.67-0.72
H12	NG3	none	tap water	295-301	2.14-2.18	4.34-4.61	1.87-2.09
H13	NG3	none	tap water	605-609	4.27-4.30	3.72-4.44	1.61-2.08
H14	NG3	none	tap water	875-877	6.13-6.15	3.75-3.92	1.37-1.74
H15	NG3	none	tap water	874-875	6.127-6.134	3.31-3.46	0.67-0.91
H16	NG3	none	tap water	632-782	4.46-5.49	3.65-3.82	1.60-1.79
H17	NG3	none	sea water	876-200	6.14-1.48	3.92-4.18	0.31-0.67
H18	NG3	NS	tap water	866-867	6.072-6.079	4.21-4.30	1.97-2.02
H19	NG3	PG	tap water	874-878	6.13-6.16	3.26-4.21	0.65-1.44
H20	NG3	PG	tap water	796-265	5.59-1.93	4.19-4.44	1.06-1.24

Explanation of Gas and Oil codes:

NG1: 100% CH_4
NG2: 90% CH_4 + 10% C_2H_6
NG3: 70% CH_4 + 20% C_2H_6 + 10% C_3H_8
NS: Neptune SPAR
PG: Platform Gail

As described in Sections II.1.2.1.1 and II.1.2.3, the temperature of the water in the clear test section of the water tunnel was not measured directly. The two temperatures provided in Table II.1.4 correspond to points in the external water circulation lines (see Figure II.1.17). The temperature of water exiting the pressure vessel is representative of the temperature of the water surrounding the water tunnel. Water entering the pressure vessel after passing through the chiller

is expected to warm slightly (< 1°C) due to heat transfer before it enters the test section. With the exception of Cases H1, H2, and H3 which were conducted before the manually-agitated chiller was installed, the majority of tests were performed at 2-3°C and 6.1 MPa. These conditions fall well within the hydrate phase boundaries for methane, ethane, and propane.

As observed by Bishnoi (1999) and other researchers, hydrate formation in water that is not saturated with the guest hydrocarbon species generally proceeds slowly. The induction time for nucleation and the rate of crystal growth may be very long for the case of hydrate formation on natural gas bubbles rising through the water column, where the gas-rich diffusion layer around a bubble may be constantly swept away by the relative motion of the bubble and water phases. In consideration of this, the first objective of the experiments was to determine if hydrates would form on the gas bubbles stabilized by the downward flow of water in the water tunnel.

Hydrate formation was visually confirmed on moving bubbles of all three gas mixtures, NG1, NG2, and NG3. Figure III.1.15 shows video frames from Test Case H14. It was observed that:

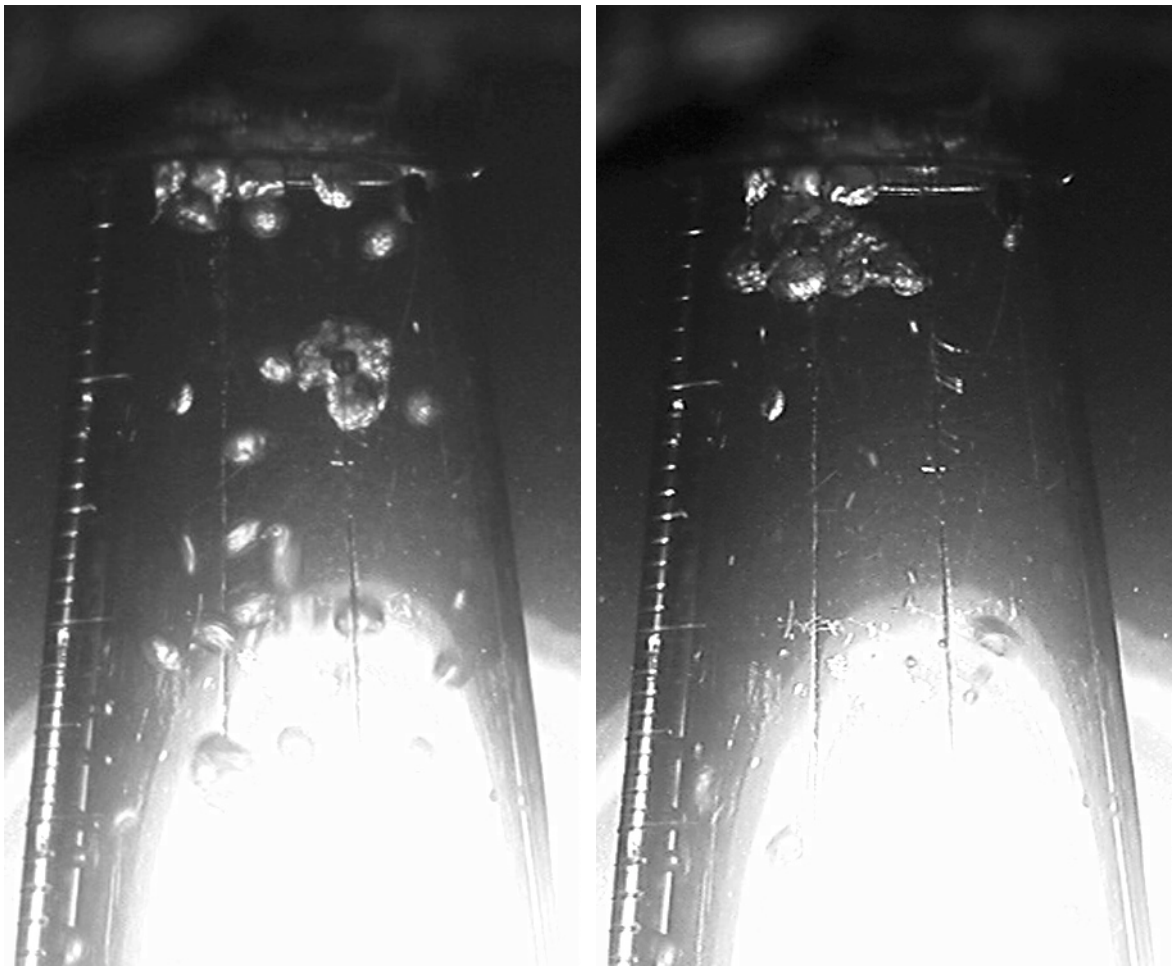

Figure III.1.15 Hydrate formation on rising bubbles of gas mixture NG3. Nominal 2°C tap water flows downward over the bubbles. Pressure is approximately 6.13 MPa. The diameter at the top of conical observation section is approximately 2.5 cm.

1. a finite induction period of the order of minutes or longer was required before hydrates could be detected with the close-up video camera (hydrates were identified by the striated surfaces or irregularly and sharp deformed shapes of the bubbles). Once nucleation and initial crystal formation occurred, the hydrate film rapidly enveloped the bubble surface.

2. As anticipated, hydrates formed most readily on bubbles of NG3 gas. The NG3 gas mixture contained 20% C_2H_6 and 10% C_3H_8, which form hydrates at significantly higher temperatures than CH_4 at the same partial pressure.

3. Small bubbles ($\leq$ 1-2 mm in diameter) which were well dispersed did not appear to form hydrates. Hydrate formation was generally achieved by producing large gas bubbles.

4. Hydrate formation appeared to be enhanced by high concentrations of moderate size or large bubbles. This may be related to the elevated concentrations of dissolved gas in the wake of a dense bubble ensemble.

5. Saturation, or near saturation of the water in the tank clearly promoted hydrate formation.

6. When a large bubble cap existed by coalescence of a number of bubbles, hydrate formation frequently began in the wake of the cap, either on its trailing surface or on separate bubbles positioned in its wake. The hydrate structure subsequently grew by agglomeration.

7. The thickness of the hydrate film at the gas-water interface was difficult to determine. Since the hydrates that were detected appeared to be quite buoyant, it is presumed that the film does not penetrate deeply into the gas and is self-limited (since gas must either diffuse out or water in through the solid hydrate layer for it to grow).

8. Hydrate shedding could not be detected from individual bubbles but was observed when large agglomerated structures formed.

Applying Henry's Law, it was determined that about 1.1 kg of methane must be dissolved in the 490 liters of water in the pressure vessel to saturate the solution. This corresponds to about 22 cm^3 of gas at the temperature and pressure in the vessel or about 25 cm^3 at room temperature (27°C). The capacity of the manual pressure generator used to feed the gas mixtures into the water tunnel was 20 cm^3/stroke. In some tests, the full capacity of the generator was discharged into the water tunnel (in several steps). While it is unlikely that the water reached saturation, levels of dissolved methane, ethane, and propane could be very high.

The NG3 gas mixture was observed readily to form hydrates. At room temperature, the saturation pressure of propane is about 0.99 MPa, which is greater than the partial pressure of this species in NG3 at a mixture pressure of 6.1 MPa. Once the gas is injected into the 2-3°C water in the pressure vessel, however, its temperature rapidly cools and about 30% of the propane will condense. This liquid phase may enhance the hydrate formation process.

Once it had been confirmed that hydrates would form in flowing tap water in the water tunnel, experiments were performed to determine if substituting sea water would have any significant effect. Synthetic sea water was employed in place of natural sea water since it could be chilled rapidly using ice (prior to adding the salts). Typically, about 6-8 hours are required to cool 570 liters of natural sea water to 0°C using the laboratory's single pass heat exchanger.

Hydrate formation was observed to occur rapidly (provided that the gas bubble loading was high) in tests H5, H7, and H11. In test H11, in which NG3 gas was injected, a large hydrate mass formed near the top of the conical test section, nearly blocking the tunnel until it was blown apart by increasing the water flow rate. The hydrate did not disappear as the facility was depressurized (at an average rate of 0.23 MPa/minute) until pressure reached about 1.4 MPa. Figure III.1.16 shows the hydrate mass as it is collapsing and a view of hydrate particles in the lower portion of the water tunnel test section. Although the turbidity of the synthetic sea water degrades the video image quality, small hydrate fragments that have been dislodged from the mass are clearly visible. Note that the scale of the two images are different. The top of the test section on the image on the left is about 2.5 cm in diameter. Adjacent lines between the (upside down) 80 and 100 markings are spaced about 2 mm apart.

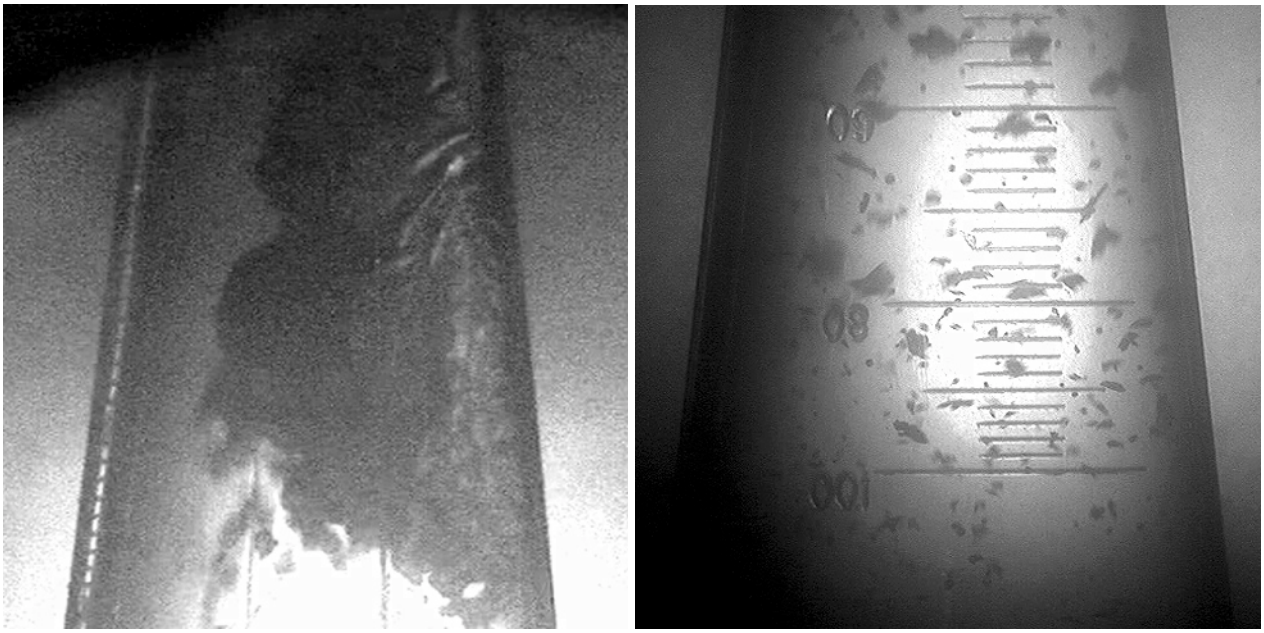

Figure III.1.16 Case H11: hydrate formation in synthetic sea water on rising bubbles of NG3 gas mixture. Sea water flows downward over the bubbles. Pressure is approximately 6.14 MPa. Image on the left shows hydrate mass deposited on wall; figure on the right shows hydrate particles dislodged from the mass in the lower section of the water tunnel.

Additional insight into the hydrate formation process on rising natural gas bubbles is provided by Figure III.1.17 which shows a sequence of video images taken over a period of 37 seconds. No hydrates are detectable in the first image (a.). Image (b.) was taken 6 seconds after image (a.), during which time a hydrate film has formed over the bottom surface of the largest bubble and smaller bubbles have become attached to the film. By the time image (c.) was taken 31 seconds after (b.) the agglomerated hydrate mass has grown substantially.

(a.) No hydrates **(b.) Hydrate formation** **(c.) Growth by agglomeration**

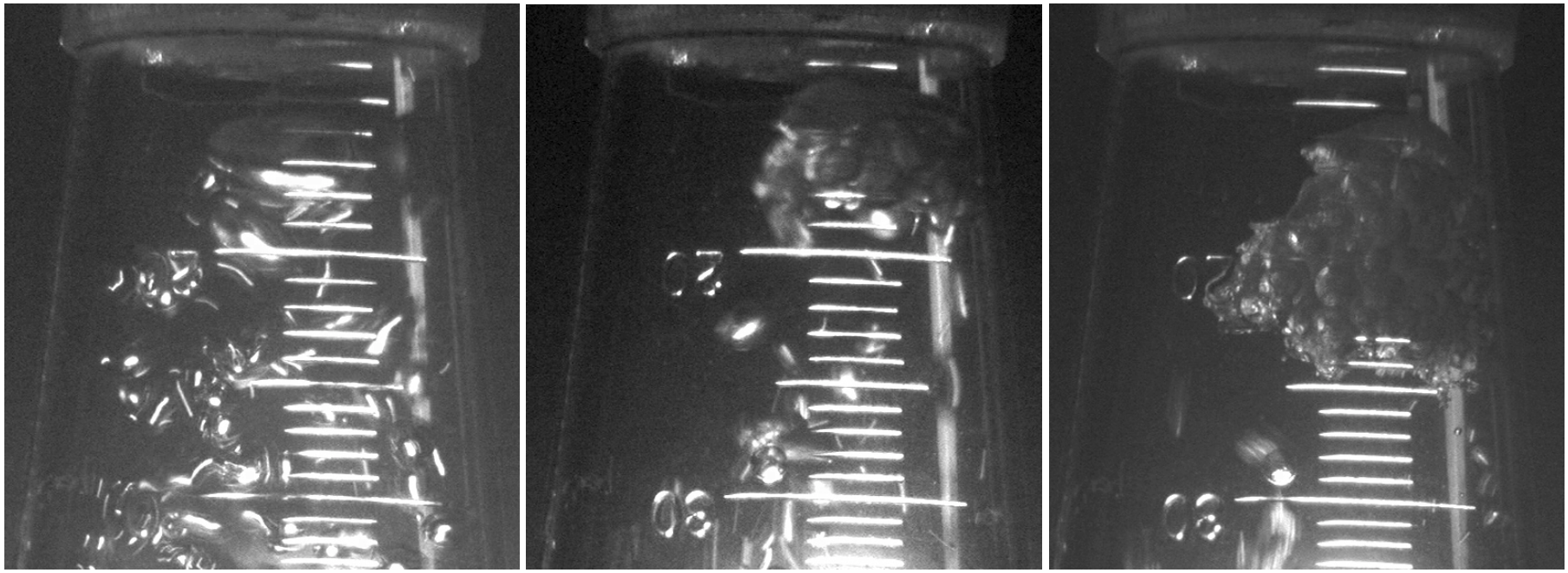

Figure III.1.17 Sequence of video images showing the speed at which hydrate formation proceeds in the flowing water tunnel once nucleation and initial crystal growth has occurred. Images correspond to Case H18; pressure was 6.1 MPa; tap water temperature was approximately 3°C. Images (b.) and (c.) were recorded 6 seconds and 31 seconds after image (a.), respectively. Spacing between the (upside down) 20 and 30 markings is 1.6 cm.

Shortly after the images presented in Figure III.1.17 were recorded, the first oily bubble tests (H18) were conducted. The oil reservoir was filled with Neptune SPAR crude oil. It was visually confirmed that oily bubbles were being injected into the water tunnel before the injector plugged with hydrates. After clearing the blockage with a burst of high pressure gas, hydrates were observed to form immediately on the surface of oily bubbles as they slowly emerged from the injector. Figures III.1.18 and III.1.19 show the progressive growth of hydrate films on two different oily bubbles. The film initiates on hydrate fragments attached to the end of the injector and moves upward over the emerging bubbles. As the hydrate skin advances, it appears to displace the oil film rather than cover it. The oil eventually collects on the top of the bubble like a cap and prevents the hydrate layer from completely encasing the bubble.

The inhibiting effect of the oil film can be better detected in video frames that have been magnified and inverted (i.e., black becomes white like a photograph negative). Figure III.1.20 provides four of these inverted images that show the hydrate film ending at the edge of the oil cap. In the upper images, the top of the hydrate shell has assumed a tulip-like shape, apparently attempting to grow over the oil. The hydrate shell never succeeded in encasing the oil in any of the recordings before the bubble dislodged from the injector. The bubbles could not be tracked after entering the water tunnel.

To confirm the inhibiting effect of oil films on hydrate formation, another oily bubble test was subsequently performed using Platform Gail oil. In tests H19 and H20, no hydrate formation was detected at the injector nor in the water tunnel under conditions that had previously produced hydrates (i.e., NG3 gas mixture; pressures up to 6.16 MPa; estimated tap water temperature in the test section of 2-3°C). After the test section was loaded with gas, a large bubble formed at the exit of contraction by coalescence and attached itself to the walls of the water tunnel. Water continued to flow over the bubble while it was monitored for over 20 minutes. Figure III.1.21 presents two right angle views of the gas bubble. The upper surface of the bubble is inclined at an angle of about 45° to the approach flow. The dark area contacting the bottom surface of the bubble is a layer of crude oil.

Although it cannot be confirmed that, given sufficient time, hydrates would not eventually appear and grow on the bubble surface, the results of these exploratory experiments suggest that the presence of an oil film on the gas-water interface exercises an inhibiting effect on hydrate nucleation and/or crystal growth. Whereas hydrates tended to form readily in the water tunnel on the downstream surfaces of clean gas bubbles, this process seemed to be disrupted by the layer of Platform Gail crude oil. Although the upper surface of the bubble appeared to be free of oil, hydrate nuclei are likely to be swept away from this area by the constant flow of water. It should be noted that Platform Gail was significantly more viscous and tarry than Neptune SPAR and the other two crude oils. It is unknown whether the permeability of the different oils to hydrate forming gases or water vary significantly. It is reasonable to expect that this property will impact hydrate formation on the interfacial oil film.

Additional experiments are warranted to confirm the effects of oil at the gas-water interface. Studies conducted in a static reactor should be fairly easy to design; would eliminate the complications associated with fluid motion; and would provide opportunities to control and measure certain parameters such as oil film thickness.

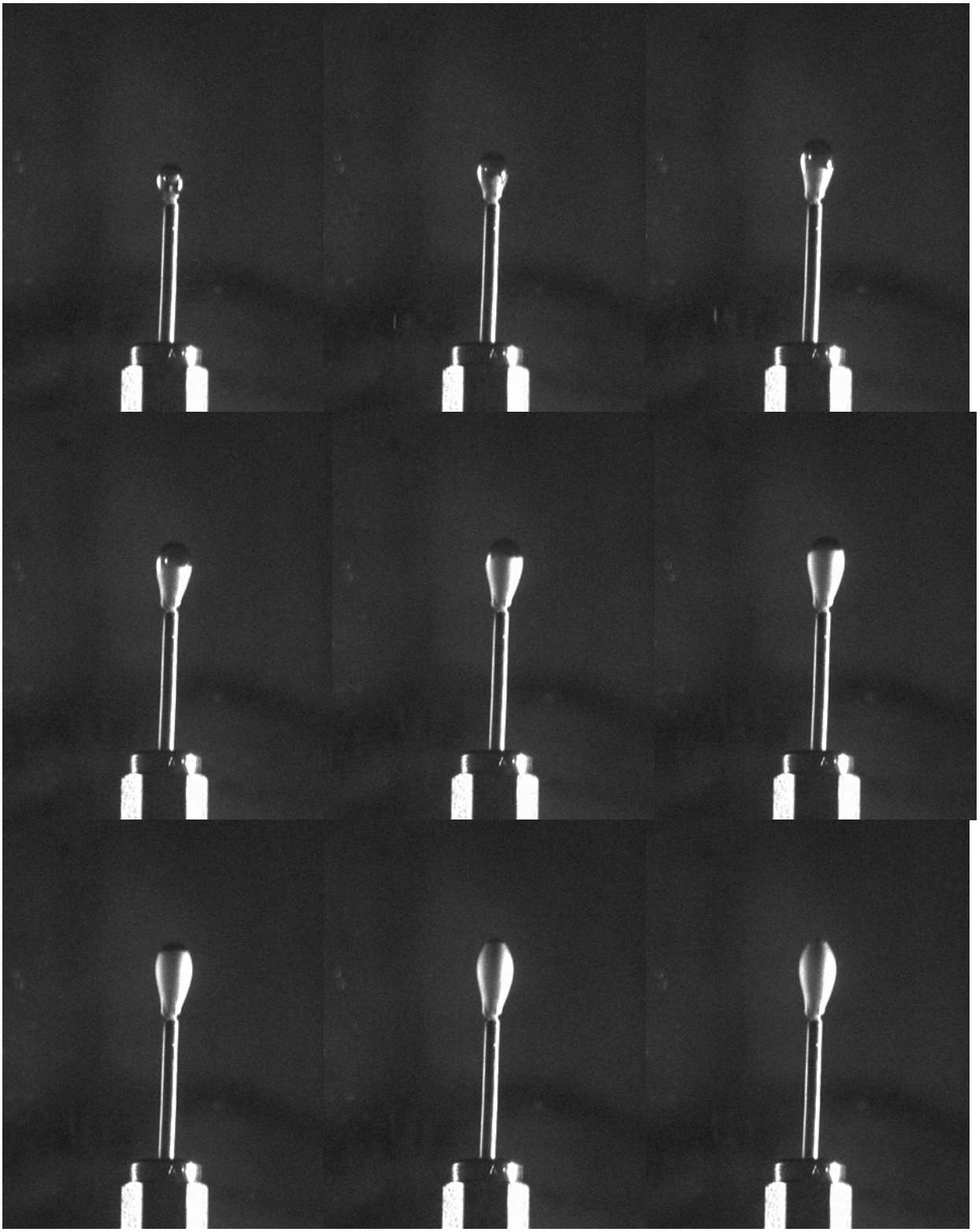

Figure III.1.18 Sequence of video images showing a hydrate film growing on the surface of an oily bubble emerging from the injector. Case H18; Neptune SPAR oil on NG3 gas. Images were recorded 1 second apart. The o.d. of the injector is 1.6 mm.

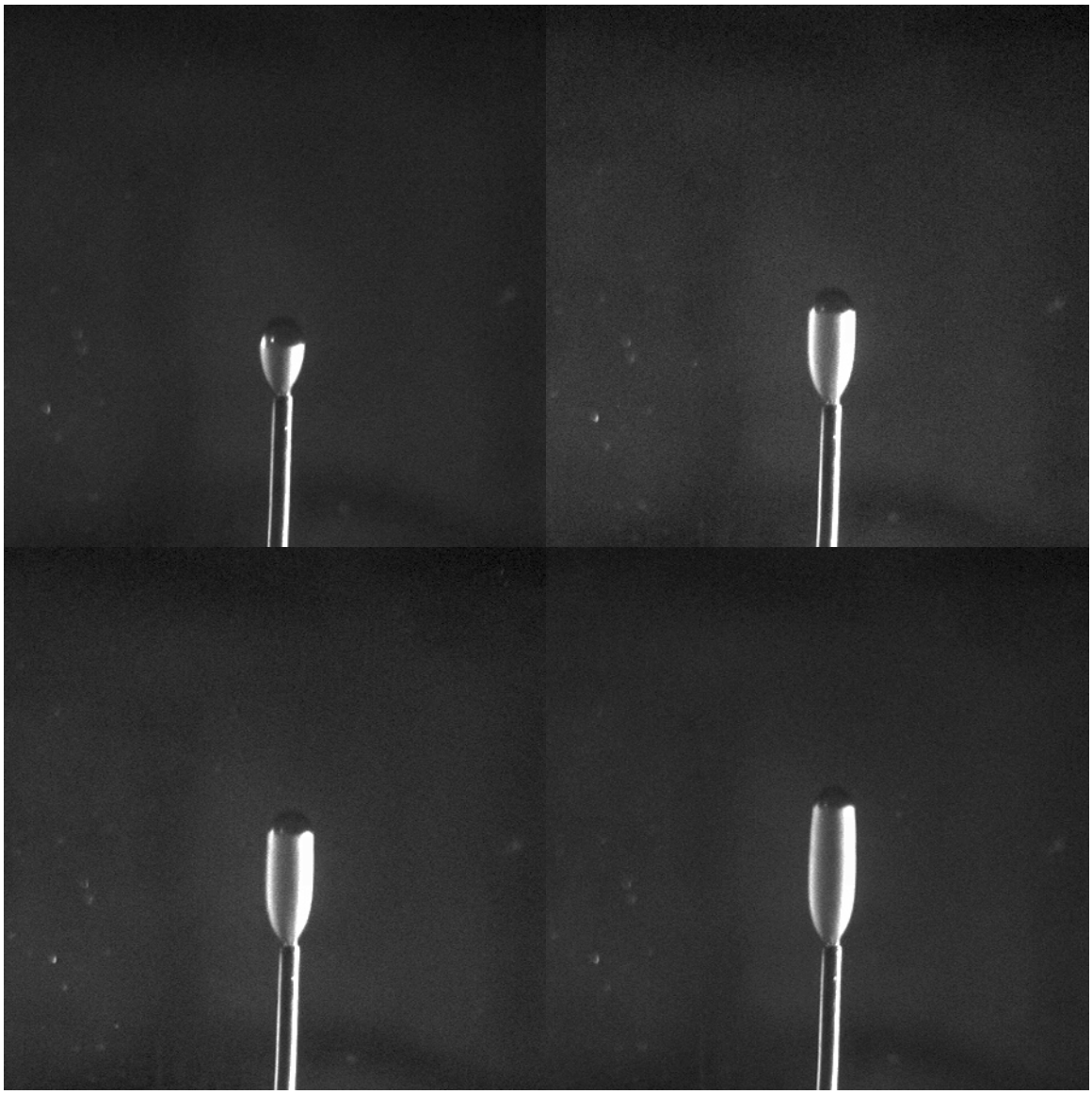

Figure III.1.19 Sequence of video images showing a hydrate film growing on the surface of an oily bubble emerging from the injector. Case H18; Neptune SPAR oil on NG3 gas. Time elapsed between the two top images was 4 seconds; the second, third and fourth images were recorded at 2 second intervals.

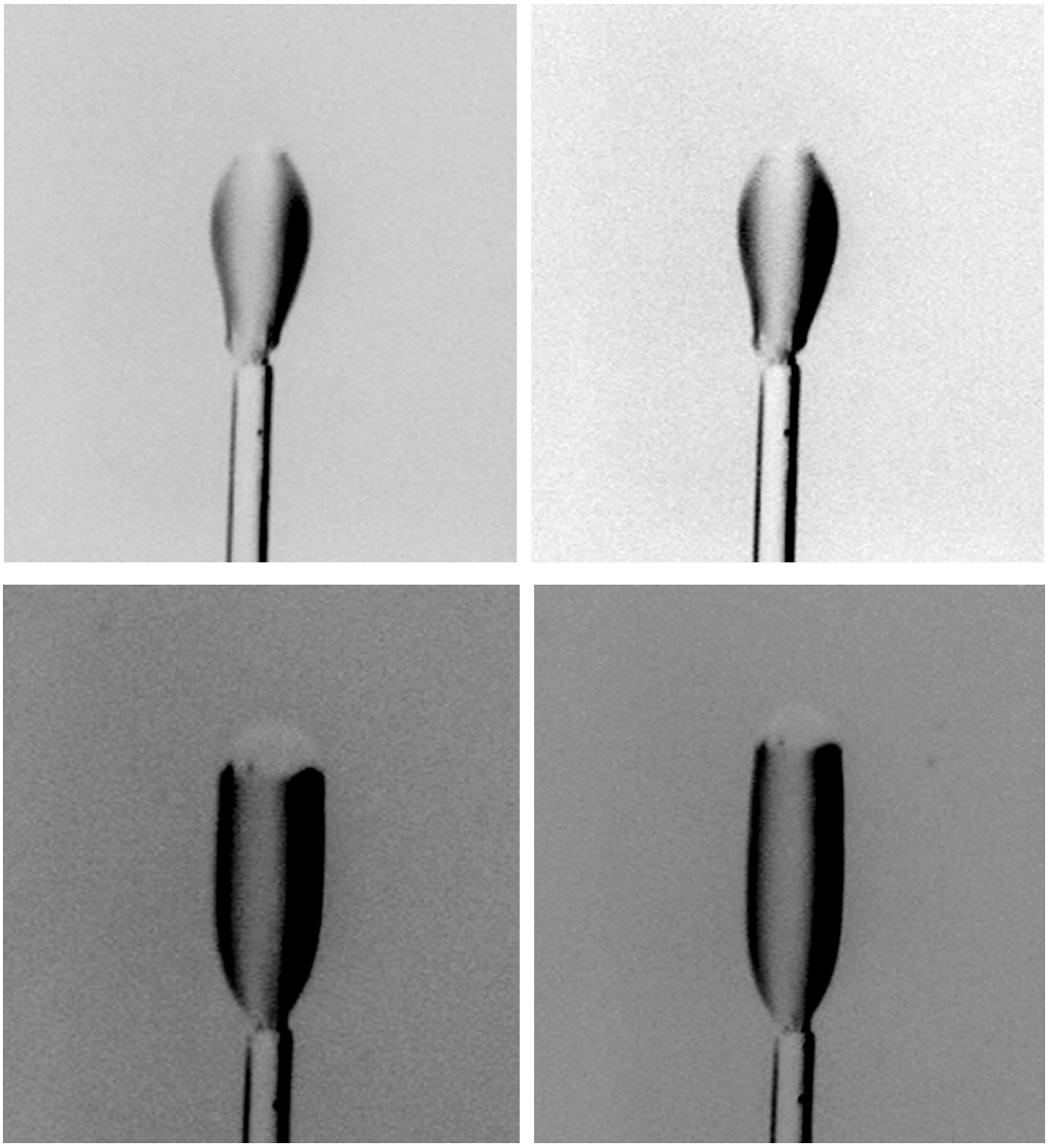

Figure III.1.20 Magnified and inverted video frames showing the upper edges of hydrate shells and the (white) cap of crude oil on the top of natural gas bubbles emerging from the injector.

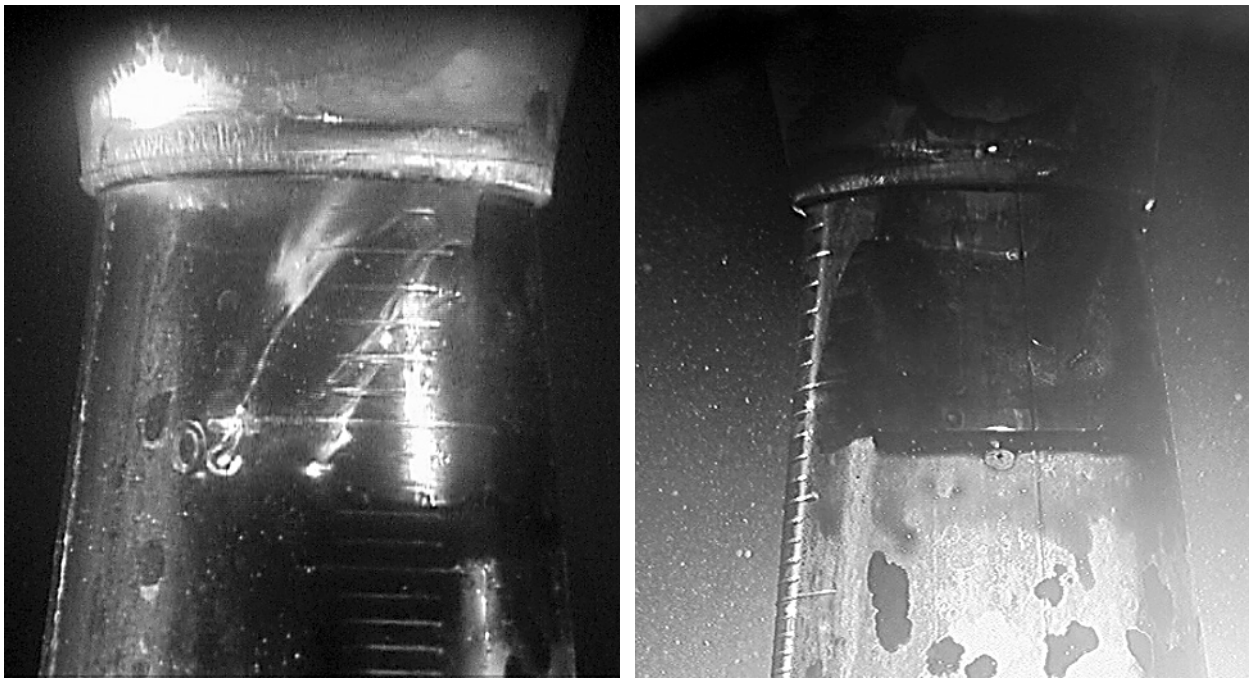

Figure III.1.21 Two views at right angles of a large bubble of NG3 gas. Nominal 2-3°C tap water flows over the 45° inclined top surface of the bubble. A layer of Platform Gail crude oil has collected at the bottom surface of the bubble and deposited on the walls of the test section. No hydrates are detected. Pressure is 6.16 MPa. The outside diameter of the clear conical test section is 2.5 cm.

III.2 MIT Results

This section presents the experimental results and the analyses outlined in Section II, followed by an application of the results to the field scale.

III.2.1 Ambient Stratification Without a Current

For multi-phase plumes in stratification (ignoring a crossflow) the important correlation parameter derived above is U_N. U_N is used to correlate measurements of plume type, intrusion layer height, and intrusion layer flux.

Figure III.2.1 combines data from Asaeda & Imberger (1993) with our own experiments to show the correlation of plume type with U_N. U_N does not predict Type 1 plumes (plumes with no subsurface intrusion) because it does not include the depth, H. The other three plume types (Types 1*, 2, and 3), however, are predicted and occur between critical values of U_N. The approximate transition values are 1.4 for the transition from Type 1* to Type 2 behavior and 2.4 for the transition from Type 2 to Type 3 behavior.

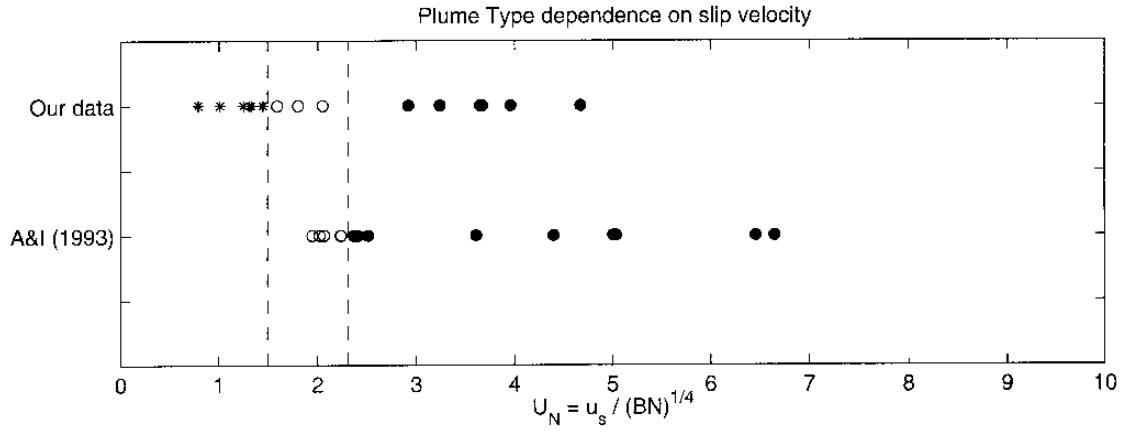

Figure III.2.1 Correlation of characteristic plume type with U_N. Stars are Type 1*, open circles are Type 2, and filled circles are Type 3. From the bottom, the first line of data is for Asaeda & Imberger (1993) and the second line of data are our experiments.

A physical understanding for the existence of the plume types comes from the parameter U_N, the ratio of bubble slip velocity to a characteristic plume fluid velocity. As the slip velocity increases, the bubbles become more independent of the motion of the plume fluid. At low U_N, the bubbles move with the fluid (low slip velocity) and we find Type 1* behavior. As the slip velocity increases, the bubbles maintain their course when the entrained fluid peels, but they remain closely enough "attached" to the fluid to provide an efficient pump and a discrete peel height (Type 2 behavior). When the bubble slip velocity increases more, the bubbles no longer provide an efficient pump and the fluid constantly separates from the rising bubble column, resulting in Type 3 behavior.

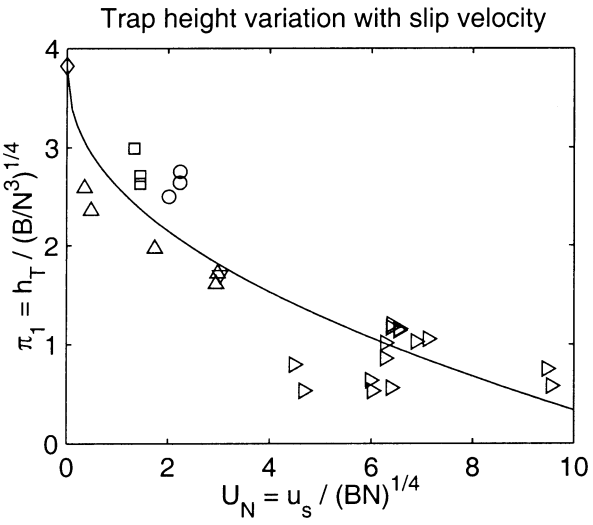

Figure III.2.2 Correlation of non-dimensional trap height with U_N. Up and down triangles are Reingold (1994), right-pointing triangles are Lemckert & Imberger (1993), circles are Asaeda & Imberger (1993), and squares are our own data. The diamond at x = 0 is the single-phase result from Morton et al. (1956).

The correlation of U_N with trap height shows a similar effect. Figure III.2.2 shows data from our experiments together with data from Reingold (1994), Asaeda & Imberger (1993), and Lemckert & Imberger (1993). The smooth curve plotted in the figure is a least-squares fit of the data yielding the relationship

$$\frac{h_T}{(B/N^3)^{1/4}} = 3.8 - 1.2U_N^{1/2}. \qquad \text{(III.2.1)}$$

The value 3.8 comes from the well-know result for a single-phase plume, where $U_N \rightarrow 0$ (Morton *et al.*, 1956). As the slip velocity increases, the trap height is reduced because the bubbles no longer go into the intrusion. When the bubbles separate from the intruding fluid, the fluid suddenly decreases in buoyancy and plunges deeper.

The intrusion layer flux, Q_i, is also correlated with U_N, as shown in Figure III.2.3. The single-phase result is taken from Fischer (1979) as the dilution at the trap height: 1.4. The smooth curve plotted in the figure is the least-squares fit of the data yielding the relationship:

$$\frac{Q_i}{(B^3/N^5)^{1/4}} = 1.4 - 0.8U_N^{0.2}. \qquad \text{(III.2.2)}$$

The intrusion layer flux is reduced from the single-phase result by two processes. First, because the trap height is reduced by the separating bubbles, there is less distance over which to entrain fluid; thus, the total flux into the intrusion is reduced. Second, bubble plumes become less efficient than single-phase plumes at pumping fluid as the slip velocity increases (Baines & Leitch 1992 and Leitch & Baines 1989). These two effects explain the downward slope of the correlation equation for larger U_N.

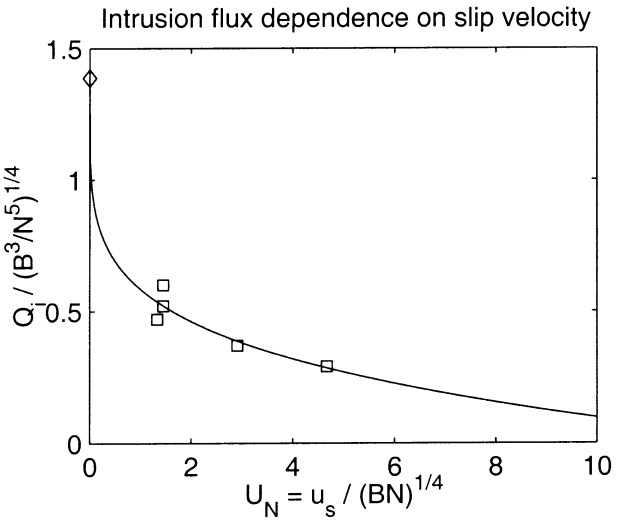

Figure III.2.3 Correlation of non-dimensional intrusion flux with U_N. Squares are our own data; the diamond at x = 0 is the single-phase result from Fischer *et al.* (1979).

III.2.2 Ambient Crossflow Without Stratification

As a summary of all the crossflow experiments, we found the following progression of stages, starting at the release point:

1. Initially, the oil/gas mixture behaves as a coherent plume and, hence, is amenable to traditional integral plume analysis.

2. Higher, the oil/gas mixture continues to behave as predicted by integral models; however, entrained fluid begins to leak from the downstream side of the plume. This occurs, presumably, because the stripping current velocity overcomes the restoring entrainment velocity, which decreases with height (Davidson & Pun 1999).

3. Above a critical height h_{cr}, the oil/gas mixture no longer behaves as a coherent mixture. Entrained water and fine oil droplets are lost downstream (or gas and large oil droplets are lost upstream), and the trajectory of the bubble column follows more closely the vector addition of the group rise velocity of the bubbles and the crossflow velocity.

4. Finally, the separated mixture of entrained fluid and fine oil droplets continues to rise in the far field due to the momentum received before separation. This far-field plume might be modeled as a single-phase plume, initiated at the separation height, h_{cr} (see further discussion in Section III.2.3).

The multi-phase plume experiments in crossflow can be described by grouping them into plumes in weak crossflow (see Section III.2.2.1) and plumes in strong crossflow (see Section III.2.2.2).

III.2.2.1 Class 1: Weak Crossflows.

In Class 1, the crossflows are weak, and the entrained fluid follows the bubble column from the injection point to the flume surface. In these cases CORMIX adequately predicts the centerline of the bubbles and the plume can be modeled as a single-phase plume in a weak crossflow. Figure III.2.4 shows four examples of plumes fitting this classification with the CORMIX predictions of plume centerline plotted over the pictures.

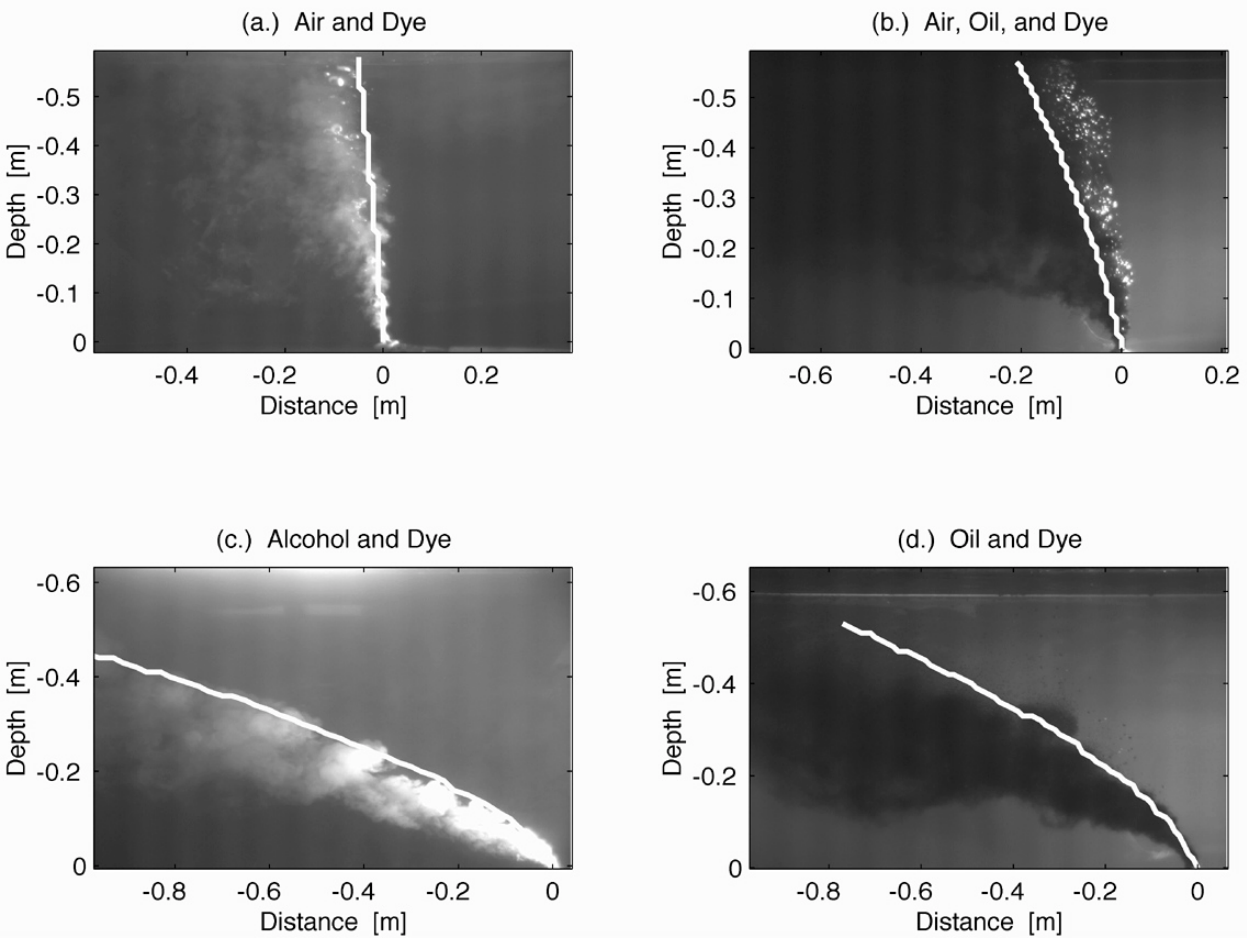

Figure III.2.4 Crossflow experiments demonstrating Class 1 behavior. The solid line represents the CORMIX prediction of the composite plume centerline.

Class 1 plumes have several important characteristics. While major separation between the lightest dispersed phase and the other components of the plume does not occur before the plumes reach the surface, two forms of leakage are observed. First, as has been observed for single-phase jets, some entrained fluid leaks into the downstream wake. Comparing frames (a.) and (b.) to frames (c.) and (d.), the leakage of entrained fluid is much greater for air bubble plumes than for the oil or alcohol plumes, even though the crossflow velocity was greater for the oil and alcohol plumes. As with the plumes in a stratified ambient, the explanation is probably that large bubbles have a more difficult time holding on to entrained plume fluid. Second, the bubbles fractionate in the crossflow, leaking smaller bubbles into the downstream wake. Although CORMIX over predicts the elevation of the plume centerlines, it performs consistently and could probably be tuned by adjusting the entrainment coefficient.

III.2.2.2 Class 2: Strong Crossflows.

For all of the plumes in Class 2, there is significant separation between the dispersed phase and entrained fluid, and CORMIX does not predict the bubble or separated oil plume trajectory above the separation height.

Figure III.2.5 shows two plumes with a single dispersed phase. For these plumes, complete separation occurs between the entrained fluid and the rising bubble column. Dye injected near the release point separates from the bubble column, but is raised a significant height due to acceleration within the bubble column, even though the dye and entrained fluid are neutrally buoyant. This indicates that, beyond the point of separation, the injected dye tracer may behave like a momentum jet. In addition, leakage is observed from the separated dye jet, and the CORMIX centerline prediction for the composite lies between the bubble column and dye jet. The bubble column has a nearly linear front and exhibits fractionation.

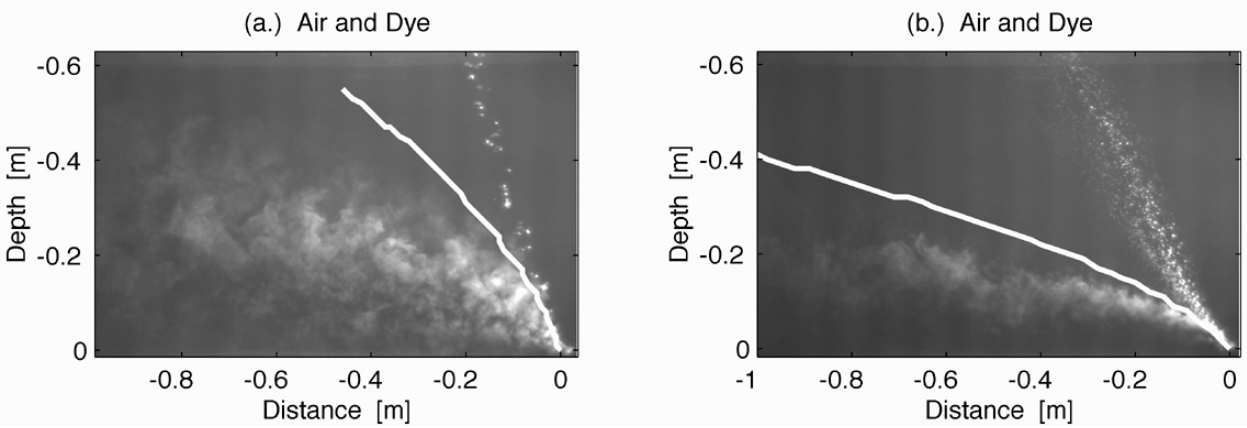

Figure III.2.5 Crossflow experiments demonstrating Class 2 behavior for two-phase plumes. The solid line represents the CORMIX prediction of the composite plume centerline.

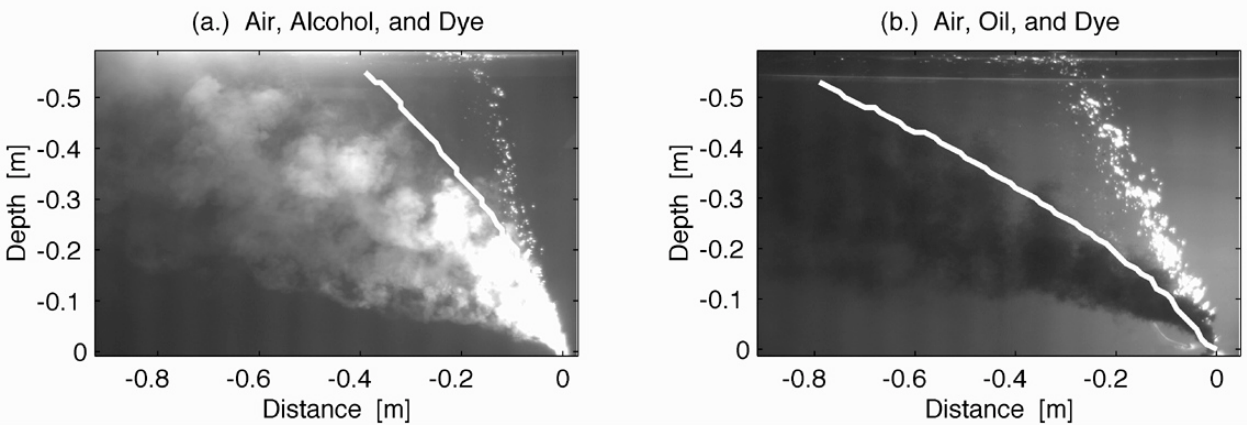

Figure III.2.6 Crossflow experiments demonstrating Class 2 behavior for multi-phase plumes. The solid line represents the CORMIX prediction of the composite plume centerline.

Figure III.2.6 shows two multi-phase plumes. Here, complete separation occurs between the air bubbles and the other dispersed phase injected with the bubble plume. CORMIX again predicts a centerline for the composite plume that lies between the rising air bubbles and the separated alcohol and oil plumes. The separated alcohol and oil plumes should probably be treated as buoyant momentum jets, since the air bubbles at the base of the plume accelerate them. Fractionation and leakage remain as characteristic features of these plumes.

III.2.2.3 Correlation Analysis

To predict the height of separation, 41 experiments summarized in Appendix B were used. Because the exact height of separation is difficult to identify, the following procedure was used. From the scaled images captured for the experiments, the highest point at which no separation had occurred was estimated first. Second, the lowest point at which complete separation had occurred was estimated. Both points were plotted in the non-dimensional parameter space and a curve was drawn separating the two points. The curve is assumed to fall on the best estimate of the transition point.

Figure III.2.7 shows the results of this correlation analysis. Points falling below the smooth curve exhibited no separation. Points falling above the curve exhibited total separation. The equation representing the smooth line is given by

$$\frac{u_a}{(B/h_{cr})^{1/3}} = 5.5\left(\frac{u_s}{(B/h_{cr})^{1/3}}\right)^{-1.8}. \qquad \text{(III.2.3)}$$

Rearranging this equation to solve for the critical transition height gives

$$h_{cr} = 6.2\frac{B}{u_a u_s^{1.9}}. \qquad \text{(III.2.4)}$$

This relationship is used in Section III.2.4 to scale the laboratory results up to the field.

III.2.3 Proposed Modified Modeling Approach

The solid lines plotted in Figures III.2.4-III.2.6 show the predicted plume trajectories using a typical integral-jet model (CORMIX). For plumes where separation occurs (Class 2) the simple jet model does not follow either the bubbles or the separated fluid.

The fact that the separated dye plume continues to rise in the lee of the bubbles indicates that momentum is transferred to the entrained fluid by the bubbles before the separation height. As a first attempt to capture these processes, CORMIX was run in two stages. First, the combined bubble, dye (and, where applicable oil or alcohol) plume was modeled as before up to the critical separation height h_{cr}. Second, the separated dye plume is modeled alone, neglecting the bubbles. The second stage is initiated at the height h_{cr} with the momentum, buoyancy, and volume flux for the entrained fluid predicted in the first stage of the modeling for the height h_{cr}. The bubbles are modeled separately above h_{cr} as the vector sum of their slip velocity and the current. Figures III.2.8-III.2.10 show results using this method for the plumes in Figures III.2.4(a), III.2.5(a), and III.2.6(b), respectively.

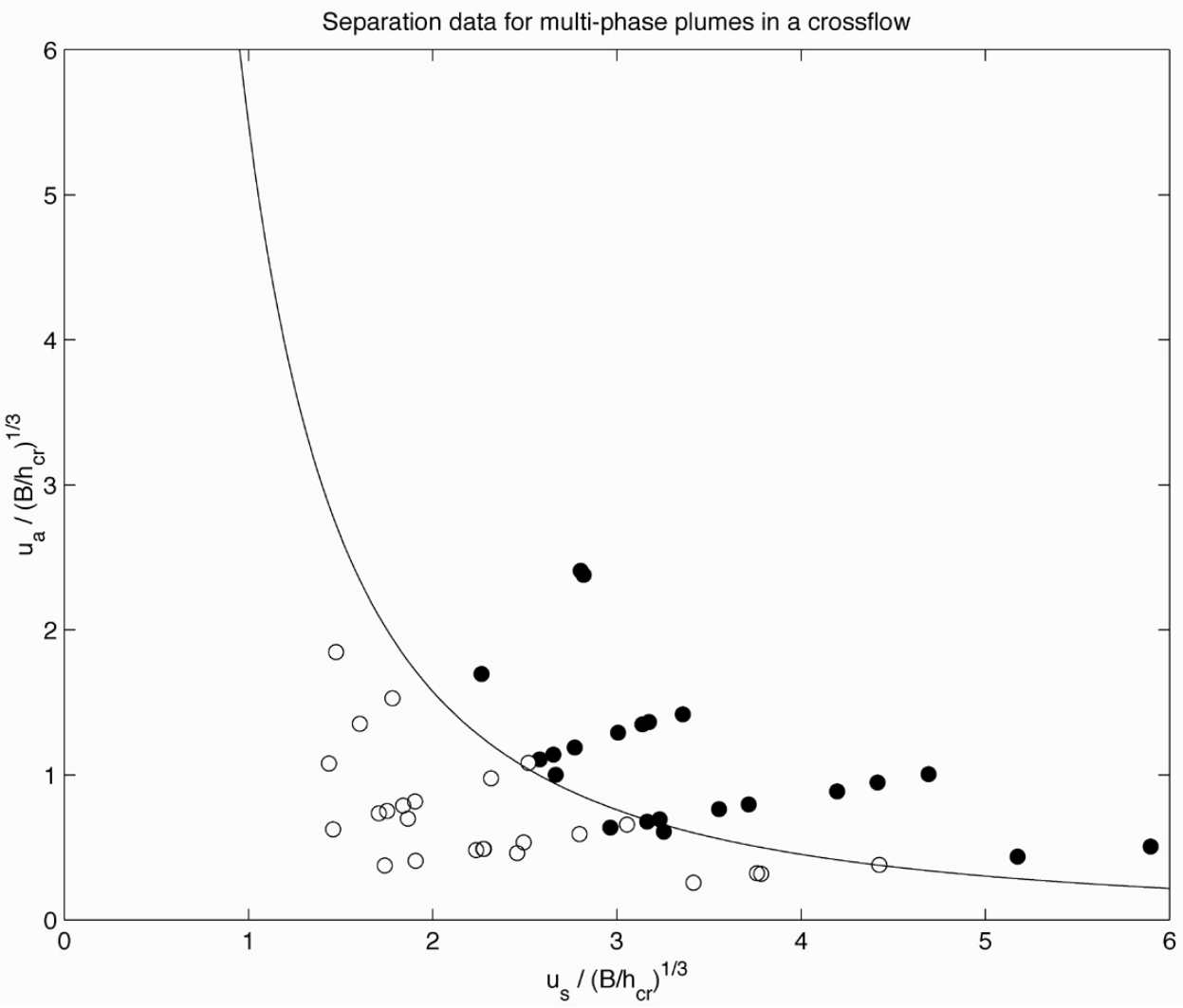

Figure III.2.7 Non-dimensional space relationship for the critical transition height, h_{cr}, for a multi-phase plume in a crossflow. Solid circles represent heights with complete separation; open circles represent heights with no separation.

Based on the figures, it looks like a traditional integral model can be used to model oil/gas plumes as long as it accounts for the process of phase separation. That is, before gas separation, both phases are included in the plume buoyancy, while following gas separation, only the oil phase is considered. The SINTEF model called DeepBlow (Johansen, 2000) takes this approach. The model uses a theoretical method to calculate the location of gas separation, but it is not clear if the separation calculations have been validated against laboratory or field data. The original Clarkson model (Yapa and Zheng, 1997) did not consider separation; however, their newest model called CDOG employs a theoretical approach to calculate gas separation, and their model results have been compared with the laboratory experiments conducted as part of this study.

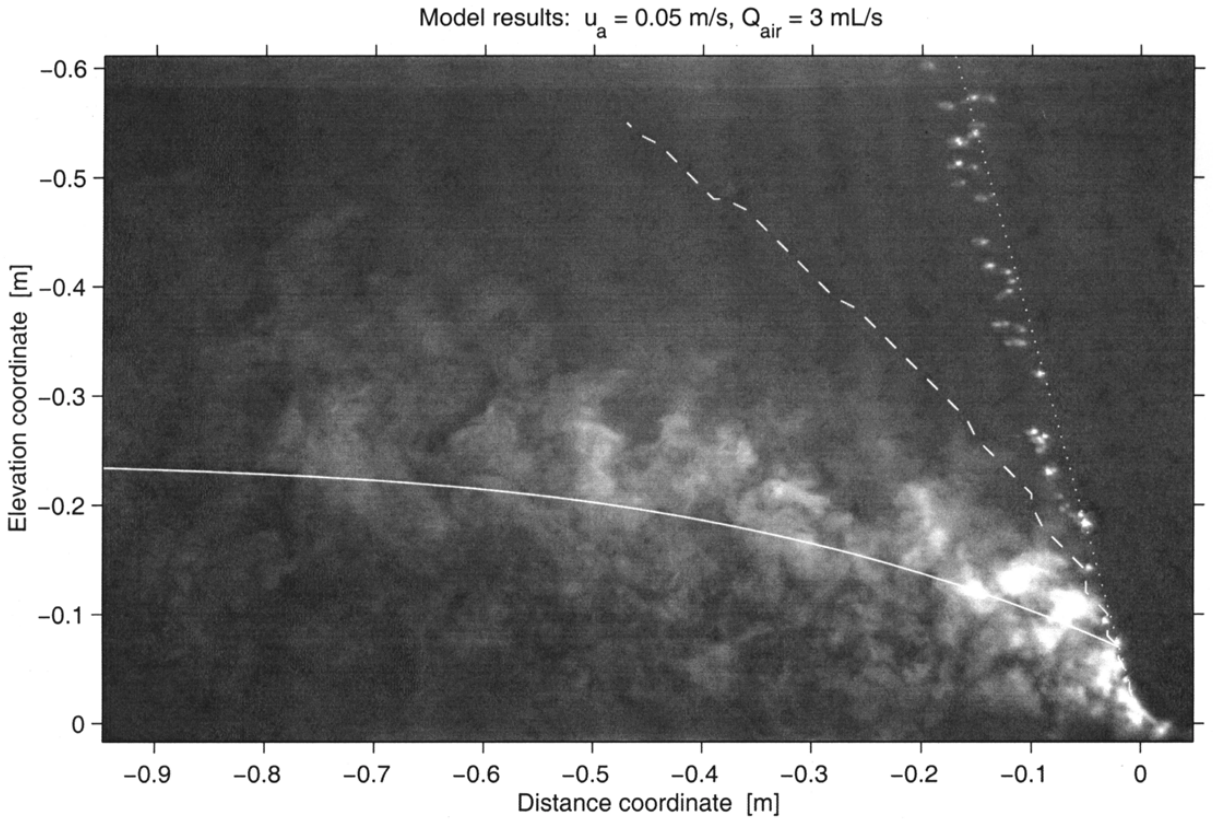

Figure III.2.8 Modified model results for a two-phase plume in a stratified crossflow (see Figure III.2.5(a)). The dashed line is the single-phase prediction; the solid and dotted lines are for the new algorithm. The dotted line is the vector sum of the bubble slip velocity and the crossflow; the solid line is a momentum jet initiated at h_{cr}.

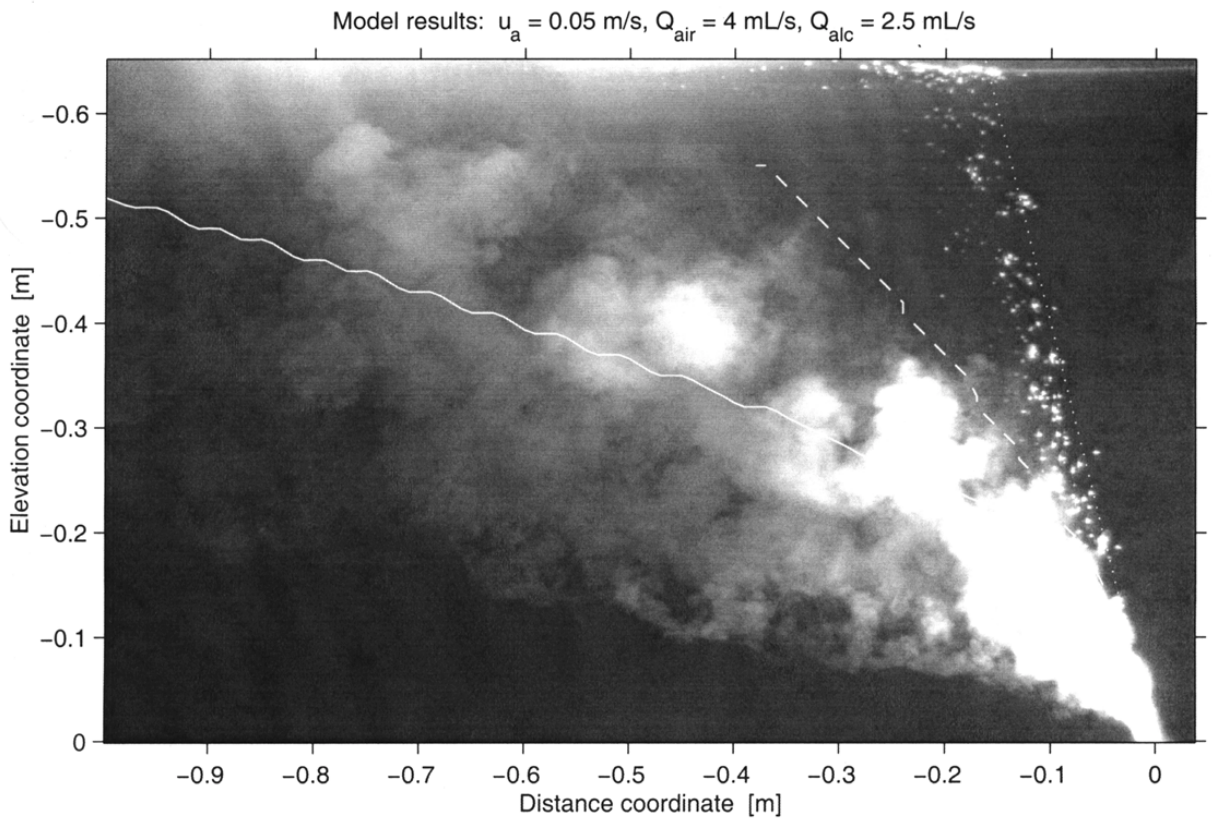

Figure III.2.9 Modified model results for a two-phase plume in a stratified crossflow (see Figure III.2.6(a)). The dashed line is the single-phase prediction; the solid and dotted lines are for the new algorithm. The dotted line is the vector sum of the bubble slip velocity and the crossflow; the solid line is a buoyant momentum jet initiated at h_{cr}.

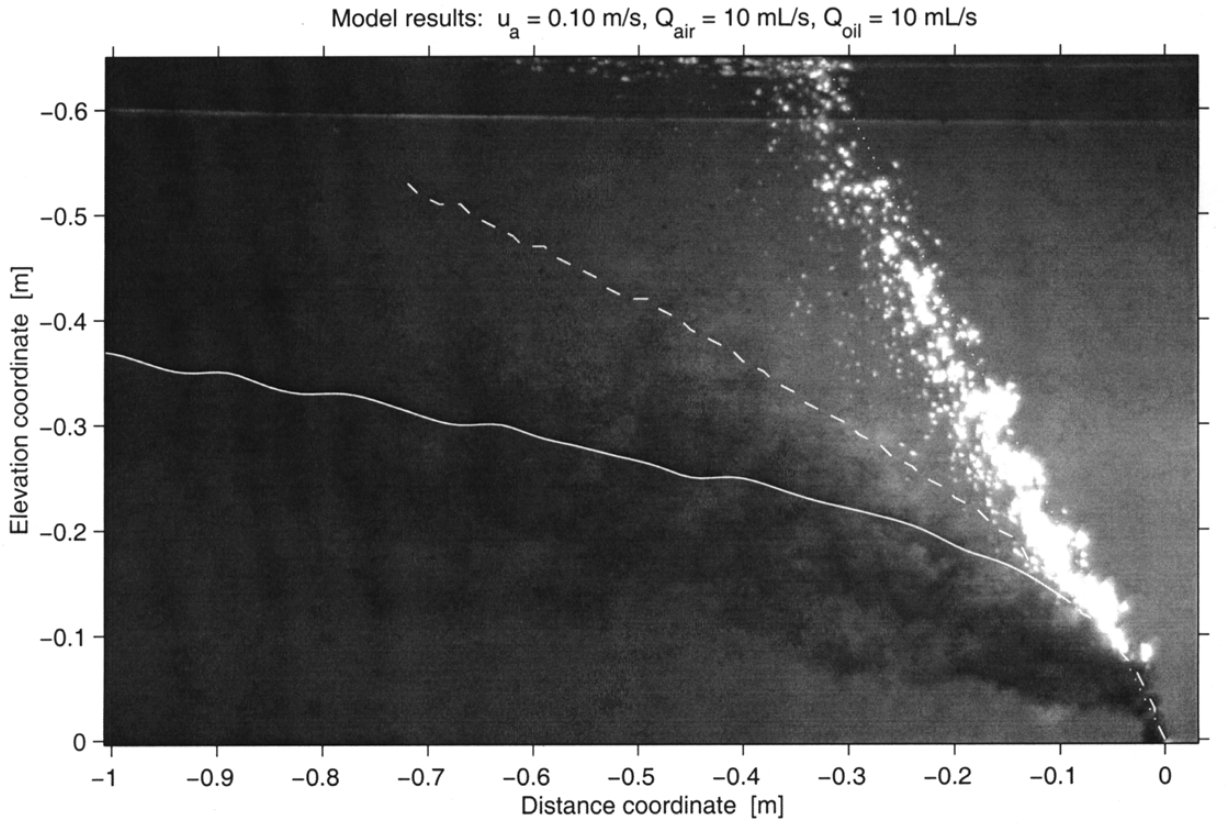

Figure III.2.10 Modified model results for a two-phase plume in a stratified crossflow (see Figure III.2.6(b)). The dashed line is the single-phase prediction; the solid and dotted lines are for the new algorithm. The dotted line is the vector sum of the bubble slip velocity and the crossflow; the solid line is a buoyant momentum jet initiated at h_{cr}.

III.2.4 Combined Effects of Stratification and Crossflow

Three experiments were conducted with both stratification and crossflow. Table III.2.1 summarizes the conditions of the experiments, plus a fourth experiment with the same apparatus but no crossflow.

Table III.2.1 Physical characteristics of the crossflow experiments with stratification. The values in columns two and three are order of magnitude estimates from (III.2.1) and (III.2.4). For these experiments $N \approx 0.5$ s^{-1} and $Q_0 = 100$ mL/min of air.

u_a [cm/s]	h_T [cm]	h_{cr} [cm]
0	$O(10)$	∞
2	$O(10)$	$O(100)$
5	$O(10)$	$O(10)$
10	$O(10)$	$O(1)$

Figure III.2.11 shows video images of the four experiments. The first experiment (without a crossflow) agrees with our stratification experiments in the taller, stagnant tank. The next experiment is for a weak crossflow (u_a = 2 cm/s, giving h_T much less than h_{cr}), where the plume is stratification dominated (separation occurs due to stratification effects before it occurs due to the crossflow). For this experiment the entrained fluid rose above the intrusion layer, peeled as it did in the no-crossflow case, and plunged to form the intrusion at the height h_T in the wake of the plume.

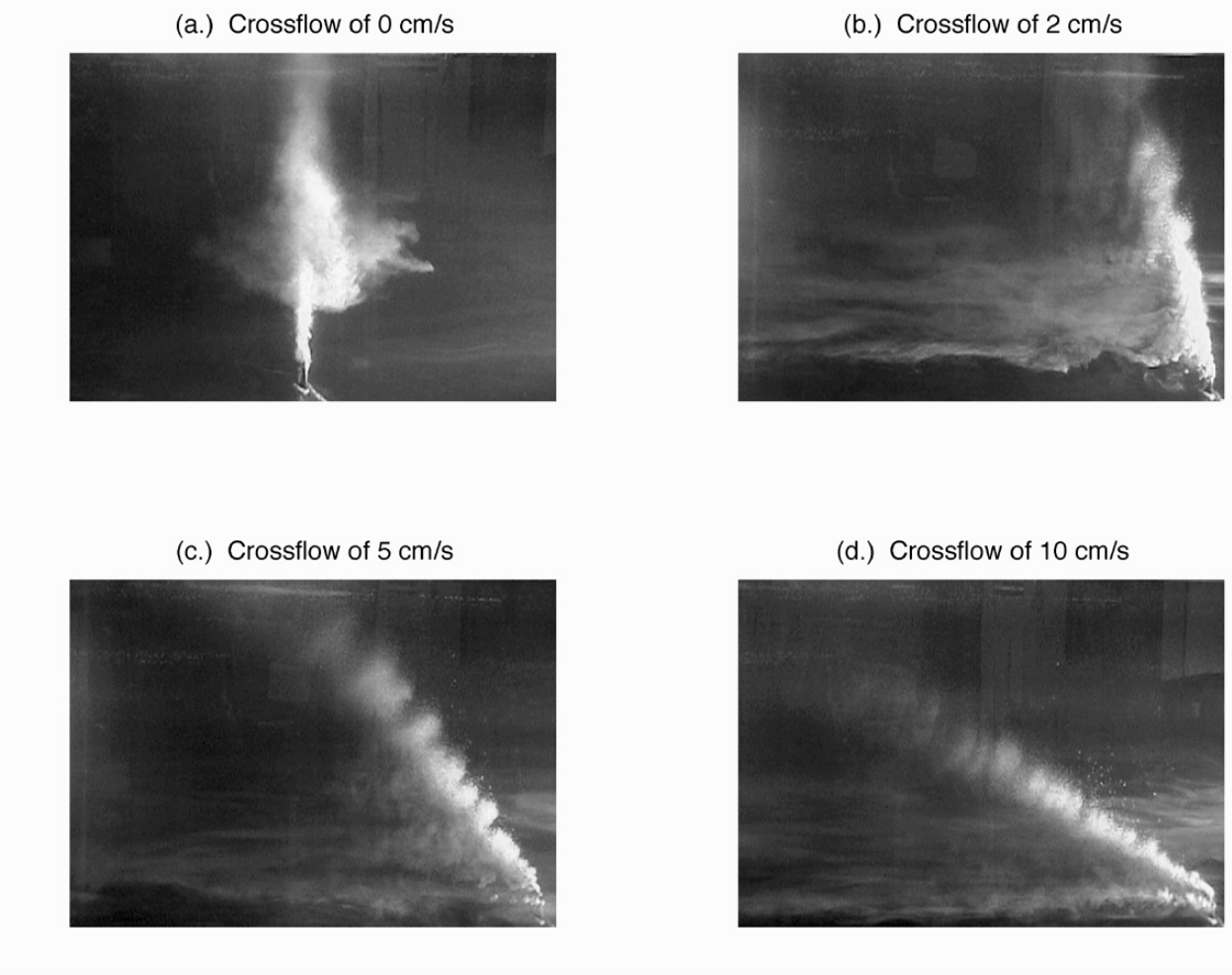

Figure III.2.11 Crossflow experiments with stratification (Q_0 = 1.7 mL/s, $N \approx 0.5$ s^{-1}, current speeds are as indicated). Some residual dye contamination complicates frames (c.) and (d.). Frame (a.) was taken with the camera zoom active which is why frame (a.) appears to have a higher intrusion height.

One difference between the weak crossflow and the no crossflow experiment is that the peeling takes place asymmetrically (in the lee of the plume) in the crossflow, rather than symmetrically (in an annular ring surrounding the plume) as in the stagnant case.

Another difference is that, with the 2 cm/s crossflow, there is significant leakage from the lower part of the plume; whereas, this is not the case for the plume in a stagnant ambient. This may be

due to the following mechanism. Because the entrained fluid is dense relative to the ambient and because the bubbles stay in a core area narrower than the full width of the plume, the outer edges of a multi-phase plume in stratification are negatively buoyant. Without a crossflow, the drag and entrainment from the inner core slowly lift these outer edges. In the presence of the crossflow, however, those dense edges are easily pulled away by the crossflow. Further experiments would have to be performed to fully understand this mechanism.

For the third experiment the effects of stratification and crossflow are comparable (u_a = 5 cm/s, giving $h_T \approx h_{cr}$). For this case some dye rose to the peel height and some dye separated at the intrusion level, but all the dye ended up at approximately the same intrusion height as for the 2 cm/s crossflow.

The final experiment for a strong crossflow (u_a = 10 cm/s, giving h_T much greater than h_{cr}) shows results for a crossflow-dominated plume (separation occurs due to crossflow effects before it occurs due to stratification). For this experiment the dye separated at the height h_{cr}, well below the previous intrusions, and no dye reached the stratification separation height, h_T. Although separation is independent of the stratification in this case, the far field plume is influenced by the stratification: stratification causes the separated plume to have a downward, trapping trajectory in the far-field.

III.2.5 Application to the Field Scale

The laboratory results can now be applied at the field scale using the non-dimensional relationships in the above equations. Two field applications are investigated. First, typical blowout scenarios for a small, medium, and large blowout are summarized in Tables III.2.2 and III.2.3.

Table III.2.2 Field-scale parameter ranges for a leak and a small, medium and large well blowout. Slip velocities were estimated from Rygg & Emilsen (1998), Rye *et al.* (1998) and Clift *et al.* (1978).

Scenario Number [--]	Spill Size [--]	*In situ* Flow Rate			Slip velocities		
		Oil [m^3/s]	Gas [m^3/s]	Hydrate [m^3/s]	Oil [cm/s]	Gas [cm/s]	Hydrate [cm/s]
1	Leak	0.001	0	0	10	30	10
2	Small	0.001	0.001	0	18	30	10
2h	Small	0.001	0	0.001	18	30	10
3	Medium	0.01	0.01	0	10-18	40	10
3h	Medium	0.01	0	0.01	10-18	40	10
4	Large	0.1	0.1	0	7-18	40	10
4h	Large	0.1	0	0.01	7-18	40	10

Table III.2.3 Field-scale predictions for a leak and a small, medium, and large well blowout at 1000 m depth. Conditions are assumed typical of the Gulf of Mexico with N = 0.002 $s^{-1}$and with the density of oil and gas hydrate assumed equal at 0.9 g/cm^3. The Net u_s is the average slip velocity of the oil, gas and hydrate, weighted by their respective buoyancy fluxes (the next column U_N is calculated using this slip velocity). The crossflow separation height h_{cr} is computed assuming a crossflow of 15 cm/s. The variable u_{ac} is the critical crossflow required to cause separation at the stratification trap height, h_T. U_N(oil) is the value of U_N computed using the slip velocity of the oil only (neglecting gas and hydrate).

Scenario Number	Net B [m^4/s^3]	Net u_s [cm/s]	U_N [--]	h_{cr} [m]	h_T [m]	u_{ac} [cm/s]	U_N(oil) [--]
1	0.001	10	2.5	4	38	2	2.5
2	0.01	29	4.3	5	44	2	2.7
2h	0.002	14	3.0	4	41	2	3.8
3	0.1	37	3.1	28	101	5	0.8-1.5
3h	0.03	10-14	1.2-1.7	43-81	94-104	9-14	1.2-2.2
4	1	37	1.7	280	235	21	0.3-0.9
4h	0.2	9-14	0.6-0.9	430-1100	197-216	37-84	0.5-1.2

From Table III.2.3 the following observations are noted:

1. The trap height h_T increases with the size of the spill.

2. From the values of U_N computed for oil alone (column 8) the oil is expected to leave a gas/hydrate plume for medium and large blowouts (values of $U_N < 1.4$ indicate droplets that would be caught in the intrusions). The potential is greatest for large blowouts in which the gas does not form a hydrate.

3. Comparing values for h_T and h_{cr}, leaks and small and medium blowouts are current dominated for a crossflow of 15 cm/s or greater. Crossflows below 1-8 cm/s are required for these plumes to become stratification dominated.

4. Large blowouts are stratification dominated.

5. Predictions for U_N (and therefore predictions of bubble/droplet fate) are very sensitive to the estimated slip velocity. The oil droplets leave the plume for medium and large spills because the slip velocities are small compared to the plume fluid velocities generated by the high buoyancy fluxes in these sized spills.

A second field application is demonstrated for the SINTEF experiments conducted in June 2000. Table III.2.4 shows the physical conditions of the experiments, and Table III.2.5 gives predicted outcomes of the experiments.

Table III.2.4 Field-scale parameter ranges for the SINTEF experiments (Johansen 1999). It is assumed that hydrates will form for all experiments using natural gas; only the first experiment uses nitrogen (a non-hydrate forming gas). For conditions in the North Sea, SINTEF estimates an ambient stratification with $N = 0.003\ s^{-1}$.

Exp. Number [--]	Spill Size [--]	*In situ* Flow Rate			Slip velocities		
		Oil [m^3/s]	Gas [m^3/s]	Hydrate [m^3/s]	Oil [cm/s]	Gas [cm/s]	Hydrate [cm/s]
1	Medium	0	0.02	0	2-10	30	10
2	Medium	0	0	0.02	2-10	30	10
3	Medium	0.02	0	0.02	2-10	30	10
4	Medium	0.02-0.03	0	0.02	2-10	30	10

Table III.2.5 Field-scale predictions for the SINTEF experiment. Variables are as indicated in Table III.2.3.

Exp. Number	Net B [m^4/s^3]	Net u_s [cm/s]	U_N [--]	h_{cr} [m]	h_T [m]	u_{ac} [cm/s]	U_N(oil) [--]
1	0.1	30	2.2	46	91	9	n/a
2	0.02	10	1.2	52	69	14	n/a
3	0.04	5-10	0.5-1.0	120-376	89-100	24-64	0.2-1.0
4	0.04-0.07	4-10	0.4-1.0	188-965	89-117	24-133	0.2-0.9

From Table III.2.5 the following observations are noted:

1. All plumes will peel well below the water surface.

2. Comparing values of h_T and h_{cr}, the first two experiments (which do not involve any oil) will be current dominated, while the last two experiments (which include oil) will be stratification dominated. Experiment 3 will be only slightly stratification dominated, so some separation is expected to occur below the peel height.

3. From the values of U_N in columns 4 and 8 we expect the following trapping of the dispersed phases. The nitrogen gas experiment (experiment 1) will not have any gas trapped in the intrusions. For the other experiments, both the hydrate and oil dispersed phases will flow into the intrusions and separate from the rising plume before initiating a secondary plume. As a result, secondary intrusion layers may be less distinct.

4. Experiments with larger bubble sizes (particularly for the oil) would cover a greater range of the variability shown in Table III.2.3.

IV SUMMARY & CONCLUSIONS

Experiments were conducted at the University of Hawaii and the Massachusetts Institute of Technology to investigate the behavior of oil and gas released into the deep ocean during underwater oil well blowout and spill events. The principal results and primary conclusions of this study include:

1. Approximate boundaries of the instability regimes of crude oil discharging into water were identified. The boundaries differ from those established in earlier studies of liquid jets in a gas and are shifted to lower values of Reynolds numbers. Relationships for the boundaries are provided in Equations III.1.1 and II.1.2.

2. As oil jet breakup in water approaches atomization, two instability mechanisms appear to operate in parallel, producing a polydispersion of droplets comprising two distinct size groups. Small droplets are generated by a short wavelength surface instability while large droplets, of the order of the oil discharge orifice, may continue to form in transitional jets from a filament of core jet fluid.

3. Although the PDPA was unable accurately to measure droplet size distributions of opaque crude oil, size histograms obtained using a clear analog fluid support the above proposed mechanism for the breakup of jets approaching atomization. To the authors' best knowledge, these size histograms represent a unique addition to the database on liquid-liquid breakup.

4. The data do not indicate any clear relationship between orifice diameter and the size of the fine droplets. Additional experiments need to be conducted to confirm this apparent scale independence.

5. Plume type depends on U_N such that Type 1* plumes occur for U_N less than about 1.4, Type 2 plumes occur for U_N between about 1.4 and 2.4, and Type 3 plumes occur for U_N greater than about 2.4.

6. Field plumes exhibiting Type 1* behavior would have oil droplets that initially are trapped in the intrusion layers. Trapping oil in the intrusion layers produces two results. First, the droplets are dispersed over a wide area, the size of the area depending on the degree to which the droplets stay with the intruding water. Second, the dispersed oil droplets lose (at least some) of their identity with the plume and can rise only at their slip velocity. A random-walk dispersion model would be a good candidate model for simulating the fate of oil droplets stripped from the plume by an intrusion layer.

7. The trap height, h_T, and the intrusion layer flux for the first intrusion, Q_i, both decrease with increasing U_N. This is due to the loss of buoyancy from the bubbles/droplets when the bubbles/droplets separate from the fluid. As U_N increases, the bubbles/droplets become more independent of the fluid and separation occurs earlier and more completely.

8. Separation occurs in multi-phase plumes in a crossflow at the critical height, h_{cr}, given by (III.2.4).

9. Multi-phase plumes in a crossflow differ from single-phase plumes when the crossflow separates the entrained fluid (and the fine oil droplets) from the rising bubble column. Above that height the gas bubbles can be modeled as the vector sum of their group rise velocity and the current speed, and the separated fluid can be modeled as a single-phase plume with the appropriate initial volume, buoyancy, and momentum flux.

10. Multi-phase plumes in a stratified crossflow have varied behavior, depending on the relative strength of the stratification to the crossflow. When the trap height predicted for stratification, h_T, is much less than the separation height for the crossflow, h_{cr}, the plume is stratification dominated, and the crossflow can be neglected in the near-field. In the opposite case, where h_{cr} is much less than h_T, separation will occur due to the crossflow and the plume is crossflow dominated: stratification can be neglected in the near-field of the plume. When the two separation heights are comparable, some fluid is stripped by the current and some fluid rises to the peel height, but the end result is that fluid intrudes in the lee of the plume at $h_T \approx h_{cr}$.

11. Hydrate formation on rising bubbles of natural gas is fostered by large bubbles and high gas loading. Hydrate formation appears to begin in the wake or on downstream surfaces of bubbles. If gas loading is high (i.e., the concentration of bubbles is high), then the hydrate film can promote bubble agglomeration and growth of the hydrate mass

12. The presence of oil at the gas-water interface can exercise an inhibiting effect of the initiation and growth of hydrate films. Additional experiments are warranted to clarify the influence of oil type, film thickness, and other factors.

V RECOMMENDATIONS FOR FUTURE WORK

1. Experiments need to be conducted at lower values of Ohnesorge number (i.e., using larger orifices and flow rates) to confirm the boundaries of the crude oil-water instability regimes that were identified in the present study.

2. Larger scale experiments also should be performed to determine if the size of fine droplets produced on the surface of the oil jet are independent or only weakly dependent on the dimension of the discharge orifice. This has important implications with regard to the far-field dispersion of the contaminant material.

3. Effort should be made to develop techniques to measure the full size distribution of droplets produced by transitional and fully atomized liquid jets in another liquid.

4. .The SINTEF field experimental data should be used to verify the correlation equations derived for this report from the laboratory experiments.

5. The model of Yapa & Zheng (1999) should be adapted to account for the separation observed in crossflow-dominated plumes illustrated above and should be tested for the momentum jet/plume region after separation.

6. Additional laboratory experiments in stratification and crossflow should investigate the enhanced leakage observed in stratification-dominated plumes.

7. Multiple separating dispersed phase plumes (plumes with several bubble/droplet classes having different slip velocities) should be studied in the laboratory and compared to the results presented above (with new theoretical relationships derived if necessary). These

effects are important in field-scale plumes where gas, gas hydrate and oil may be present simultaneously in a wide range of bubble/particle/droplet sizes.

8. Experiments are warranted to confirm the effects of oil at the gas-water interface on hydrate formation. Studies should systematically examine the influence oil type and film thickness.

REFERENCES

Allisy, A., *Proceedings of the International School of Physics "Enrico Fermi," Course LXVIII,* (A.F. Milone & P. Giacomo, eds.), North-Holland, Amsterdam (1980).

Asaeda, T. and J. Imberger, "Structure of Bubble Plumes in Linearly Stratified Environments," *J. Fluid Mech.*, **249**, pp. 35-57, 1993.

Bachalo, W.D., "Method for Measuring the Size and Velocity of Spheres by Dual-Beam Light-Scatter Interferometry," *Appl. Opt.*, **19**, pp. 363-370, 1980.

Bachalo, W.D., "Experimental Methods in Multiphase Flows, *Int. J. Multiphase Flow,* **20**(Suppl.), pp. 261-295, 1994

Bachalo, W.D. and M.J. Houser, "Phase/Doppler Spray Analyzer for Simultaneous Measurements of Drop Size and Velocity Distributions," *Opt. Eng.*, **23**(5), pp. 583-590, 1984.

Baines, W.D. and A.M. Leitch, "Destruction of Stratification by Bubble Plumes," *J. Hydr. Engrg.*, **118**, pp. 559-577, 1992.

Berecz, E., and Balla-Achs, M., *Gas Hydrates*, Elsevier Science Publishing Company, Inc., New York, (1983).

Bishnoi, P.R., "Hydrate Formation and Oil/Gas Well or Pipeline Blowout in Deep Waters," lecture presented at the DSTF Modeling Workshop, Honolulu, Hawaii, February 1999.

Brewer, P.G., F.M. Orr, Jr., G. Friederich, K.A. Kvenvolden, D.L. Orange, J. McFarlane and W. Kirkwood, "Deep Ocean Field Test of Methane Hydrate Formation from a Remotely Operated Vehicle," *Geology*, **25**(5), pp. 407-415, 1997.

Chandrasekhar, S., *Hydrodynamic and Hydromagnetic Stability,* Dover, New York (1981).

Clift, R., J.R. Grace, and M.E. Weber, *Bubbles, Drops, and Particles*, Academic Press, New York, NY (1978).

Cruickshank, M.J. and S.M. Masutani, "Methane Hydrate Research & Development," *Sea Technology*, **40**(8), 69 (1999).

Davidson, M.J. and K.L. Pun, "Weakly Advected Jets in a Cross-flow," *J. Hydr. Engrg.*, **125**, pp. 47-58, 1999.

Fendinger, N.J., R.G. Lehmann, and E.M. Mihaich, "Polydimethylsiloxane," Chapt. 7 in *The Handbook of Environmental Chemistry; Organosilicon Materials, Vol. 3, Part H* (G. Chandra, ed.), Springer-Verlag, Berlin (1997).

Fingas, M., personal communication, 1999.

Gornitz, V. and I. Fung, "Potential Distribution of Methane Hydrates in the World's Oceans," *Glob. Biogeochem. Cyc.* **8**, 335, 1994.

Grant, R.P. and S. Middleman, "Newtonian Jet Instability," *AIChE. J.*, **12**(4), pp. 669-678, 1966.

Gytre, T., J.E.Ø. Nilsen, J.E. Stiansen and S. Sundby, "Resolving Small Scale Turbulence with Acoustic Doppler and Acoustic Travel Time Difference Current Meters from and Underwater Tower," *Trans. IEEE*, pp. 442-450, 1996.

Hoffmann, H. and W. Ulbricht, "Surface Activity and Aggregation Behavior of Siloxane Surfactants," Chapt. 4 in *Silicone Surfactants* (R.M. Hill, ed.), Marcel Dekker, New York (1999).

Johansen, Ø., "Field Experiment to Study the Behavior of a Deepwater Blowout," Technical Proposal No. STF66-99043, SINTEF, Trondheim, Norway (1999).

Johansen, Ø., "DeepBlow--a Lagrangian Plume Model for Deep Water Blowouts, Spill Science & Technology Bulletin, 6(2):103-111, 2000.

Kinoshita, C.M., H. Teng, and S.M. Masutani, "A Study of the Instability of Liquid Jets and Comparison with Tomotika's Analysis," *Int. J. Multiphase Flow,* **20**(3), pp. 523-533, 1994.

Kitamura, Y. and T. Takahashi, "Stability of Jets in Liquid-Liquid Systems," Chapt. 19 in *Encyclopedia of Fluid Mechanics, Vol. 2* (N.P. Cheremisinoff, ed.), Gulf Publishing Company, Houston, TX (1986).

Kumar, A. and S. Hartland, "Correlation for Drop Size in Liquid/Liquid Spray Columns," *Chem. Eng. Commun.*, **31**, pp. 193-207, 1984.

Kvenholden, K.A., "Methane Hydrate–A Major Reservoir of Carbon in the Shallow Geosphere," *Chemical Geology* **71**, 41, 1988.

Kvenholden, K.A., G.D. Ginsburg, and V.A. Soloviev, "Worldwide Distribution of Subaquatic Gas Hydrates," *Geo-Marine Letters* **13**(1), 32, 1993.

Lefebvre, A.H., *Atomization and Sprays,* Hemisphere Publishing Company, New York (1989).

Leifer, I., personal communication, 1999.

Lemckert, C.J. and J. Imberger, "Energetic Bubble Plumes in Arbitrary Stratification," *J. Hydr. Engrg.*, **119**, pp. 680-703, 1993.

Leitch, A.M. and W.D. Baines, "Liquid Volume Flux in a Weak Bubble Plume," *J. Fluid Mech.*, **205**, pp. 77-98, 1989.

Maini, B. and P.R. Bishnoi, "Experimental Investigation of Hydrate Formation Behaviour of a Natural Gas Bubble in a Simulated Deep Sea Environment," *Chem. Eng. Sci.*, **36**, pp. 183-189, 1981.

Masutani, S.M., C.M. Kinoshita, T. Ho, G.C. Nihous, and L.A. Vega, "An Experiment to Simulate Ocean Disposal of Carbon Dioxide," *Energy Convers. Mgmt*, **34**, 865, 1993.

Masutani, S.M., R.B. Coffin, and P.K. Takahashi, "An International Partnership in Seabed Methane Hydrates R&D," presented at the 23rd Meeting of the Marine Facilities Panel of the U.S.-Japan Cooperative Program in Natural Resources (UJNR), May 2000.

Max, M.D. and M.J. Cruickshank, "Extraction of Methane from Oceanic Hydrate System Deposits," Paper OTC 10727, presented at the 1999 Offshore Technology Conference, Houston, Texas, 3-6 May 1999.

Miesse, C.C., "Correlation of Experimental Data on the Disintegration of Liquid Jets," *Ind. Eng. Chem.*, **47**, 1690, 1955.

Morton, B., G.I. Taylor, and J.S. Turner, "Turbulent Gravitational Convection from Maintained and Instantaneous Sources," *Proc. R. Soc. London Ser. A*, **234**, pp. 1-23, 1956

Naqwi, A.A. and F. Durst, "Light Scattering Applied to LDA and PDA Measurements Part 1: Theory and Numerical Treatments," *Part. Part. Syst. Charact.*, **8** pp. 245-258, 1991.

Ohnesorge, W. von, "Formation of Drops by Nozzles and the Breakup of Liquid Jets," *Z. Angew. Math. Mech*., **16**, 355-358, 1936.

Rayleigh, Lord, *Theory of Sound*, Dover, New York (1945).

Reingold, L.S., "An Experimental Comparison of Bubble and Sediment Plumes in Stratified Environments," M.S. Thesis, Dept. of Civil & Environmental Engineering., MIT, Cambridge, MA (1994).

Reitz, R.D., "Atomization and Other Breakup Regimes of a Liquid Jet," Ph.D. Thesis, Princeton University (1978).

Reitz, R.D. and F.V. Bracco, "Mechanism of Breakup of Round Liquid Jets," Chapt. 10 in *Encyclopedia of Fluid Mechanics, Vol. 3* (N.P. Cheremisinoff, ed.), Gulf Publishing Company, Houston, TX (1986).

Reynolds, W.C., "Thermodynamic Properties in SI," published by Department of Mechanical Engineering, Stanford University, Stanford, CA (1979).

Rochow, E.G., *Silicon and Silicone*, Springer-Verlag, Berlin (1987).

Rye, H., Ø. Johansen, and H. Koderup, "Drop Size Formation from Deep Water Blowouts," Tech. Report No. STF66F98090, SINTEF, Trondheim, Norway (1998).

Rygg, O.B. and M.H. Emilsen, "A Parameter Study of Blowout Rates for Deep Water and Their Effect on Oil Droplet and Gas Bubble Generation," Technical Report, Well Flow Dynamics, Billingstad, Norway (1998).

Sankar, S.V. and W.D. Bachalo, "Response Characteristics of the Phase Doppler Particle Analyzer for Sizing Spherical Particles Larger than the Light Wavelength," *Appl. Opt.*, **30**(12) pp. 1487-1496, 1991.

Sloan, E.D., Jr., *Clathrate Hydrates of Natural Gases*, Marcel Dekker, New York (1989).

Szczepanski, R., B. Edmonds, N. Brown, and T. Hamilton, "Research Provides Clues to Hydrate Formation and Drilling-Hazard Solutions," *The Oil and Gas Journal*, **96**(10), pp. 52-58, 1998.

Teng, H., "Laminar Instability of Cylindrical Liquid Jets," Ph.D. Thesis, Department of Mechanical Engineering, University of Hawaii (1994).

Teng, H., C.M. Kinoshita, and S.M. Masutani, "Prediction of Droplet Size from the Breakup of Cylindrical Liquid Jets," *Int. J. Multiphase Flow,* **21**(1), pp. 129-136, 1995.

Tomotika, S., "On the Instability of a Cylindrical Thread of a Viscous Liquid Surrounded by Another Viscous Fluid," *Proc. R. Soc.,* **A150**, 322, 1935.

Tomotika, S., "Breaking Up of a Drop of Viscous Liquid Immersed in Another Viscous Fluid Which is Extending at a Uniform Rate," *Proc. R. Soc. London Ser. A,* **A153**, pp. 302-320, 1936.

Weber, C., "Disintegration of Liquid Jets," *Z. Angew. Math. Mech*., **11**(2), pp. 136-159, 1931

Yapa, P.D. and L. Zheng, "Simulation of Oil Spills from Underwater Accidents I: Model Development," *Journal of Hydraulic Research* **35**(5), pp. 673-687, 1997.

Yapa, P. D. and L. Zheng, "Modeling Underwater Oil/Gas Jets and Plumes," *J. Hydr. Engrg.*, **125**, pp. 481-491, 1999.

Appendix A: Oil Properties

Properties of the four deep crude oils and the silicone fluid (polydimethylsiloxane) used in the breakup experiment are presented below. Silicone fluid properties were provided by the manufacturer or taken from the literature (Rochow, 1987; Fendinger *et al*., 1997; Hoffmann & Ulbricht, 1999). Analyses of the crude oil samples were performed by the Environmental Technology Centre of Environment Canada. Additional information on oil testing procedures and properties can be found at the Environmental Technology Centre website at www.etcentre.org.

Refractive indices were measured using conventional laboratory refractometers. Samples of the four crude oils and the silicone fluid were sent to Hauser Laboratories in Boulder, Colorado. Hauser Laboratories was unable to measure the refractive indices of the crude oils. Samples were then analyzed by the UH researchers using a Bausch & Lomb precision refractometer at the Hawaii Agricultural Research Center (HARC) and at UH using an inexpensive refractometer sold by Fisher Scientific. The HARC analyses were performed at 20°C using a constant temperature bath. The UH instrument was not equipped to maintain constant temperature; measurements were performed at room temperature (approximately 21–24°C). Results are summarized in Table A.1. The HARC and UH values are averages for 2-3 samples.

Table A.1 Refractive indices of SPF96-20 silicone fluid and four deepwater crude oils.

Oil Name	Index of refraction measured by Hazen	Index of refraction measured at HARC	Index of refraction measured at UH
Genesis	off scale (>1.520)	1.5016	1.492
Mars TLP	off scale (>1.520)	1.5037	1.492
Neptune SPAR	off scale (>1.520)	1.4872	1.485
Platform Gail	off scale (>1.520)	1.5180	1.517
Silicone fluid SPF96	1.400	1.4150	1.400

Other property information is given below.

<u>Genesis</u>
Origin: Gulf of Mexico, USA

Equation(s) for Predicting Evaporation

$$\%Ev = (2.12 + 0.045T)\ln(t)$$

where %Ev = weight percent evaporated; T = surface temperature [°C]; t = time [minutes]

Water Content (weight %)

Evaporation (weight %)	
0	0.4
8	< 0.1
15	< 0.1
23	< 0.1

Density, ρ [g/mL]

Evaporation (weight %)	Temperature [°C]	
0	15	0.8841
	25	0.8769
8	15	0.9074
	25	0.9006
15	15	0.9223
	25	0.9152
23	15	0.9364
	25	0.9301

Dynamic Viscosity, μ [cP]

Evaporation (weight %)	Temperature [°C]	
0	15	26
	25	18
8	15	66
	25	40
15	15	157
	25	90
23	15	543
	25	255

Emulsion Formation

Evaporation
(weight %)

0	Visual stability: none	
8	Visual stability: none	
15	Visual stability: none	
23	Visual stability: meso	
	Viscosity [cP]:	10,510
	Complex modulus [mPa]:	26,450
	Water content [wt %]:	62

Mars TLP
Origin: Gulf of Mexico, USA

Equation(s) for Predicting Evaporation

$\%Ev = (2.18 + 0.045T)\ln(t)$

where %Ev = weight percent evaporated; T = surface temperature [°C]; t = time [minutes]

Water Content (weight %)

Evaporation (weight %)	
0	0.6
8	0.1
17	0.2
26	< 0.1

Density, ρ [g/mL]

Evaporation (weight %)	Temperature [°C]	
0	15	0.8883
	25	0.8817
8	15	0.9122
	25	0.9056

17	15	0.9331
	25	0.9260
26	15	0.9520
	25	0.9461

Dynamic Viscosity, μ [cP]

Evaporation (weight %)	Temperature [°C]	
0	15	33
	25	24
8	15	93
	25	57
17	15	404
	25	171
26	15	2,237
	25	963

Emulsion Formation

Evaporation (weight %)		
0	Visual stability: none	
8	Visual stability: meso	
	Viscosity [cP]:	5,836
	Complex modulus [mPa]:	12,750
	Water content [wt %]:	63
17	Visual stability: meso	
	Viscosity [cP]:	10,520
	Complex modulus [mPa]:	30,800
	Water content [wt %]:	65
26	Visual stability: meso	
	Viscosity [cP]:	30,660
	Complex modulus [mPa]:	94,500
	Water content [wt %]:	62

Neptune SPAR (Viosca Knoll Block 826)
Origin: Gulf of Mexico, USA

Equation(s) for Predicting Evaporation

$$\%Ev = (3.75 + 0.045T)\ln(t)$$

where %Ev = weight percent evaporated; T = surface temperature [°C]; t = time [minutes]

Water Content (weight %)

Evaporation (weight %)	
0	0.1
8	< 0.1
15	< 0.1
23	< 0.1

Density, ρ [g/mL]

Evaporation (weight %)	Temperature [°C]	
0	15	0.8697
	25	0.8613
8	15	0.8826
	25	0.8749
15	15	0.8925
	25	0.8847
23	15	0.8986
	25	0.8930

Dynamic Viscosity, μ [cP]

Evaporation (weight %)	Temperature [°C]	
0	15	17
	25	13
8	15	42
	25	24

15	15	84
	25	44
23	15	187
	25	76

Emulsion Formation

Evaporation
(weight %)

0	Visual stability: none	
8	Visual stability: none	
15	Visual stability: meso	
	Viscosity [cP]:	14,120
	Complex modulus [mPa]:	545,000
	Water content [wt %]:	48
23	Visual stability: stable	
	Viscosity [cP]:	31,240
	Complex modulus [mPa]:	925,000
	Water content [wt %]:	63

<u>Platform Gail</u>
Origin: California, USA

Equation(s) for Predicting Evaporation

$$\%Ev = (1.68 + 0.045T)\ln(t)$$

where %Ev = weight percent evaporated; T = surface temperature [°C]; t = time [minutes]

Water Content (weight %)

Evaporation
(weight %)

0	1.3
7	0.3
13	0.1
21	< 0.1

Density, ρ [g/mL]

Evaporation (weight %)	Temperature [°C]	
0	15	0.9297
	25	0.9224
7	15	0.9489
	25	0.9422
13	15	0.9645
	25	0.9585
21	15	0.9810
	25	0.9752

Dynamic Viscosity, μ [cP]

Evaporation (weight %)	Temperature [°C]	
0	15	406
	25	196
7	15	1,450
	25	604
13	15	7,092
	25	2,723
21	15	161,500
	25	363,400

Emulsion Formation

Evaporation (weight %)		
0	Visual stability: stable	
	Viscosity [cP]:	35,820
	Complex modulus [mPa]:	120,000
	Water content [wt %]:	76
7	Visual stability: stable	
	Viscosity [cP]:	69,520
	Complex modulus [mPa]:	202,500
	Water content [wt %]:	75

13	Visual stability: stable	
	Viscosity [cP]:	112,800
	Complex modulus [mPa]:	337,500
	Water content [wt %]:	67
21	Visual stability: entrained	
	Viscosity [cP]:	398,200
	Complex modulus [mPa]:	1,210,000
	Water content [wt %]:	44

Silicone Fluid (SPF96-20)
Manufacturer: CLEARCO Products Co., Inc., Bensalem, PA

Description: pure polydimethylsiloxane
Appearance & odor: clear, colorless, odorless liquid

Boiling point:	> 400°F (> 204°C)
Specific Gravity (25°C):	0.98
Vapor Pressure (20°C):	negligible
Solubility in water (20°C):	insoluble
Solubility in organic solvent:	soluble in toluene
Surface Tension:	20 – 21 dyne/cm
Kinematic viscosity:	see figure below re-plotted from manufacturer's graph; ν is given in centistokes

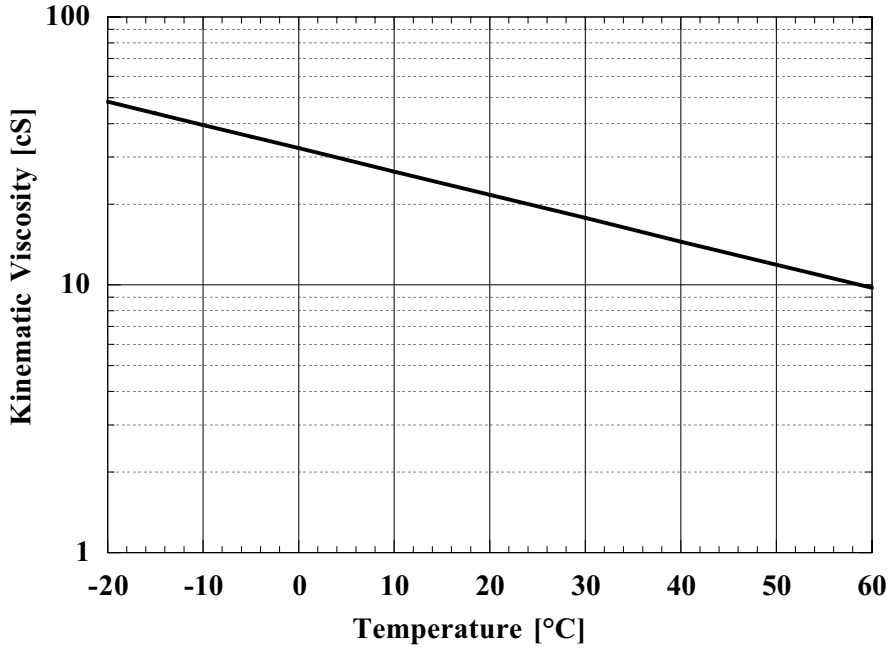

Figure A.1 Kinematic viscosity as a function of temperature for CLEARCO SPF96-20.

Appendix B: Final Report: Exploratory Experiments with Droplet Plumes in a Crossflow

Final Report: Exploratory experiments with droplet plumes in a cross-flow

September 1999

S. Socolofsky, A. Leos-Urbel, and E. Eric Adams

Abstract: Preliminary experiments were conducted this past summer to investigate the range of behavior of oil and gas plumes in a cross-flow. An experimental apparatus was assembled that allowed the generation of a cross-flow either by towing the source or by pumping a recirculation current. Three air diffusers were tested. A final suite of experiments investigated oil and combined gas and oil plumes with various gas:oil ratios. We observed that entrained water (which could include fine oil droplets) tended to separate (leak) from the downstream side of the plume while air bubbles and larger oil droplets tended to leave the plume on the upstream side. These observations pertain to a wide range of experimental conditions. Using a scaling analysis based on these experiments, entrained water and fine oil droplets are expected to separate from a gas plume for most small and medium sized deep-water spills anticipated for the Gulf of Mexico. In the case of a large spill, it is possible that the gas/oil plume would trap due to stratification before reaching the height for oil/gas separation.

1. Introduction

The desire to tap deep oil reserves in the oceans and the Gulf of Mexico has sparked the need to develop better predictive tools for the fate of oil released from accidental spills and blowouts in deep water (> 700 m). Of particular concern, here, is the behavior of these plumes in a current.

As summarized in our May 25 proposal, results from Hugi (1993) suggest that traditional bubble/droplet models (Yapa & Zheng 1997a,b, Liro *et al*. 1992, McDougall 1978, Asaeda & Imberger 1993) may break down when an ambient current is present. Hugi showed that dye entrained at the base of bubble columns towed along the bottom of a 3 m wide x 5.8 m long x 3 m deep tank separated out of the bubble plume and failed to reach the surface. He postulated that the bubble column never truly forms a coherent air/water plume, but merely lifts entrained water a short distance and then discharges it on the downstream side. A subsequent vortex street is formed in the lee of the bubble column, but entrained water is only displaced a short distance vertically. Deep oil-well blowouts can be accompanied by a large amount of natural gas and most integral plume models would predict that the oil, gas and entrained seawater would be transported to the surface in a coherent plume. If however, the oil and gas separate, as observed by Hugi (1993) in the case of dye, the oil may become widely distributed downstream of the gas plume.

Our proposal also summarized the results of Davidson & Pun (1999), who documented the downstream leakage of previously entrained fluid in single-phase jets in a cross-flow. The leakage is caused by turbulent eddies which dislodge fluid to the outside of the jet boundary. The ambient current then transports this fluid further away. A similar process is expected for buoyant plumes, both single and multi-phase (i.e., bubble and droplet plumes).

Based on the work of Hugi (1993) and Davidson & Pun (1999), we expected to find critical heights, dependent on the buoyancy flux, slip velocity, and ambient current speed, where a series of transitions would occur. Starting at the release point, we expected to see the following plume structure:

- Initially, the oil/gas mixture behaves as a traditional integral plume with Gaussian velocity and concentration profiles.

- Higher, the oil/gas mixture continues to behave as predicted by integral models; however, entrained fluid begins to leak from the downstream side of the plume. This occurs when the entrainment velocity is of the same order as the cross-flow velocity and detached fluid cannot be re-entrained downstream. Some fine oil droplets would be expected to be lost with this leaking fluid.
- Higher still, the oil/gas mixture no longer behaves as an integral plume. Entrained water and fine oil droplets are quickly lost downstream (or oil/gas is lost upstream) and the trajectory of the bubble column follows more closely the vector addition of the terminal rise velocity with the cross-flow velocity.
- Finally, the entrained water and oil mixture that separates from the plume transitions to behave more like a line thermal than a continuous plume. This would likely occur only in the event of high cross-flow or low bubble terminal velocities.

The focus of our investigation was to see if these regimes could be observed and, in general, to identify differences between actual plume behavior and behavior assumed in integral plume models.

To investigate these issues, we modified some of our existing facilities and, using a range of methods, conducted three sets of experiments. Section 2 discusses the experimental facility and the physical characteristics of the apparatus. Section 3 presents and discusses the images captured during the experiments. Section 4 applies scaling relationships to relate laboratory results to field-scale spills in the Gulf of Mexico. Section 5 summarizes the results of this summer's investigation, and Section 6 proposes a continued set of analyses and modeling exercises.

2. Experimental Setup

The experiments were conducted in the Parsons Laboratory at MIT using the wave flume depicted in Figure 1. The portion of flume we used measured 0.9 m deep x 0.8 m wide x 15 m long.

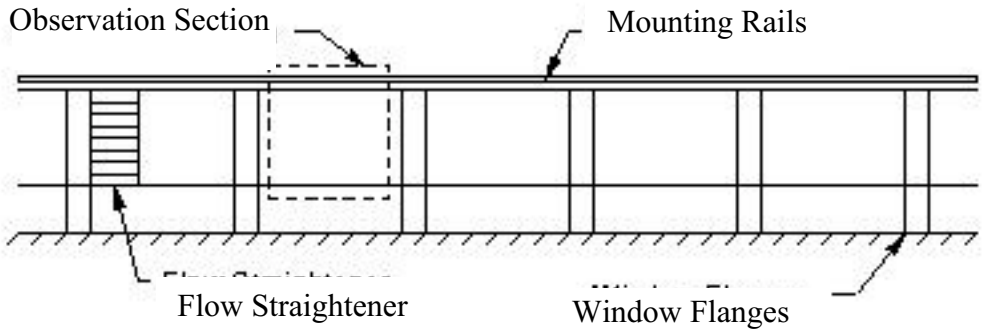

Figure 1: The experimental flume at Parsons Laboratory, MIT. Distance between successive flanges is 1.5 m.

2.1 Setting up a cross-flow

The cross-flow can be created in two different, yet comparable ways:

- **Pump:** There is a pump that recirculates the water through the flume. Its flow rate is controllable, using an upstream gate valve, and ranges from 10 to 100 L/s. These flow rates correspond to velocities of 1.4 to 14 cm/s when the tank is full.

- **Motor:** We also built a towing mechanism that can push or pull a diffuser mounted along the bottom of the tank. In this method the cross-flow is simulated using a moving frame of reference. The towing mechanism consists of a 1750 rpm variable speed motor with a 30:1 reducer gear box, attached through synchronous belts and gears to a carriage. The carriage has wheels and runs on rails, mounted on the top of the tank, enabling it to travel the length of the tank.

Cross-flow velocities generated by the pump were measured using a Sontek acoustic Doppler velocimeter (ADV). Vertical profiles were measured at a stationary point along the center-line of the tank at a range of flow rates to calibrate the pump. Profiles were also taken 0.2 m from each side to check for flow uniformity across the cross-section. To help create a uniform flow, a plastic honeycomb flow straightener was placed upstream of the test section and sealed with attached pieces of horsehair and rubber. Measured velocities varied by about +/-20% over the cross-section (i.e., the flow was not quite uniform).

The motor towing speeds were calibrated using a ruler and stopwatch method. The motor tow velocities are accurate and repeatable in the 2 cm/s - 23 cm/s range (20-90% of its maximum rpm). The motor calibration equation relating motor rpm percentage, x, to towing velocity, y, is:

$$y = 0.3\,x - 4.4 \qquad (1)$$

2.2 Characterizing the diffusers

As shown in Figure 2 , the diffusers mount to the end of a support arm attached to the carriage. The diffuser mount is attached to the towing carriage using two pieces of PVC pipe joined by a 90 degree elbow. A fluorescent dye is used as a tracer to mark the fluid entrained at the base of the plume. The air diffuser and dye line are both connected to rubber tubing running through the pipe, which is clamped to the carriage. The bubbles are discharged at 7 cm above the bottom of the tank with three different types of diffuser: a 6 cm tall limewood diffuser, a 2.5 cm tall aquarium airstone diffuser, and a 1 cm tall piece of 0.6 cm diameter vinyl tubing. In fresh water, each diffuser produces a slightly different bubble spectrum. The characteristics of the bubbles were measured using two different techniques:

- **PDPA:** The Phase Doppler Particle Analyzer (PDPA) housed at the University of Hawaii Look Laboratory was used to characterize the limewood diffuser in fresh and salty water (tap water, NaCl solutions with tap water, and seawater taken from 40 m depth). The PDPA assumes the bubbles are spherical, which is a reasonable assumption for these smaller bubbles. Rise velocities were calculated from empirical formulas relating the bubble diameter to terminal velocity in Clift *et al*. (1978).

- **Towing Technique:** The other diffusers each had bubbles too large to measure using the PDPA; hence, an alternate method was required. Hugi (1993) measured rise velocity by timing the rise of bubbles released from a rapidly towed source. Similarly, we used the towing mechanism described above and timed bubbles as they rose a distance of 63 cm, released from a diffuser towed at 22 cm/s. Bubble diameter was calculated using the same empirical formulas from Clift *et al*. (1978).

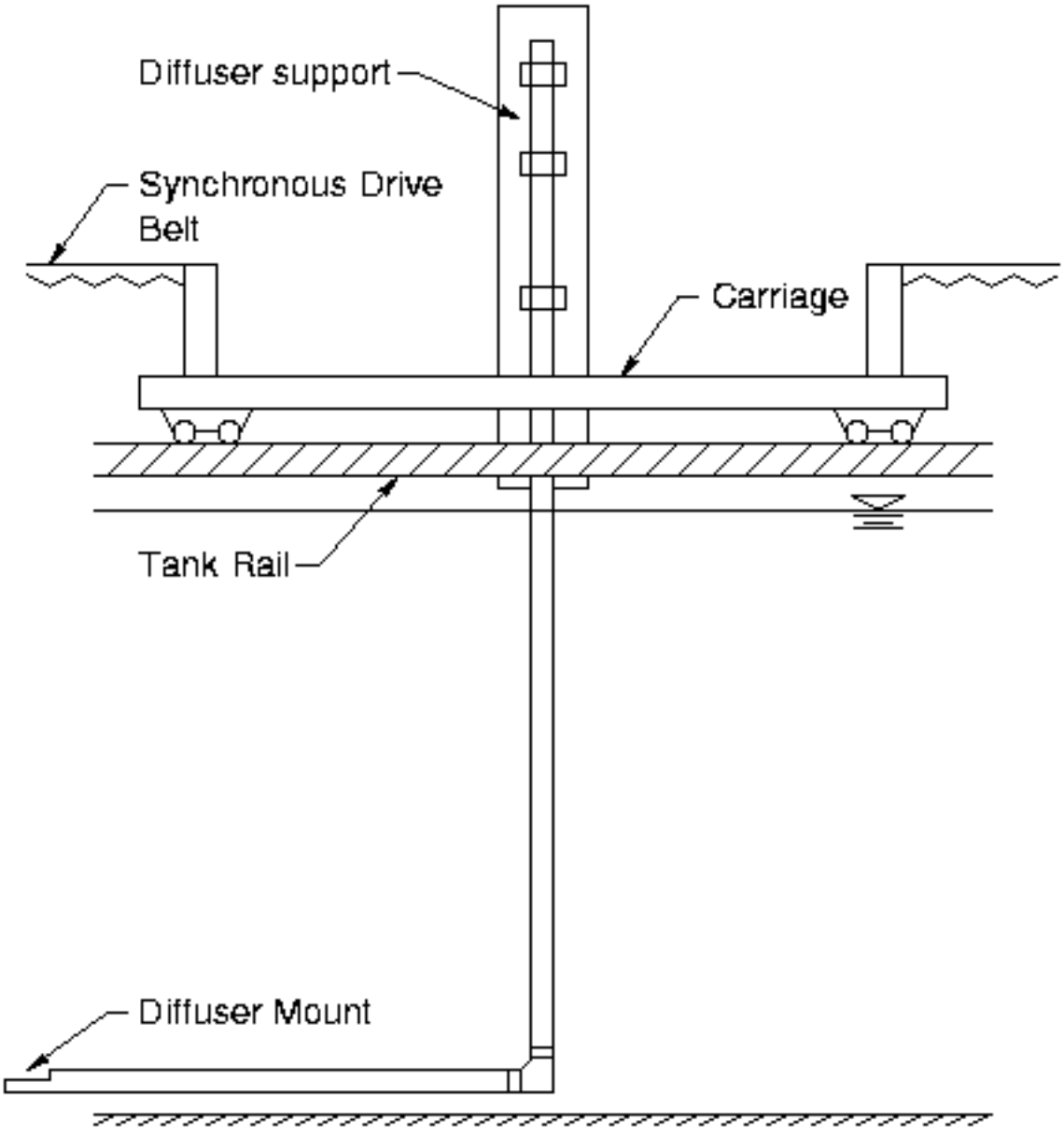

Figure 2 : The support and towing mechanism for the diffuser.

Diffuser	Average droplet diameter [mm]	Average slip velocity [cm/s]
Limewood	1.6	18
Airstone	2.4	23
Vinyl tube	2.9	26

Table 1 :Air bubble characteristics.

Table 1 summarizes the bubble characteristics for each diffuser in fresh tap water. The data in Table 1 indicate that the three diffusers produce similar bubble slip velocities. Concerning their different bubble spectra, the airstone and vinyl tube produce only "large" bubbles (~2.5 mm diameter), while the limewood diffuser produces mainly "large" bubbles, with some "small" bubbles (~0.5 mm diameter).

The small bubbles behave more like oil droplets since they have slip velocities in the range of 6.5 cm/s. We found that discharging a neutrally buoyant saltwater and alcohol solution near the diffuser head caused many more (estimated as over half the volume flux) small bubbles to form. These small bubbles have an average size of 0.5 mm and slip velocity of 6.5 cm/s. Based on our size spectrum experiments in Hawaii, the small droplet size is very stable and does not show a dependence on saltwater concentration above the threshold necessary to start producing small bubbles. In addition, once the small bubbles nucleate, they do not coalesce as they rise; hence, the small bubbles continue to rise unchanged to the surface.

In addition to pure air experiments, we also ran experiments with just crude oil, with just alcohol, with air/oil mixtures by volume of 1:1 and 10:1, and with mixtures of alcohol and gas. These experiments varied the oil, alcohol, and gas flow rates and the cross-flow velocity. The droplet characteristics of the oil diffusers were not precisely determined; however, the majority of oil droplets by volume had slip velocities in the approximate range of 4 to 8 cm/s. The oil droplet spectrum had a long tail of smaller droplets trailing down to very fine droplets rising in The 1 mm/s and lower velocity range. Alcohol was used to simulate the finest oil droplets since it has an effective slip velocity of 0. These different experiments with various bubble sizes could represent a range of natural gas bubble sizes (with or without hydrates), a range of oil

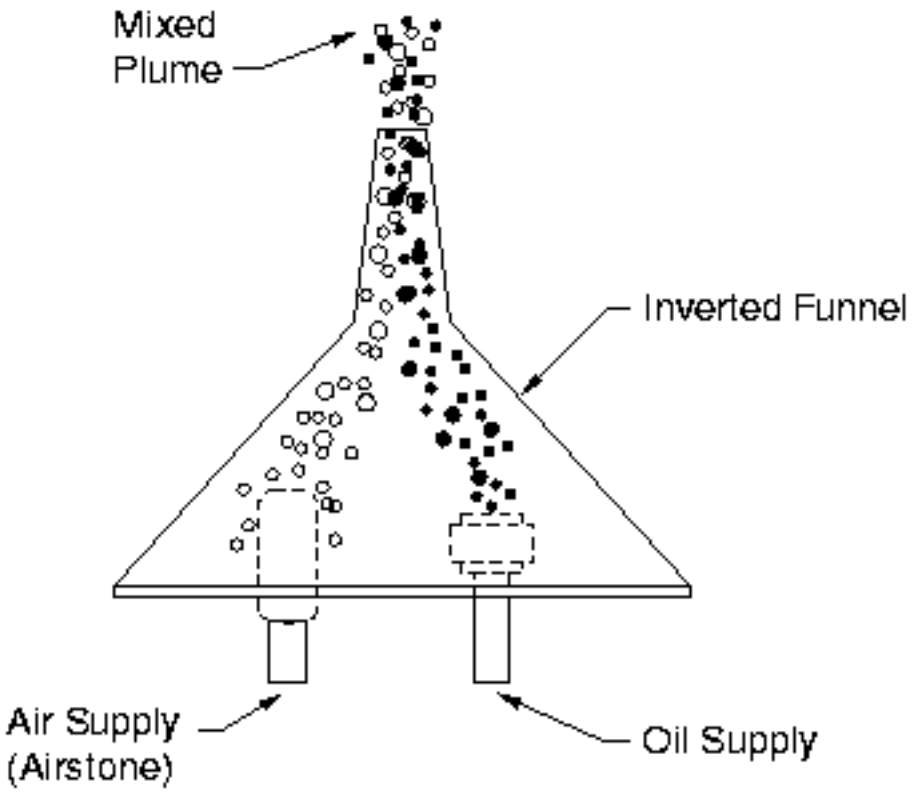

Figure 3: Inverted funnel.

droplet sizes, or a combination. To ensure that the oil and gas and alcohol and gas where equally distributed in the plume, an inverted funnel was used as depicted in Figure 3.

3. Experimental Results

3.1 Gas experiments with the recirculation pump

An initial set of experiments was conducted using air only and the recirculation cross-flow generated by the pump. Images captured during these experiments are summarized in Thumbnails 1 and were presented by Dr. Adams at the Houston Conference in July. The conditions of each experiment were as shown in Table 2. The funnel diffuser refers to dense saltwater experiments designed to show the difference between single- and multi-phase plumes.

Thumbnails 1: Pump experiments with gas, dye and dense water

Experiment A1

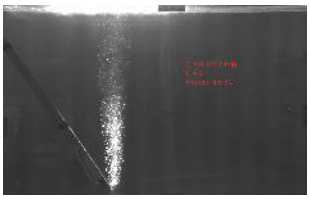

Experiment A2

Experiment A3

Experiment A4

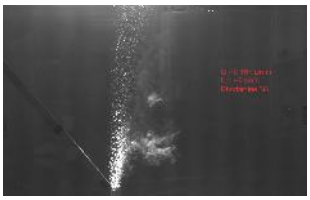

Experiment A5

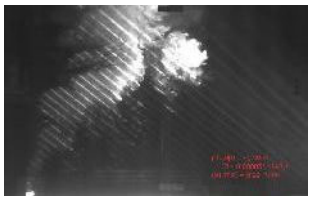

Experiment A6

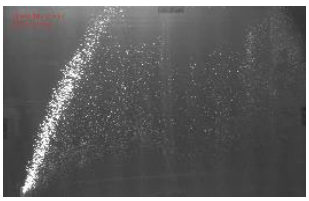

Experiment A7

Experiment A8

Experiment A9

Table 2 Parameter values for shake-down experiments

Experiment	Diffuser	Cross-flow velocity [cm/s]	Gas flow rate at STP [mL/min]	Saltwater flow rate [mL/min]	Dye Injected ? [yes/no]
A1	Limewood	0	167	0	no
A2	Limewood	0	167	0	yes
A3	Funnel	0	0	860	yes
A4	Limewood	2	167	0	no
A5	Limewood	2	167	0	yes
A6	Funnel	2	0	860	yes
A7	Limewood	10	167	0	no
A8	Limewood	10	167	0	yes
A9	Limewood	10	167	0	yes

In the Thumbnails, the photos for the funnel experiments are shown up-side-down to have the same orientation as the bubble experiments with the same absolute buoyancy. The buoyancy flux for the dense water and air bubble experiments was the same, even though the volume flux was quite different. The buoyancy flux should control the behavior of these plumes.

The experiments in column 1 of Thumbnails 1 were with air only, column 2 had air and injected dye, and column 3 presents the dense water experiments having saltwater and dye. This first set of experiments demonstrates the following behavior for bubble plumes in a cross-flow:

- The effect of the bubbles is to raise entrained water (marked by the dye) in the bubble column (see Experiments A2, A5, and A8).

- Even small currents (second row of Thumbnails 1: cross-flow velocity is 2 cm/s) cause bubbles to separate from dye (plume) at some point in their trajectory.

- Close examination of row 2 shows small bubbles fractionate/sort from the large bubbles, creating a bubble column with large bubbles upstream and small bubbles downstream and gradual transition in between.

- The above two effects are magnified for larger currents, meaning the effects occur at lower elevations (see row 3: cross-flow velocity is 10 cm/s).

- The trajectory of the bubble experiments (columns 1 and 2) is much different from the trajectory of the single-phase experiments (column 3). The bubble columns trace a slanted line as they rise, whereas, the single-phase plumes are bent over in a parabolic shape.

- A traditional integral plume model would simulate column 3, but not columns 1, and 2.

Based on the various dye injection methods tested during this set of experiments, we decided it was important to inject the dye upstream of the plume to insure that it was entrained and not lost right away on the downstream side. A range of pump flow rates was also tested to help design the towing mechanism. Small bubbles were observed to leave the main bubble plume beginning at a cross-flow velocity as low as 2 cm/s. From these experiments the towing mechanism described above was designed and built.

3.2 Gas experiments with the towing mechanism

The remaining experiments were conducted using the towing mechanism, the first set of which were designed to observe the fate of dye tracer entrained at the base of pure gas plumes, analogous to the experiments presented in the previous section in column 2 of Thumbnails 1. The images from this set of tests are cataloged in Thumbnails 2 and are summarized in Table 3.

Experiments B1 to B8 were with a 6 mm diameter piece of vinyl tubing; Experiment B9 was with dye only; and, Experiments B10 and B11 were with an aquarium airstone. These experiments confirm the observations from the earlier pumped experiments and confirm our expectation for plume development presented in Section 1. Specifically, the following set of observations are made:

- To varying degrees, again, dye and bubbles tend to separate from each other for all cases.

- There is little apparent effect of bubble size on the trajectory of the separated dye (compare Experiments B11 to B2 and B10 to B1).

Thumbnails 2: Towed experiments with gas and dye

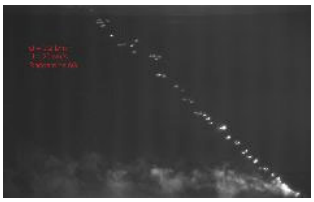

Experiment B1

Experiment B2

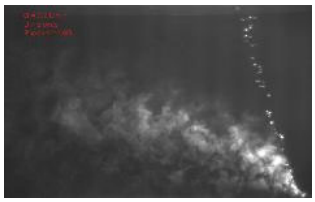

Experiment B3

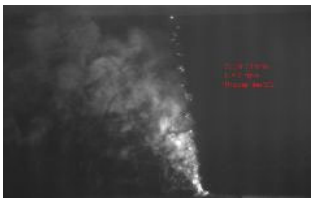

Experiment B4

Experiment B5

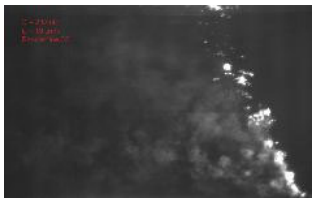

Experiment B6

Experiment B7

Experiment B8

Experiment B9

Experiment B10

Experiment B11

Table 3 Parameter values for air experiments

Experiment	Diffuser	Cross-flow velocity [cm/s]	Gas flow rate at STP [mL/min]
B1	Vinyl Tube	20	200
B2	Vinyl Tube	10	200
B3	Vinyl Tube	5	200
B4	Vinyl Tube	2	200
B5	Vinyl Tube	20	2000
B6	Vinyl Tube	10	2000
B7	Vinyl Tube	5	2000
B8	Vinyl Tube	2	2000
B9	Dye only	10	0
B10	Airstone	20	200
B11	Airstone	10	200

- There is a strong effect of the cross-flow with higher cross-flow leading to greater separation (compare, successively, Experiments B1 through B4 and B5 through B8).

- The effect of the bubbles is to raise the dye centerline, as was seen by Hugi (1993), and to increase the thickness of the shed dye plume. Both effects increase with increasing bubble flow (compare Experiments B9, B2, and B6).

- One factor causing the thickness of the shed dye plume to increase is that some shed dye is re-entrained by the rising bubble column and discharged again later at a higher elevation. This effect is strongest in weakest currents (because the dye cannot stray far) and in strongest air flow rates (because entrainment is strongest).

- Conclusions: There are two factors causing separation (material leaving the coherent bubble column):

    1 Fractionation due to differential rise velocities of bubbles.

    2 Leakage caused by shed turbulent eddies.

    And there are two competing forces effecting material once it has separated:

a. Currents which cause further separation.

b. Entrainment which causes less separation by promoting material being returned to the bubble column.

3.3 Oil plume experiments

The final experiments involved oil, gas, and alcohol in various combinations and were conducted with the towing mechanism. These experiments are summarized in Thumbnails 3 and are listed in Table 4.

Table 4 Parameter values for oil experiment

Experiment	Cross-flow velocity [cm/s]	Gas flow rate at STP [mL/min]	Oil flow rate [mL/min]	Alcohol flow rate [mL/min]	Dye injected ? [yes/no]
C1	5	250	250	0	no
C2	2	250	250	0	no
C3	10	250	250	0	no
C4	5	600	600	0	no
C5	10	600	600	0	no
C6	5	2500	250	0	no
C7	10	2500	250	0	no
C8	5	1000	1000	0	no
C9	10	1000	1000	0	no
C10	2	600	600	0	yes
C11	5	0	250	0	yes
C12	5	250	250	0	yes
C13	5	600	600	0	yes
C14	5	0	600	0	yes
C15	10	600	600	0	yes
C16	5	250	0	150	yes
C17	5	600	0	360	yes
C18	10	600	0	360	yes
C19	5	0	0	150	yes
C20	10	0	0	360	yes
C21	10	0	0	150	yes

Thumbnails 3: Pump experiments with gas, oil, and alcohol

Experiment C1

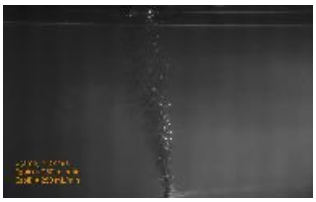

Experiment C2

Experiment C3

Experiment C4

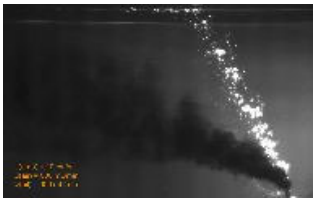

Experiment C5

Experiment C6

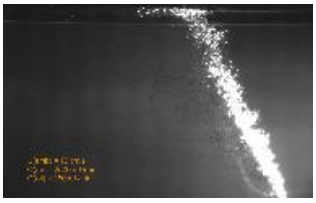

Experiment C7

Experiment C8

Experiment C9

Experiment C10

Experiment C11

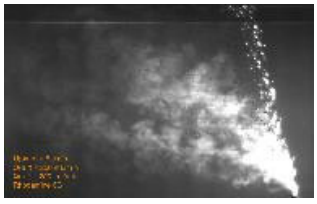

Experiment C12

Thumbnails 3: Pump experiments with gas, oil, and alcohol

Experiment C13

Experiment C14

Experiment C15

Experiment C16

Experiment C17

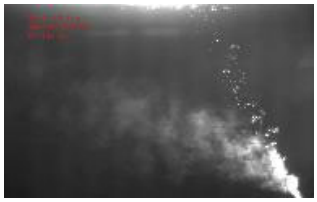

Experiment C18

Experiment C19

Experiment C20

Experiment C21

Three oil flow rates were selected (250, 600, and 1000 mL/min) and four air flow rates were selected (250, 600, 1000, and 2500 mL/min). These flow rates were combined primarily in gas:oil ratios of 1:1 (which corresponds to a gas:oil ratio (GOR) of 100 at 1000 m depth in the field), with two experiments (numbers C6 and C7) having a gas:oil ratio of 10:1 (GOR of 1000 in the field, admittedly a high number). Pure isopropyl alcohol was also used in some experiments to simulate the influence of very small oil droplets on the characteristics of the plume (since the equivalent "slip velocity" of alcohol is 0). The density of oil used was 0.87 g/cc; the density of alcohol was 0.78 g/cc. So that the buoyancy flux of alcohol would be the same as that for oil, two alcohol flow rates were selected (150 and 360 mL/min) which correspond to the two lowest oil flow rates (250 and 600 mL/min, respectively). Dye was added to some of the experiments to aid visualization.

This final set of experiments provides the following set of observations:

- Dye added to a pure oil release (Experiments C11, & C14) stayed with the oil droplets much better than dye added to a pure gas discharge (Experiments in Series A & B in Sections 3.1 & 3.2) implying that a pure oil discharge is much more of a "plume" than a pure gas discharge. Although we couldn't simulate a hydrate discharge, we can expect behavior similar to oil discharge because similar density differences and rise velocities.

- Nevertheless, the slip velocity of the oil droplets does affect the plume. As illustration, even though they have the same buoyancy flux, the pure alcohol and pure oil plumes show a significant difference in trajectory, apparently because of the oil droplet slip velocity (compare Experiments C19 and C11).

- All experiments involving both oil and gas show at least some fractionation/separation of the two phases. This is similar to the previous discussion of the Series~A and~B experiments with pure gas, and is not surprising since the buoyancy of the gas exceeds that of the oil by an order of magnitude in most experiments (those with gas:oil ratio of 1) and two orders of magnitude in others (those with gas:oil ratio of 10).

- Dye added with the oil/gas plumes to mark the entrained water more closely follows the oil than the gas, but trails the oil a little bit (leaks out of the oil plume), especially for

lower buoyancy fluxes of oil. Thus, Experiments C15 and C5 (600 mL/min) are similar, but Experiments C12 and C1 (250 mL/min) show some difference.

- Separation of oil and gas increases with increasing current speed. Thus, for an average oil and gas flow rate of 600 mL/min, Experiment C10 (current was 2 cm/s) showed some separation; Experiment C4 (current was 5 cm/s) showed more separation; Experiment C5 (current was 10 cm/s) showed strong separation. This effect, however, is not as strong as seen previously in Section 3.2 with gas and dye because of the positive slip velocity of the oil droplets.

- The separation of oil and gas decreases with increasing buoyancy flux. Experiments C2, C1, and C3 had oil and gas flow rates of 250 mL/min and show more effect than Experiments C8 and C9, which had oil and gas flow rates of 1000 mL/min.

- Increasing the GOR (10 in the lab corresponding to 1000 in the field) pushes oil up further, due to larger entrainment, resulting in less separation of oil and gas (Compare Experiments C7 to C3 and C6 to C2).

- A traditional integral plume model would simulate the pure oil plumes in the same way as pure alcohol plumes, thus missing some of the effects of slip velocity, and would not simulate the separation observed between oil and gas or between alcohol and gas in the multi-phase experiments.

4. Application to field conditions

To apply the results from the laboratory to the field-scale conditions, proper scaling relationships must be identified. As explained in the May 25 proposal, the important parameters determining the plume characteristics are the buoyancy flux, $B = Qo\ g\ dp/p$ (where Qo is the volume flow rate of the buoyancy source (e.g., oil), g is the acceleration of gravity, dp is the density difference between the buoyant fluid and the ambient fluid, and p is the ambient density), the droplet terminal rise velocity, us, the ambient current speed, ua, the stratification strength, N= sqrt[$(g / p)\ (dp / dz)$], and the elevation of interest, z, above the source. For the experiments

conducted this summer, we ignored the effect of stratification to focus on the effect of the current.

Comparing the laboratory conditions to the field, we expect that *us* and *ua* in the laboratory would be the same order of magnitude in the field (of order 10 cm/s for both). Hence, B and z are the main parameters that need to be scaled from the laboratory conditions to the field conditions. In non-dimensional terms, we have:

$$\left.\frac{u_s}{\left(\frac{B}{z}\right)^{1/3}}\right|_{\text{lab}} = \left.\frac{u_s}{\left(\frac{B}{z}\right)^{1/3}}\right|_{\text{field}} \tag{2}$$

$$\left.\frac{u_a}{\left(\frac{B}{z}\right)^{1/3}}\right|_{\text{lab}} = \left.\frac{u_a}{\left(\frac{B}{z}\right)^{1/3}}\right|_{\text{field}} \tag{3}$$

Which give us

$$\left(B/z\right)_{\text{lab}} = \left(B/z\right)_{\text{field}} \tag{4}$$

if *ua* and *us* are the same. Using Equation 4 we can calculate the size of field-scale plumes that correspond to the experiments presented above.

For this analysis, we have defined small, medium and large field-scale oil spills, each discharged at a depth of 1000 m. First, is a small spill containing just oil, with an oil flow rate of 0.001 cubic meters per second (cms). Second, is a small spill containing oil and gas and assuming that all of the gas is in hydrates. This spill has a GOR of 100 and an oil flow rate of 0.001 cms. Third, is another small spill of oil and gas, this time assuming that none of the gas converts to hydrates (GOR remains 100; oil flow rate is still 0.001 cms). The fourth spill is a medium spill of oil and gas without hydrates that has a GOR of 100 and an oil flow rate of 0.01 cms. The final spill is a large spill of oil and gas that has a GOR of 100 and an oil flow rate of 0.1 cms. Table 5 presents the physical characteristics of these five spills. The entries in Table 5 were calculated assuming the density of seawater was p = 1.034 g/cc, the density of oil was the same as for hydrates and was $po = ph$ = 0.9 g/cc, and the stratification was typical of the Gulf of Mexico with N = 0.002/s, appropriate for a release depth of H = 1000 m (data provided by Chevron, personal communication). The trap heights in Table 5 were calculated with the empirical equation:

Table 5 Physical characteristics of the field-scale oil spills. The trap-height calculation assumes a standard stratification of 0.006 s^{-1}.

Spill size	Oil flow rate [cms]	Hydrate flow rate [cms]	STP Gas flow rate [cms]	Buoyancy flux [m^4/s^3]	Trap height [m]
Small	0.001	0	0	0.0013	55
Small	0.001	0.001	0	0.0025	64
small	0.001	0	0.001	0.0098	89
Medium	0.01	0	0.01	0.098	160
Large	0.1	0	0.1	0.98	280

$$h_T = 2.7 \frac{B^{1/4}}{N^{3/4}} \qquad (5)$$

The laboratory experiments from Section 3.3 are compared to the field-scale spills in Table 6.Table 6 gives the percent of the total depth in the laboratory that would be realized in the field before the plume is expected to trap. For these calculations, the density of water was taken as p = 0.996 g/cc and the total depth was $H(lab)$ = 0.7 m. From Equations 4 and 5 the percent of flume applicable in the field is:

$$\text{Percent} = \frac{B_{\text{lab}}}{B_{\text{field}}} \frac{h_T}{H_{\text{lab}}} 100\% = \frac{2.7 B_{\text{lab}} 100}{0.7 N^{3/4} B_{\text{field}}^{3/4}} = 41000 \frac{B_{\text{lab}}}{B_{\text{field}}^{3/4}} \qquad (6)$$

If there were no stratification in the field, or only very weak stratification, the full laboratory depth would be realized.

Based on the data in Table 6, field plumes scaled down to our laboratory conditions would generally trap in the low to middle portion of our tank, except for the large spill with oil and gas which would trap near the spill source. Because most of the oil/gas separation observed in our experiments occurs throughout the water column, the observations detailed in Section 3 for the lab should also be applicable to the small and medium sized spills in the field with stratification (or to all spills in the field without stratification).

Table 6 Application of laboratory tests to the field-scale. The number in the columns to the right indicate the percent of the total laboratory depth that would be realized in the field before the plume is expected to trap.

Exp. IDs	Gas Flux [mL/min]	Oil Flux [mL/min]	Alcohol Flux [mL/min]	B_{lab} x10^{-6} [m^4/s^3]	Small oil	Small oil + hydrate	Small oil + gas	Medium oil + gas	Large oil + gas
C11	0	250	0	3.9	23	14	--	--	--
C14	0	600	0	9.5	27	34	--	--	--
C19 C21	0	0	150	5.3	32	18	--	--	--
C20	0	0	360	13	78	46	--	--	--
C1 C2 C3 C12	250	250	0	45	--	--	50	9	2
C4 C5 C10 C13 C15	600	600	0	110	--	--	> 100	23	5
C8 C9	1000	1000	0	180	--	--	> 100	36	7
C16	250	0	150	46	--	--	52	9	2
C17 C18	600	0	360	110	--	--	> 100	23	5

It is hard to tell what the effect of a current would be on the largest oil and gas spills with stratification because they would trap very near the origin. However, further dimensional analysis suggests the effect of a current diminishes with increasing spill size. For a given slip velocity, the elevation, h_c , at which a current significantly affects plume dynamics should be given by:

$$h_c \sim \frac{B}{u_a^3} \tag{7}$$

The importance of a cross-flow, relative to ambient stratification, is given by the ratio hT/hc or, combining Equations 5 and 7:

$$\text{Importance of cross - flow} \sim \frac{u_a^3}{(BN)^{3/4}} \tag{8}$$

Large spills with oil and gas have larger B and would more likely trap before the effect of a current came into play.

5. Summary

The laboratory experiments conducted this summer indicated a significant difference between the behavior of single-phase and two-phase plumes in a cross-flow. These differences are important since traditional integral plume models ignore some of the physical differences between two-phase and single-phase plumes. The important differences described above can be summarized as follows:

- The trajectories of pure oil, and pure gas plumes are much different from single-phase plumes having the same buoyancy flux because of the effect of the slip velocity of the oil droplets and gas bubbles.

- When there is a distribution of bubble or droplet sizes, rising bubbles and droplets are fractionated by the current, causing large droplets to lead out front with a gradual transition to smaller droplets in the lee of the plume. This was observed even at very low cross-flow velocities (2 cm/s and greater).

- Injected dye (which marks entrained ambient water and could also represent fine oil droplets) is observed to leak from the downstream side of a gas or oil and gas plume, even at low current speeds, as observed by Davidson & Pun (1999) for single-phase plumes. Hence, the entrained water and rising bubbles become more independent of each other with increasing current speed and with increasing height above the release point.

- When ambient water, oil droplets and air bubbles become separated, the situation can no longer be modeled with a traditional integral plume model because the different constituents maintain different trajectories. These effects are more extreme for gas/oil/water plumes than for oil/water plumes or for oil/hydrate/water plumes.

- The effects above increase with increasing current speed and droplet/bubble slip velocity and with decreasing flow rate.

The application of the laboratory tests to the field-scale spills is discussed in Section 4. Based on scaling relationships, the effects outlined in the above list would impact small and medium sized spills at 1000 m depth in the Gulf of Mexico, but ambient stratification might cause large spills to trap before current effects become dominant. We conclude that the current effects outlined above must be addressed to accurately predict the fate of spilled oil, especially that originating from small and medium sized oil-well blowouts.

6 Proposal for further investigation

As a next step in understanding the effects of a cross-flow on two-phase plumes, we propose to create a simple numerical model/algorithm that includes criteria for when and where gas bubbles and entrained water and oil would separate and that tracks the individual plumes after separation. The model would not include the complex effects of chemistry, mass transfer or stratification. However, upon calibration, the algorithm could be incorporated into more complex integral models (which include chemistry, mass transfer and stratification) such as Yapa & Zheng (1997a,b). Additional laboratory experiments would be conducted, if necessary, to complement the data basis for model calibration. Based on the analysis of Section 4, we would focus on larger

laboratory flow rates to allow experiments to apply to larger field-scale oil and gas spills. Also, a few laboratory experiments would be conducted with stratification and a current to allow validation of the more complete models. These additional tests could be conducted using our towing mechanism, installing two bulkheads in our wave flume, and making use of our two tank filling system (similar to what we are doing for our stratified stagnant water tests) to effect a linear stratification.

Appendix I. References

Asaeda, T. & Imberger, J. (1993) "Structure of bubble plumes in linearly stratified environments", *Journal of Fluid Mechanics* **249** , 35-57.

Clift, R., Grace, J. R., & Weber, M. E. (1978) *Bubbles, Drops, and Particles* , Academics Press, New York, New York.

Davidson, M. J. & Pun, K. L. (1999), "Weakly advected jets in a cross-flow", *ASCE Journal of Hydraulic Engineering* **125** (1), 47-58.

Hugi, C. (1993), Modelluntersuchungen von Blasenstrahlen fuer die Seebelueftung, Ph.D. Thesis, Inst. f. Hydromechanik u. Wasserwirtschaft, ETH, Zurich.

Liro, C. R., Adams, E. E. & Herzog, H. J. (1992), "Modeling the release of CO2 in the deep ocean", *Energy Conservation Management* **33** (5-8), 667-674.

McDougall, T. J. (1978), "Bubble plumes in stratified environments", *Journal of Fluid Mechanics* **85** (4), 655-672.

Reingold, L. S. (1994), An experimental comparison of bubble and sediment plumes in stratified environments, Master's thesis, Massachusetts Institute of Technology, Department of Civil and Environmental Engineering.

Yapa, P. D. & Zheng, L. (1997*a*), "Simulation of oil spills from underwater accidents I: Model development", *Journal of Hydraulic Research* **35** (5), 673-687.

Yapa, P. D. & Zheng, L. (1997*b*), "Simulation of oil spills from underwater accidents II: Model verification", *Journal of Hydraulic Research* **35** (5), 688-697.

Appendix C: Report Summary: CORMIX 3.2 Analysis of Droplet Plumes in a Crossflow

Report Summary: CORMIX 3.2 Analysis of droplet plumes in a cross-flow

October 1999
S. Socolofsky, A. Leos-Urbel, and E. Eric Adams

Contents

Abstract: Images from the summer cross-flow experiments were compared to predictions using the Cornell Mixing Zone Model (CORMIX) Version 3.2. The CORMIX model uses a variety of control programs and a large number of simulations modules to predict the flow from a wide range of discharge and ambient conditions. The results for the center-line plume prediction are plotted together with the images captured from the cross-flow experiments to provide a comparison.

1. Introduction

The desire to tap deep oil reserves in the oceans and the Gulf of Mexico has sparked the need to develop better predictive tools for the fate of oil released from accidental spills and blowouts in deep water (> 700 m). Of particular concern, here, is the behavior of these plumes in a current.

Our previous report *Draft Final Report: Exploratory experiments with droplet plumes in a cross-flow* summarized the important physical properties controlling the fate of oil in a plume in a cross-flow. This report summarizes our comparison of the experiments to predictions from a commonly used jet and plume model, the Cornell Mixing Zone Model (CORMIX) Version 3.2.

CORMIX is an accepted standard for the determination of mixing zone properties for water quality permit application for a wide range of discharge types and ambient conditions. At the model's heart

is a toolbox of simulation models based on buoyant jet similarity and integral models, ambient diffusion theory, stratified flow theory, and simple dimensional analysis. The basic procedure is for CORMIX to classify the flow based on dimensional analysis and then select the appropriate simulation modules for the given flow classification. Using these techniques the plume is modeled from the near-field of the injector to the far-field of the receiving water body.

In the analysis presented here, CORMIX 3.2 was run for each of the experiments in Set B and Set C from the previous report. The center-line prediction from CORMIX is then plotted on the images captured from the experiments. The Analysis section interprets the results of the simulations and the Summary presents the findings.

2. CORMIX 3.2 Simulations

As already mentioned, CORMIX 3.2 combines a number of different simulation methods to prediction plume properties. Some of the limitations of CORMIX methods impact the formulation of the simulations.

First, CORMIX was designed to predict the fate of single-phase contaminants. For stability reasons, and to meet the requirements of its methods, CORMIX limits the density of injected fluid to be between 0.8 and 1.2 g/cc. To meet this requirement, the injected fluid density for each simulation was assumed to be 0.8 g/cc (except for pure oil plumes, where the actual oil density of 0.87 g/cc could be used). Because air, alcohol, and air/oil mixtures have effective densities less than 0.8 g/cc, higher flow rates are used in CORMIX than were actually injected. In all cases, the buoyancy flux was kept constant between simulations and experiments.

Second, CORMIX is able to simulate both jet- and plume-like behavior. Because our air diffusers are porous materials (with unknown port surface areas), the port diameter was set to 0.02 m, which resulted in negligible momentum effects at the injector. This agrees well with the observations that a significant bubble jet did not form.

2. CORMIX 3.2 Results for Air Experiments

The air-only experiments were conducted using the towing mechanism, designed to observe the fate of dye tracer entrained at the base of pure gas plumes. The images from this set of tests are cataloged in Thumbnails 1 and are summarized in Table 1.

Table 1

Experiment	Diffuser	Cross-flow velocity [cm/s]	Gas flow rate at STP [mL/min]
B1	Vinyl Tube	20	200
B2	Vinyl Tube	10	200
B3	Vinyl Tube	5	200

B4	Vinyl Tube	2	200
B5	Vinyl Tube	20	2000
B6	Vinyl Tube	10	2000
B7	Vinyl Tube	5	2000
B8	Vinyl Tube	2	2000
B9	Dye only	10	0
B10	Airstone	20	200
B11	Airstone	10	200

Experiments B1 to B8 were with a 6 mm diameter piece of vinyl tubing; Experiment B9 was with dye only; and, Experiments B10 and B11 were with an aquarium airstone. Because Experiment B9 injected only dye, CORMIX was not run for comparison.

These experiments suggest the following observations:

- CORMIX follows air for Experiments 4, 6, 7, and 8.

- CORMIX over-predicts the center-line elevation for the bubble plume in low currents. In this case the bubble rise velocity is of the same order as the plume rise velocity, making the bubble column plume-like; however, as fluid leaks from the downwind side of the bubble column, the plume rise velocity is diminished from the single-phase case, causing the bubble plume to lie below the CORMIX prediction.

- CORMIX under-predicts the center-line elevation for the bubble plume in high currents. In this case the air bubble slip velocity is much greater than the predicted plume rise velocity, and the bubble column is not plume-like.

- Dye does not follow air completely in any experiment.

- CORMIX follows dye for Experiments 1 and 10.

3. CORMIX 3.2 Results for Oil Experiments

The next set of experiments involved oil, gas, and alcohol in various combinations and were conducted with the towing mechanism. These experiments are summarized in Thumbnails 2 and are listed in Table 2.

Table 2

Experiment	Cross-flow velocity [cm/s]	Gas flow rate at STP [mL/min]	Oil flow rate [mL/min]	Alcohol flow rate [mL/min]	Dye injected ? [yes/no]
C1	5	250	250	0	no
C2	2	250	250	0	no
C3	10	250	250	0	no
C4	5	600	600	0	no
C5	10	600	600	0	no
C6	5	2500	250	0	no
C7	10	2500	250	0	no
C8	5	1000	1000	0	no
C9	10	1000	1000	0	no
C10	2	600	600	0	yes
C11	5	0	250	0	yes
C12	5	250	250	0	yes
C13	5	600	600	0	yes
C14	5	0	600	0	yes
C15	10	600	600	0	yes
C16	5	250	0	150	yes
C17	5	600	0	360	yes
C18	10	600	0	360	yes
C19	5	0	0	150	yes
C20	10	0	0	360	yes

Three oil flow rates were selected (250, 600, and 1000 mL/min) and four air flow rates were selected (250, 600, 1000, and 2500 mL/min). These flow rates were combined primarily in gas:oil ratios of 1:1 (which corresponds to a gas:oil ratio (GOR) of 100 at 1000 m depth in the field), with two experiments (numbers C6 and C7) having a gas:oil ratio of 10:1 (GOR of 1000 in the field, admittedly a high number). Pure isopropyl alcohol was also used in some experiments to simulate the influence of very small oil droplets on the characteristics of the plume (since the equivalent "slip velocity" of alcohol is 0). The density of oil used was 0.87 g/cc; the density of alcohol was 0.78 g/cc. So that the buoyancy flux of alcohol would be the same as that for oil, two alcohol flow rates

were selected (150 and 360 mL/min) which correspond to the two lowest oil flow rates (250 and 600 mL/min, respectively). Dye was added to some of the experiments to aid visualization.

These experiments suggest the following observations:

- CORMIX generally predicts the trajectory of the oil and the alcohol for each experiment involving oil or alcohol, even in the presence of air bubbles.

- The oil and alcohol do not always follow the air (exceptions are Experiments 2 , 6, 7, 8, 13, and 17.

- CORMIX tends to over-predict the height of the oil and alcohol plume center-lines. This can be accounted for by two reasons:

    1. The diffuser support arm rocks up and down, and an error of a few centimeters for the injection height can account for the offset in the center-line predictions.

    2. The slip velocity can also account for the difference, as indicated in the previous section for air bubbles in weak cross flows. in the single phase case, the plume effect helps organize the plume and carry the entrained fluid vertically upward. In the two-phase case, entrained water is seen leaving the plume on the downwind side, decreasing the plume effect, and reducing the upward velocity of plume fluid; hence, the two phase plume would plot below the single phase plume when the plume fluid rise velocity is of the same order as the bubble slip velocity.

4. Analysis

As discussed in our previous report, the important scaling parameters controlling these plumes are U, the ambient current speed, B, the plume buoyancy flux, and z, the elevation coordinate, taken as the total water depth, H for the analysis in this section. The droplet slip velocity is also an important parameter, but is neglected in this analysis because CORMIX does not include the slip velocity in its computation.

Combining the important parameters in a non-dimensional way gives us:

$$P = U/(B/H)^{(1/3)} \qquad (1)$$

From the experiments presented in the previous two sections, critical values for P that corresponds to whether CORMIX can predict the trajectory of plume components (whether an integral model is appropriate) can be calculated. The following critical regions were identified:

- For P <= 1.0 +/- 0.2 CORMIX predicts a trajectory that follows the air bubbles.

- For P between 1.0 and 5.0, CORMIX predicts a trajectory that differs from the bubbles, but falls between the bubbles and the injected dye tracer.

- For P > 5.0, CORMIX predicts a trajectory that follows the injected dye tracer, lagging far behind the air bubble front.

- For all *P* simulated, CORMIX predicts a trajectory that follows the oil and the alcohol, both when air is present and when it is absent. CORMIX is designed to handle the alcohol plume case in the absence of air, so this indicates that for our experimental facility, the slip velocity of the oil droplets appears to be negligible for simulating the trajectory of oil in oil and air/oil plumes.

5. Summary

From simulations using CORMIX 3.2, three primary observations were made:

1. CORMIX can predict the trajectory of air-bubble plumes for $P <= 1.0 +/- 0.2$.

2. CORMIX predicts well the trajectory of oil and alcohol plumes for all of the experiments conducted.

3. The slip velocity can account for plume trajectories that fall above the CORMIX predictions in high currents, and below the CORMIX predictions in low current.

Thumbnails 1: Towed experiments with gas and dye

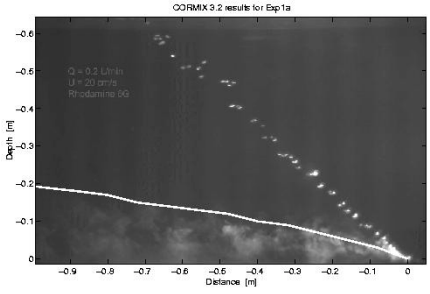

Experiment B1

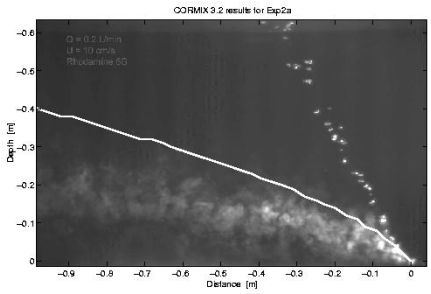

Experiment B2

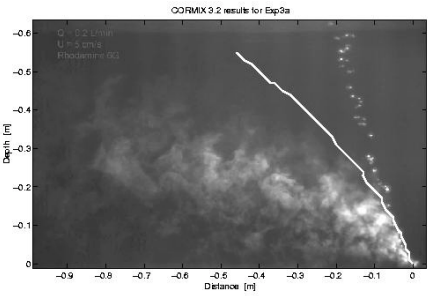

Experiment B3

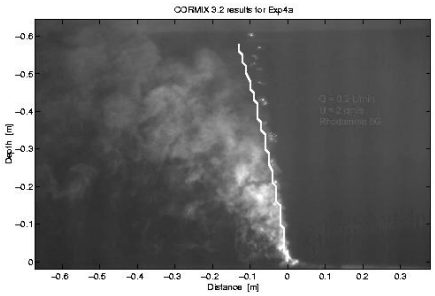

Experiment B4

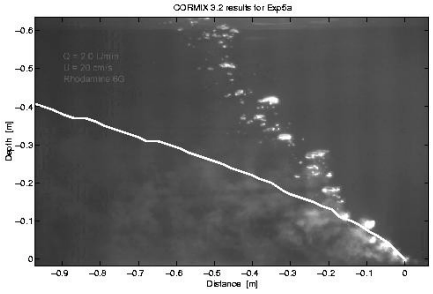

Experiment B5

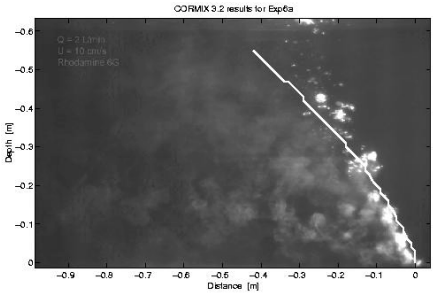

Experiment B6

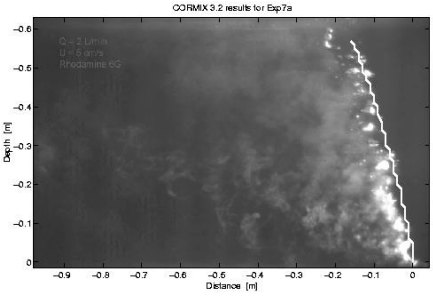

Experiment B7

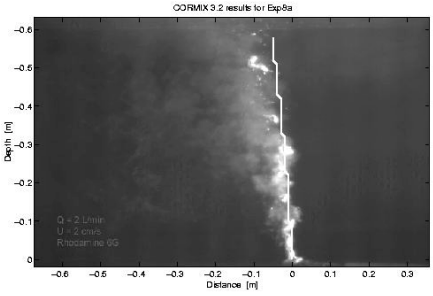

Experiment B8

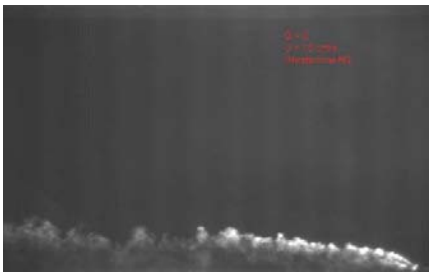

Experiment B9

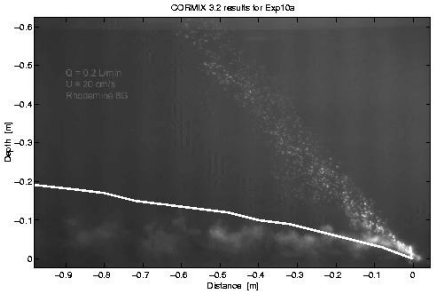

Experiment B10

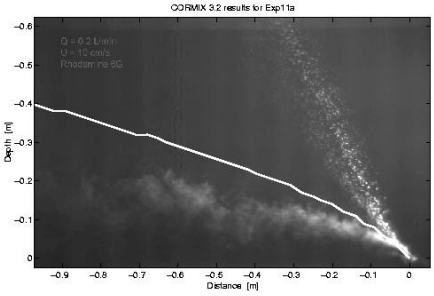

Experiment B11

Thumbnails 2: Experiments with gas, oil, and alcohol

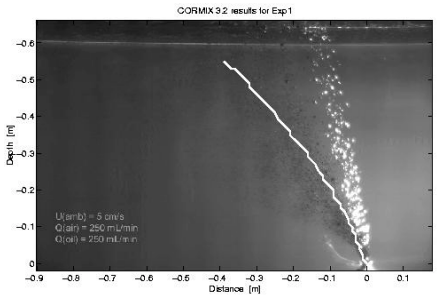

Experiment C1

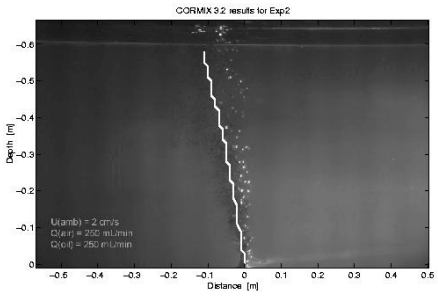

Experiment C2

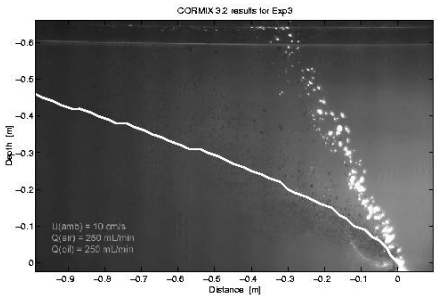

Experiment C3

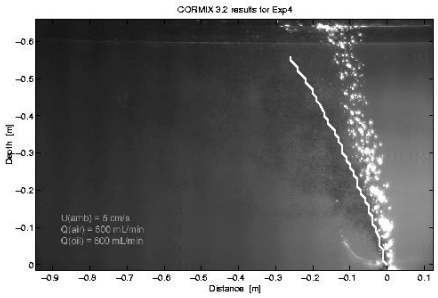

Experiment C4

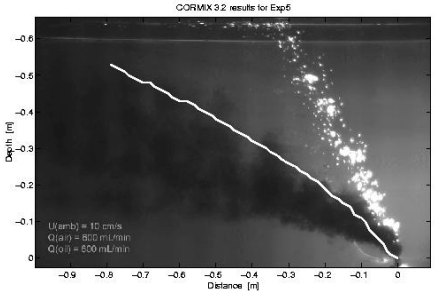

Experiment C5

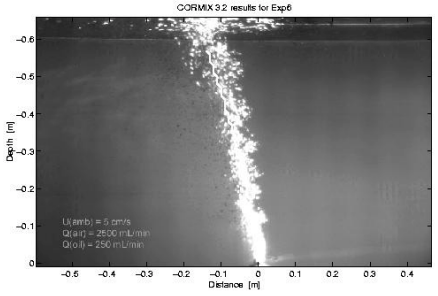

Experiment C6

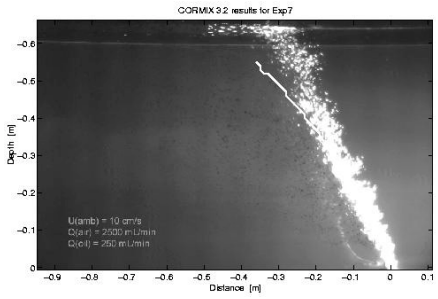

Experiment C7

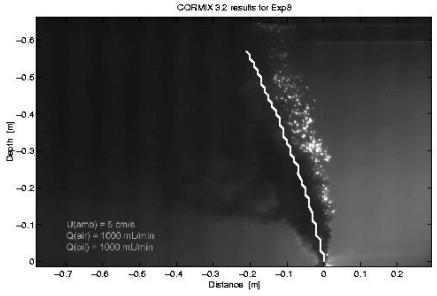

Experiment C8

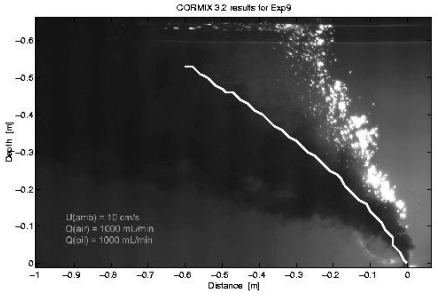

Experiment C9

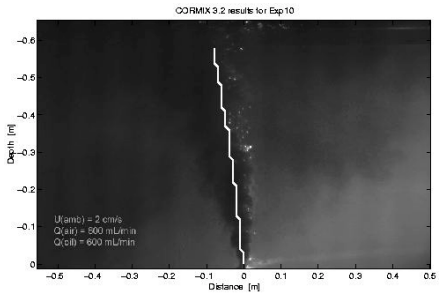

Experiment C10

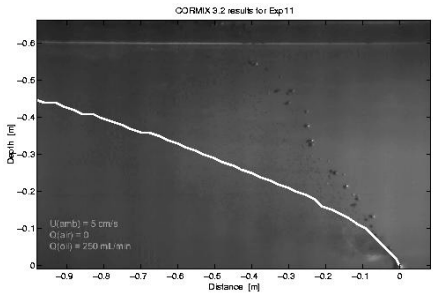

Experiment C11

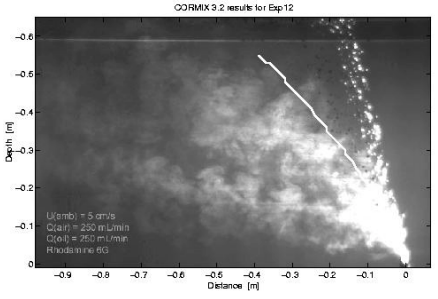

Experiment C12

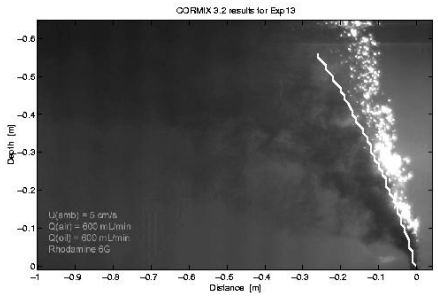

Experiment C13

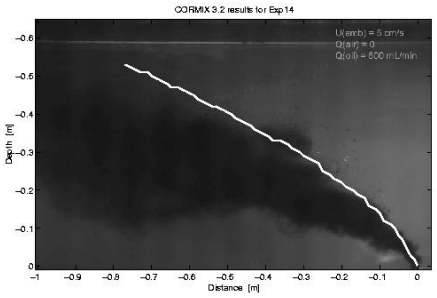

Experiment C14

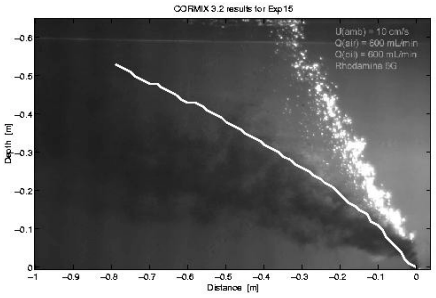

Experiment C15

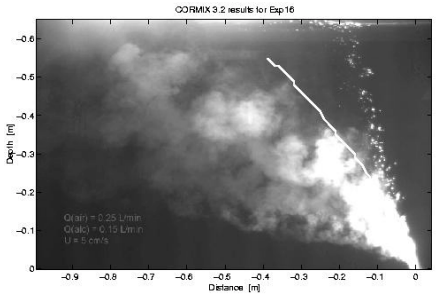

Experiment C16

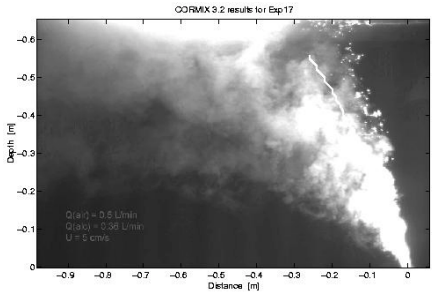

Experiment C17

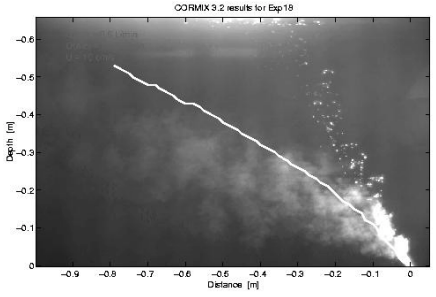

Experiment C18

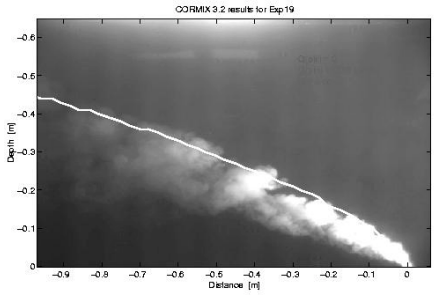

Experiment C19

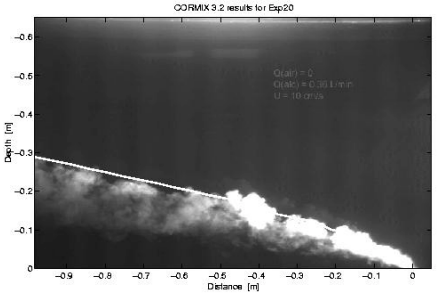

Experiment C20

Appendix D: PDPA Verification Tests

Crude oil droplet size spectra obtained with the PDPA operated in the reflective mode contained few samples below about 1 mm. This seemed to contradict close-up video records and visual observations of the dispersed phase. The response of the PDPA appeared to be highly biased toward large droplets. To determine whether the instrument was capable of detecting small droplets in the configuration employed in the oil experiments, the PDPA was tested by performing size measurements of reflective metal balls of known diameters.

A 20 gallon aquarium was substituted for the large Plexiglas tank to facilitate recovery of the balls. The aquarium was filled with water and balls were guided downward to sink through the PDPA optical sample volume using a small submerged glass funnel. Five different sizes of balls were utilized. Each size was tested individually by pouring 100 to 200 balls through the PDPA sample volume. In addition, a mixture comprising about 100 balls of each size was tested. The PDPA set-up was essentially the same as in the oil jet breakup experiments. The only differences were: (1) the receiver optics and polarizer needed to be rotated 180° since the balls moved in the opposite direction (downward) of the rising oil droplets; and (2) the optics had to be shifted slightly closer to the sample volume since the optical path length through water was shorter, which reduced the effective focal lengths of the PDPA transmitter and receiver lenses.

Table D.1 lists the metal balls that were used as standards to verify the response of the PDPA. According to the supplier, these laboratory grade spheres are manufactured to precision tolerances. The indicated sphericity is the difference between the minimum and maximum diameters of a ball given in millionths (10^{-6}) of an inch (0.0254 μm). Although it could not be independently confirmed, within any given collection of balls, diameters were specified to fall within ±5% of the nominal value.

PDPA size histograms measured in these tests are presented in Figures D.1 through D.5. Mean diameters calculated from these data consistently underestimated ball sizes by 10% to 15%. This was contrary to what was suspected, i.e., that diameters measured with the PDPA were significantly larger than actual values. Furthermore, when a mixture of different size balls were poured through the sample volume, the smallest size was detected best.

Table D.1 Precision metal balls used in the PDPA verification tests

Material	Diameter [μm]	Specific Gravity	Sphericity Grade
Chrome steel	396.9 (1/64")	7.833	25
Brass	793.8 (1/32")	8.47	200
Stainless steel	1588 (1/16")	7.916	100
Stainless steel	2381 (3/32")	7.916	100
Brass	3175 (1/8")	8.47	200

The verification tests appear to confirm that the PDPA configuration employed in the present oil experiments is capable of detecting small reflective droplets under the ideal condition of extremely low particle number density. As discussed in Section II of this report, however, at the

high droplet concentrations encountered in oil jet breakup, the PDPA is susceptible to bias and other errors that can profoundly impact measured size statistics.

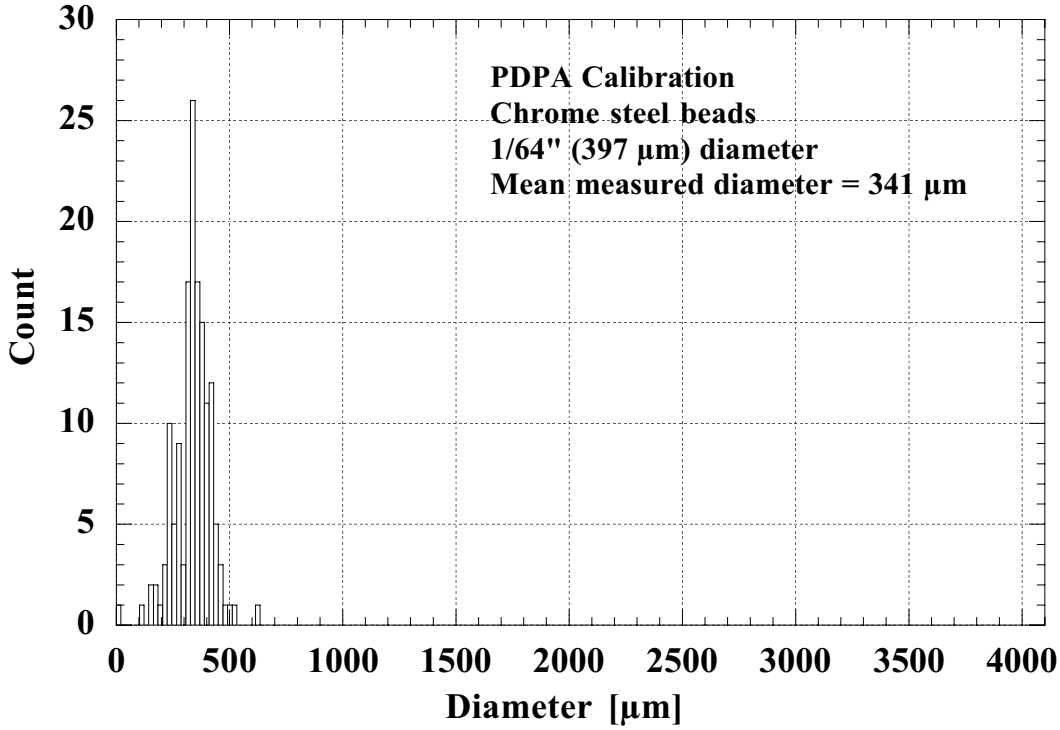

Figure D.1 Measured size histogram of 397 µm diameter chrome steel balls.

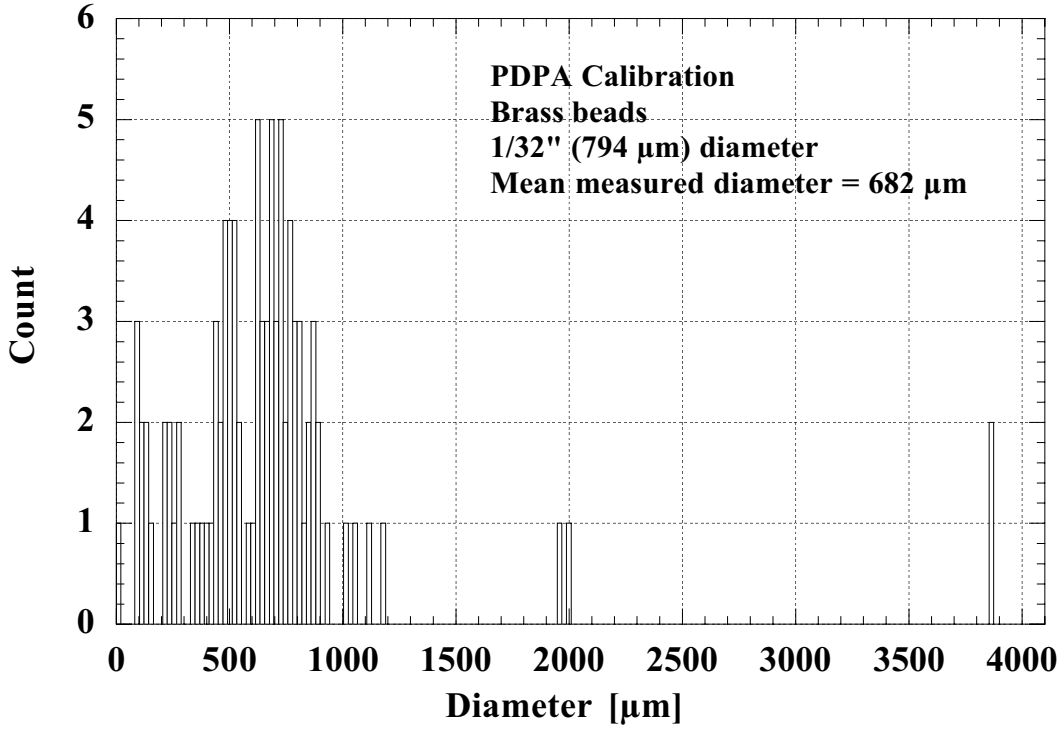

Figure D.2 Measured size histogram of 794 µm diameter brass balls.

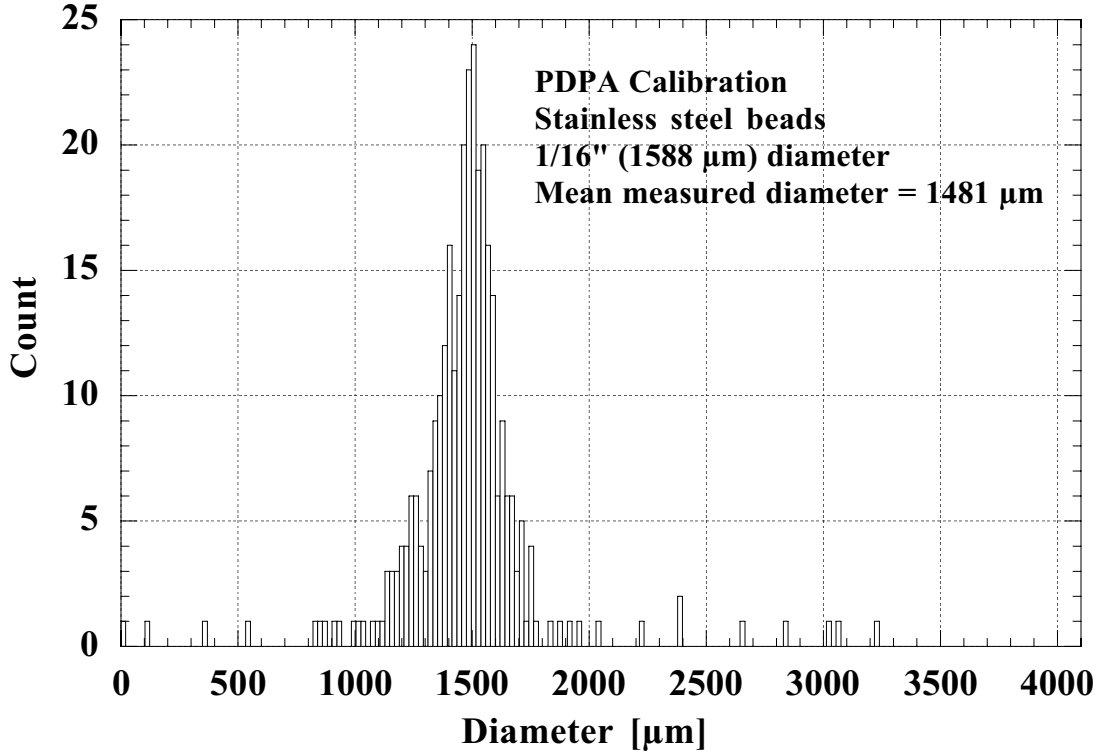

Figure D.1 Measured size histogram of 1588 µm diameter stainless steel balls.

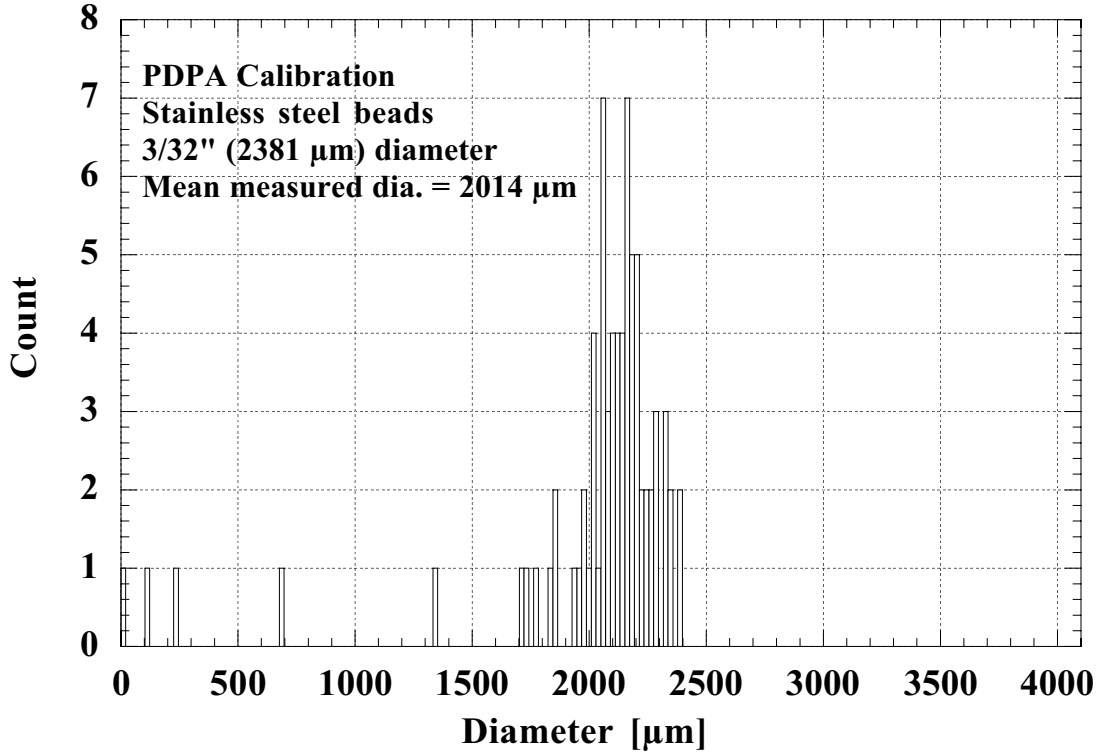

Figure D.1 Measured size histogram of 2381 µm diameter stainless steel balls.

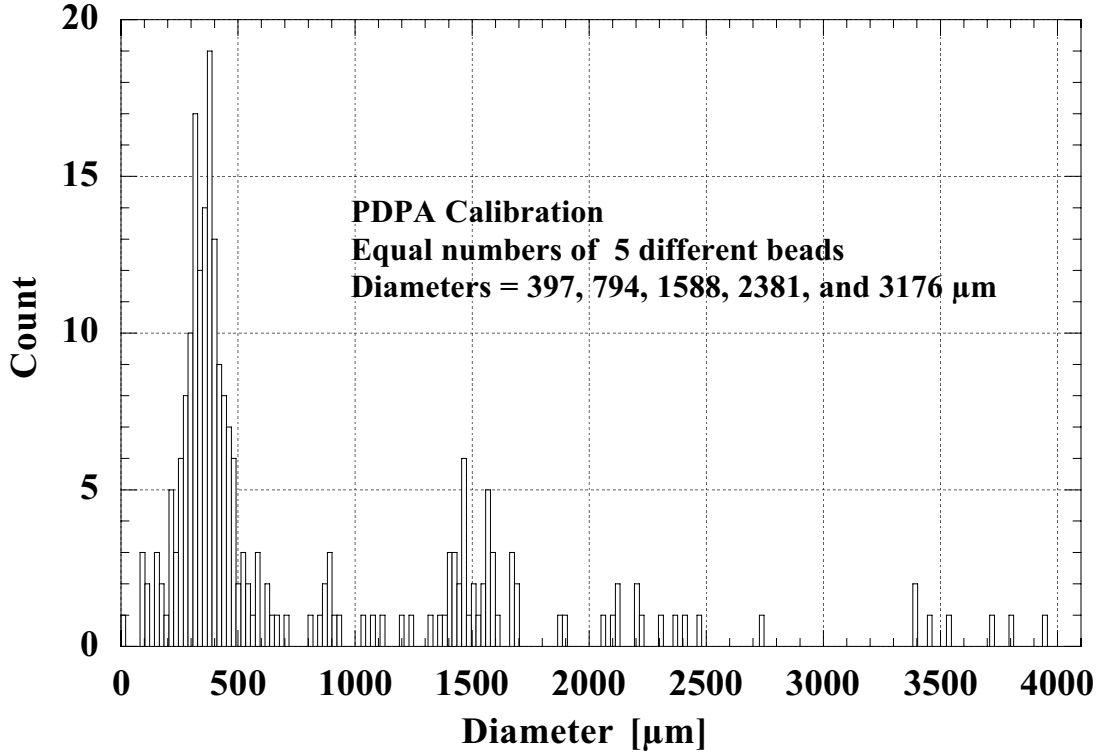

Figure D.1 Measured size histogram of a mixture comprising about 100 balls each of 5 different diameters.